Positron annihilation spectroscopy of sub-surface defects in semiconductors

Pi, Xiaodong

Award date:
2003

Awarding institution:
University of Bath

POSITRON ANNIHILATION SPECTROSCOPY OF SUB-SURFACE DEFECTS IN SEMICONDUCTORS

Xiaodong Pi

Submitted for the degree of
Doctor of Philosophy
of the University of Bath
2003

ProQuest LLC
789 East Eisenhower Parkway
P.O. Box 1346
Ann Arbor, MI 48106-1346

To my Mother

Acknowledgements

Firstly, I would like to thank my supervisor, Prof. P. G. Coleman, for intelligent guidance and strong support. It goes without saying that this thesis would not have been possible without him. In the past three years I have benefited a lot from such an excellent supervisor that gave me enough freedom and still led me in a correct direction. Without his insights and experiences the value of my work would not have been fully recognized.

I am very grateful to Dr. C. P. Burrows for the help in my research. Useful ideas could always come from the discussion with him. His expertise in the design and realisation of a slow positron beam is impressive. It was his great contribution that enabled the compact positron beam spectrometer to work in our lab in July, 2003. I will also never forget that he is a kind man with amazing knowledge about birds.

I would like to thank Mr. H. Bone for the technical support in my work. He also kindly taught me lots of English humour. It is a great progress that I can share jokes with him in many cases now. Many thanks are also due to Miss R. Mason, who is considerate and helpful in our lab.

I would like to thank Dr. R. M. Gwilliam and Prof. B. J. Sealy at the ion beam centre of the University of Surrey for the preparation of ion-implanted samples. I am indebt to Prof. W. N. Wang and Mr. C. L. Tseng in our department for the preparation of gallium nitride samples and allowing me to use their annealing facility. I would further like to thank Miss S. Zeng and Dr. D. Wolverson in our department and Miss R. Harding and Prof. A. T. Collins at King's College, London, for their help in my photoluminescence measurements. Mr. H. Perrott and Prof. R. Stevens at the materials research centre helped me with transmission electron microscopy. Dr. A. Lapkin in the department of chemical engineering helped me with Fourier transform infrared spectroscopy. I appreciate all of them sincerely.

Especially, I would like to acknowledge the support of my parents and brothers. It is their encouragement that stimulates me to keep striving. Finally, I thank Shanshan, whose love and help have been and will continue to be invaluable in my life.

Abstract

Slow positron beam based positron annihilation spectroscopy (PAS) has been used to study open-volume defects in ion-implanted silicon (Si) and gallium nitride (GaN) films. Firstly, the Doppler-broadening measurement parameters of PAS for the study of vacancies in Si are optimized by using theoretical Doppler broadened spectra. Optimum regions of interest are determined according to crystalline orientation and detector energy resolution.

The interaction between vacancies and impurities such as oxygen (O) and fluorine (F) and the behaviour of the corresponding vacancy (V)-impurity complexes have been investigated in ion-implanted Si. It is found that the evolution of divacancies (V_2) to V-O complexes competes with V-interstitial (I) recombination at low temperature. V_mO_n ($m > n$) are formed in the shallow region most effectively at 700 °C. V_xO_y ($x < y$) are produced near projected range (R_p) by annealing. At 800 °C implanted Si ions diffuse and reduce m, and implanted O ions diffuse and increase n in V_mO_n. All O-related V-type defects appear to begin to dissociate at 950 °C. F retards V-I recombination because vacancies and interstitials trap F to form complexes. F diffuses in the V-rich region via a vacancy mechanism. After a long annealing time at 700 °C F precipitates are developed from the V-type defects around the R_p and the I-type defects at the end of range.

With the support of photoluminescence spectroscopy it is found that nitrogen and oxygen are trapped in the voids around nanocrystalline Si (*nc*-Si) at low temperatures. It appears that the defects at the *nc*-Si/SiO_2 interface have already been completely passivated by nitrogen and/or oxygen in the as-formed *nc*-Si sample. High temperature annealing during the formation of *nc*-Si causes hydrogen originally residing in the SiO_2/substrate region to enter the SiO_2 structure. It diffuses back to the SiO_2/substrate region in vacuum at 400 °C because no other impurities block its diffusion channels. At temperatures above 700 °C, both nitrogen and oxygen react with *nc*-Si, resulting in a volume increase. This introduces stress in the SiO_2 matrix, which is relaxed by the shrinkage of its intrinsic open volume.

It is concluded that gallium vacancies (V_{Ga}) exist alongside dislocations and are stable up to 900 °C. Dislocations are believed to behave as shallow positron traps. The decrease of dislocation density increases the positron effective diffusion length (L_{+eff}) and the probability of trapping at V_{Ga} for annealing at $\leq$ 500 °C. Above 500 °C, the trapping of positrons at V_{Ga} is saturated while L_{+eff} continues to change.

Finally, A compact user-friendly positron beam annihilation spectrometer is introduced. Its design features, performance and first results are presented and discussed. Possible applications are described, including ion dosimetry and mapping, SIMOX process control, void monitoring and thin film interrogation.

Contents

List of Figures

Chapter 1

Slow Positron Technique

1.1 Introduction

Positron annihilation spectroscopy (PAS) is an effective method to investigate the defects in materials[1, 2]. It was firstly applied to metals and alloys in the 1970s. From the mid-1980s its application was widened to semiconductors. In the development of PAS the appearance of the slow positron technique is a milestone. Compared with the conventional PAS, the slow positron technique employs much lower positron implantation energies, which are monoenergetic and adjustable. This leads to convenient investigations of thin films, epitaxial layers and sub-surface regions of bulk materials, which are all important in semiconductor technology. Hence, it is no wonder that slow positron technique has become dominant in the field of positron research on semiconductors[3, 4, 5].

The defects investigated by PAS are mainly open-volume defects, such as vacancies, vacancy agglomerates, vacancy-impurity complexes and dislocations[6]. This is due to the attractive potential at an open-volume defect, which results from the lack of repulsive positively charged nucleus. When an energetic positron enters a material, it will reach a thermal equilibrium in a few picoseconds (10^{-12}s). The thermalized positron may be trapped at a certain open-volume defect with an attractive potential during its diffusion. In contrast to the high electron den-

sity in a perfect material, the electron density at the open-volume defect is lower because of a lost atom. Therefore, the positron lifetime at the open-volume defect is longer than that at the perfect material, e. g. it takes the positron a longer time to annihilate with an electron emitting two gamma photons when it is localized at the open-volume defect. Moreover, in the annihilation process of a positron with an electron, the energy and momentum are conserved. The lower momentum of the electron at the open-volume defect resulting from the lack of a nucleus causes a smaller angular deviation from 180° between the two gamma photons emitted from the annihilation of positron-electron pair. It also causes smaller Doppler shift of the two emitted gamma photons whose energies are about 511 keV. Therefore, by analyzing the information conveyed by the emitted gamma photons, the open-volume defect can be effectively studied by positron lifetime technique, angular correlation of annihilation radiation technique, and Doppler broadening technique. These techniques can all be realized with slow positron beams.

1.2 Positron annihilation

Positrons can be obtained from the β^+-decay of radioactive isotopes (e. g. ^{22}Na, ^{64}Cu, ^{58}Co, etc.). At the present time, ^{22}Na is the most used source because of its relatively high positron yield ($\sim$ 90.4 %), nearly simultaneous appearance of 1.27 MeV gamma photons with the emission of positrons which enables the positron lifetime measurement, simple manufacture, long half-life (2.6 years) and reasonable price. ^{22}Na decays by emission of a positron, e^+, and an electron neutrino, ν_e, to be the excited state of ^{22}Ne , ^{22}Ne*. Then ^{22}Ne* changes to the ground state of ^{22}Ne after 3.7 pico-seconds by emitting a 1.27 MeV gamma photon. The formulas of the delay reaction of ^{22}Na are as follows:

$$^{22}Na \rightarrow ^{22}Ne^* + e^+ + \nu_e \tag{1.1}$$

and

$$^{22}Ne^{*} \rightarrow ^{22} Ne + \gamma. \tag{1.2}$$

When the positron enters a semiconductor, it will annihilate with an electron by predominantly emitting two 511-keV gamma photons, e. g., $e^{-} + e^{+} \longrightarrow 2\gamma$. The probability of three-photon emission is only $\sim$ 0.3 % and hence can be neglected. However, at the surface of the semiconductors, where the electron density is very low compared with that in the bulk, positronium could be formed. A positronium is similar to a hydrogen atom except that a positron substitutes the proton. If the positron has the same spin as the electron, the formed positronium is called ortho-positronium, which annihilates by emitting 3γ. Otherwise, the formed positronium is para-positronium, which annihilates by emitting 2γ. The ratio of ortho-positronium to para-positronium is usually 3:1.

1.3 Slow positrons

In conventional positron measurements a positron source is placed between two identical samples. The main advantage of such an arrangement is that the samples can be measured in air. In the meantime the high positron energy up to 540 keV allows a relatively high maximum penetration depth in the samples. However, the sample preparation must be made according to its unique requirements, the crucial one of which is that the samples must be thick enough to ensure an essential fraction of positron annihilating in the samples. In the research on semiconductors many problems are linked to thin layers, sub-surfaces and interfaces, where the conventional positron techniques can just have a limited application. The low-energy positron (slow positron) technique, however, displays its strong power at the most in such an area.

The positron energy is monoenergetic and usually varies in the range from 0 to 40 keV in the slow positron technique. The monoenergetic positrons are obtained by moderating emitted positrons with a material of negative positron

work function, which is usually tungsten. The moderated positrons (< 1 %) are separated from unmoderated ones and accelerated to a required energy. The energy variation makes the defect profiling possible in a semiconductor. The transfer of positrons from the source to a sample is carried out in a vacuum with a magnetic field. The vacuum condition of 10^{-5} Pa is sufficient and can be easily achieved.

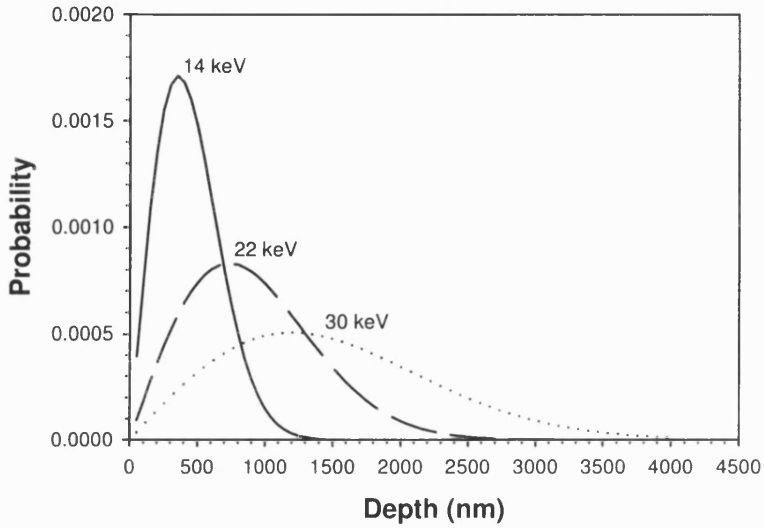

Figure 1.1: The positron distribution in wurzite GaN with the implantation energies of 14, 22 and 30 keV.

The distribution of slow positrons at the implantation energy of *E*, *P(z, E)*, in a material is a Makhov profile[7, 8]. It is read as:

$$P(z,E) = \frac{mz^{m-1}}{z_0^m} exp[-(\frac{z}{z_0})^m] \tag{1.3}$$

with

$$z_0 = 1.13\overline{z} \tag{1.4}$$

where m is an empirical parameter and $\overline{z}$ is the positron mean depth, which is

given by

$$\overline{z} = AE^r/\rho \tag{1.5}$$

where A, r are also empirical parameters. Typically used empirical values are: $m = 2$, $r = 1.6$, and $A = 4.0$ μg cm^{-2}keV^{-r}[9]. ρ is the mass density of the sample. It can be seen that the positron mean depth is proportional to the implantation energy, inverse proportional to the material density. The maximum positron energy is usually fixed for a slow positron beam. Hence, the material investigated determines the maximum depth which positrons can reach. For example, the maximum mean depths are 3.96 and 1.60 μm in silicon and gallium nitride (GaN) for a slow positron beam with the maximum implantation energy of 30 keV, respectively. The full width at half maximum (FWHM) of a Makhov distribution is approximately equal to the mean depth. It means that FWHM increases with the implantation energy. This worsens the depth resolution of slow positron measurements. Figure 1.1 illustrates the positron distribution in wurzite GaN at some implantation energies. It is very clear that at lower energies the profiles are sharper and hence the depth resolutions are better.

1.4 Observables

1.4.1 Positron lifetime

A conventional positron lifetime is defined as the interval between the birth of a positron and its annihilation with an electron in a material. It is the inverse of positron annihilation rate. The signal of the 1.27 MeV gamma photon accompanying the positron emission from a source is used as the start signal. The 511 keV gamma photon serves as the stop signal. A main difference in a slow positron technique is that expensive electronics should be employed to realise pulsed beams, whose pulse signal is used as the start signal.

When positrons are trapped in open-volume defects, the positron lifetime

increases with respect to the defect-free sample. The value of the longer positron lifetime component is a measure of the size of the open-volume defect. The strength of this component, i.e., its intensity, is directly related to the defect concentration. In principle, both the kind and concentration of the defect under investigation can be obtained independently by a single measurement.

The positron lifetime spectrum, *dn(t)/dt*, is the probability for the positron annihilation at time *t*. It can be expressed as follows:

$$dn(t)/dt = \sum_{i=1}^{N} I_i exp(-t/\tau_i)/\tau_i \tag{1.6}$$

Where $n(t)$ is the positron concentration, τ_i and I_i (i=1, 2, ..., N)is the positron time and its corresponding intensity at the ith trapping site, respectively. By decomposition of a lifetime spectrum, the characteristic positron lifetime for a definite defect can be obtained. The defect concentration can also be calculated using the corresponding I_i. In practice, an experimentally obtained spectrum is a convolution of the real spectrum described above and a Gaussian time resolution function whose FWHM is usually 200 to 250 ps. Such a convolution limits the time resolution of the positron lifetime spectra. In addition, a proper source correction must be made for the lifetime spectrum because 5 to 10 % of positrons annihilate in the source material. Allowing for the finite time resolution, annihilation in the source materials (if slow positrons are not used) and random background, typically only 1 to 3 lifetime components can be resolved in the analysis of the experimental spectra. The distinguishing of two lifetime components is only successful only if the ratio of them is larger than 1.5.

In positron lifetime measurements average lifetime, τ_{av}, is a good and statistically accurate parameter. It is the center of mass of the lifetime spectrum, expressed as:

$$\tau_{av} = \sum_{i=1}^{N} I_i \tau_i \tag{1.7}$$

τ_{av} can be correctly calculated from the respective intensity and lifetime even if

the spectrum decomposition only represents a good fit to the experimental spectrum without any physical meaning. Changes smaller than 1 ps can be reliably observed. By comparing τ_{av} with the lifetime in a "defect-free" reference sample, τ_b, one can clearly tell if any open-volume defect exists. p-type semiconductor crystal is often a good reference sample because all vacancy defects are in their most positive charge state if they exit and thus minimizing the effect of positron trapping.

1.4.2 Momentum distribution

Doppler Broadening

After the annihilation of a positron with an electron, the momentum of the positron-electron pair, $\boldsymbol{p}$, is transferred to two gamma photons because of the momentum conservation. The component of $\boldsymbol{p}$, $\boldsymbol{p}_z$, parallel to the propagation direction z of the gamma rays results in a Doppler shift ΔE of the annihilation energy of 511keV, which is approximately equal to:

$$\Delta E = p_z c/2. \tag{1.8}$$

In a measurement lots of annihilation events (typically larger than 10^6) are registered to give a complete Doppler spectrum. The energy distribution of gamma photons is broadened with the centroid at 511 keV owing to the individual Doppler shifts in both directions, $\pm$ z. Since the momentum of a thermalized positron is negligible, p could be regarded as the momentum of the electron in the positron-electron pair. Electrons can be divided into high-momentum core electrons and low-momentum valence electrons in a material. In open-volume defects positrons mainly annihilate with valence electrons because of the low-density core electrons resulting from the missing atoms. Owing to the low momenta of valence electrons, the Doppler shift ΔE is smaller compared with that in the case of the annihilation in a defect-free region.

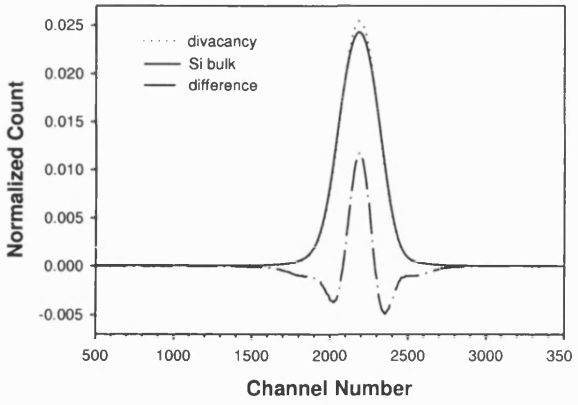

Figure 1.2: The Doppler-broadening spectra of defect (divacancy) and defect-free bulk in (100) silicon. The difference between them is also plotted. The spectra are measured in oxygen implanted silicon (400 keV, 10^{14} cm^{-2}) by adjusting the positron energy to 6 keV and 30 keV for the measurements of defects and bulk, respectively. The centroid of each spectrum is at 511 keV. One channel is equivalent to 9.309 eV.

S and W parameters are typically used to evaluate the Doppler-broadening spectra quantitatively. S is defined as the area of the central low-momentum part of a spectrum, A_s, divided by the area below the whole spectrum, A, after background subtraction:

$$S = A_s/A \tag{1.9}$$

W is calculated as the area of the high-momentum wing part of the spectrum, A_w, divided by A:

$$W = A_w/A. \tag{1.10}$$

The effect of positron trapping in defects on the Doppler-broadening spectrum is demonstrated in Figure 1.2. It can be seen that the spectrum of defective silicon with divacancies is sharper than that of defect-free silicon. It means S (W) is larger (smaller) of defective silicon than that of defect-free silicon. By comparing

S (W) values in the studied sample and defect-free (reference) sample, one can know whether defects exist. The S (W) in the reference sample is often written as S_b (W_b).

A_s (A_w) is usually called the region of interest (ROI). Its change brings the variation of S (W). In order to characterize defects with small errors and high sensitivity, A_s (A_w) must be carefully selected according to detector energy resolution, crystal orientation, and material and defect type. Practically, there are some differences between the selections of A_s (A_w) in different laboratories. This makes the direct comparison of S (W) value very difficult. The comparison is still not reliable even if the normalized parameter, S/S_b (W/W_b), is employed. This is due to the effect of detector energy resolution and crystal orientation, especially the former, although the ROI is the same.

If all implanted positrons annihilate at defect, S (W) will be the characteristic parameter for this kind of defects, S_d (W_d). S (W) can be expressed as the linear sum of the characteristic parameters for respective positron trapping site:

$$S = \sum f_{di} S_{di} + (1 - \sum f_{di}) S_b \tag{1.11}$$

$$W = \sum f_{di} W_{di} + (1 - \sum f_{di}) W_b \tag{1.12}$$

where f_{di} is the fraction of positrons trapped and annihilating at the ith kind defects, whose characteristic parameter is S_{di} (W_{di}). If only one type of defects exists uniformly in the samples, it is possible to calculate its concentration, C_d (per atom), from the measured S with the formula as follows:

$$C_d = \frac{\lambda_b (S - S_d)}{\mu_d (S_d - S)}, \tag{1.13}$$

where λ_b and μ_d are the positron annihilation rate and trapping coefficient at the defect, respectively. Actually, the surface of a material is an effective trapping site for positrons. If the investigated area is very near surface, the contribution

of the characteristic parameter S_s of the surface should be taken into account. This usually makes the analysis difficult.

From (1.11) we can see the value of S will be saturated if all the implanted positrons annihilate at defects ($\sum f_{di}$=1). It means there is no change in S any more even if the defect concentration continues to increase, e. g. the sensitivity of S to defect concentration vanishes. In this case, back-diffusion measurements are adopted to calculate the effective positron diffusion length (L_{+eff}) using the fraction of positrons diffusing back to the surface. Because of

$$\lambda_d = \lambda_b[(L_+/L_{+eff})^2 - 1], \tag{1.14}$$

λ_d, the positron trapping rate at defects, can be calculated with the experimentally obtained L_{+eff}, known positron diffusion length, L_+, and positron annihilation rate, λ_b, at a defect-free material. Then the defect concentration can be obtained with the expression:

$$C_d = \lambda_d/\mu_d. \tag{1.15}$$

If only one type of defects exist, the following expression can be derived from (1.11) and (1.12):

$$\frac{S - S_b}{W - W_b} = \frac{S_d - S_b}{W_d - W_b} = k, \tag{1.16}$$

where k is a constant, which is dependent on the defect type. Therefore, the points will be on the same line, whose slope is k, when S (S/S_b) is plotted against W (W/W_b). This is usually used to tell how many kinds of defects are in the sample investigated.

In addition, one can tell whether the vacancy is decorated by impurities by plotting the respective characteristic S for different vacancies (V_x, $x = 1 \sim 5$)[10]. If there is no impurity decorating these vacancies, there will be no deviation from the linearity of S over W.

Angular Correlation of Annihilation Radiation (ACAR)

The components of $\boldsymbol{p}$, $\boldsymbol{p}_{x,y}$, perpendicular to the propagation direction z of the gamma rays lead to the angular deviation, $\Theta_{x,y}$, of the collinearity of two emitted gamma photons. $\Theta_{x,y}$ is expressed as

$$\Theta_{x,y} = \frac{p_{x,y}}{m_0 c}, \tag{1.17}$$

where m_0 is the rest mass of the electron.

The momentum distribution is usually recorded in two dimensions in ACAR. This is so-called 2D-ACAR. If a position-sensitive detector is used, one-dimension ACAR (1D-ACAR) could be realized. The angular resolution is in the range from 0.2 to 5 mrad, corresponding to the energy resolution in the range from 0.05 to 1.3 keV. Thus, ACAR has a much better momentum resolution than Doppler broadening spectroscopy. The measurement time, however, is very long (several days). The main applications of ACAR are in bulk electronic structure and Fermi surface studies.

1.5 Summary

Positron annihilation spectroscopy is a powerful tool to study the defects, especially open-volume defects, in materials. The advent of slow positron techniques made it possible that thin structures such as sub-surfaces, thin films and epitaxial layers can be measured by PAS. Slow positron techniques mainly consist of positron lifetime spectroscopy, Doppler-broadening spectroscopy and angular correlation of annihilation radiation. They can play a role in the characterization of semiconductor materials.

Chapter 2

Open-Volume Defects in Ion-Implanted Semiconductors

2.1 Introduction

Ion implantation has been one of the most important tools in silicon-based microelectronics industry[11, 12]. When the device dimension decreases to deep sub-micrometer regime, however, ion implantation is faced with ever severer challenges. The critical dimensions of metal-oxide-semiconductor (MOS) devices in the near future are shown in Table 2.1 [13]. The challenges caused by the decreasing dimensions require a more complete understanding of the interaction between the defects and dopants during implantation and activation of dopants. For example, the role of interstitial-type defects introduced by B^+ implantation has been carefully investigated to understand the mechanism of B transient enhanced diffusion[14]. The successful manufacture of a shallow junction in a p-MOS will benefit from such an understanding. Open-volume defects are inevitable in ion implantation. They are usually in the forms of vacancy, divacancy, vacancy-impurity complex, vacancy cluster and void, etc.. It was shown that some dopants such as Sb[15] and Ge[16] are vacancy-related diffusers so that their distribution could be impacted by vacancies in silicon. It is also demonstrated that vacancies play an important part in the activation of dopants, e.g., B[17]. In addition, the

Table 2.1: Projected MOS source/drain doping technology requirements[13].

First year of production	2001	2004	2007	2010
Transistor gate length (μm)	0.18	0.13	0.10	0.07
Depth of p-n junction at channel (nm)	30-80	20-60	15-45	10-30
Surface concentration (cm^{-3})	10^{19}	10^{19}	10^{20}	10^{20}
Wafer diameter (mm)	300	300	300	
Metal impurity (10^9at.cm^{-2})	10	5	2.5	< 2.5

effects of open-volume defects are critical in other ion implantation related techniques such as impurity gettering[18, 19]. Therefore, the study of open-volume defects is not only a natural component of defects research in ion-implanted silicon, but also scientifically and technologically important issue closely linked to the continuing development of Si-base ultra-large-scale integrated (ULSI) circuits.

Compared with defect study in ion-implanted silicon, the counterpart in III-V compound semiconductors seems weak. Although ion implantation has been applied into GaAs, some special problems deter the understanding of the defect formation and the annealing in ion-implanted GaAs. Firstly, during implantation a variety of defects with different annealing behaviour are generated in both sublattices of GaAs. Secondly, the comparably high arsenic vapor leads to a selective evaporation, which makes the heat treatment difficult. Finally, the recoils of As and Ga by ion implantation produce vacancies near the surface and an excess of interstitials in deeper regions. In the research of GaN ion implantation is still struggling to realize its potential[20]. Without doubt a successful and full application of ion implantation depends on the understanding of production and annealing of defects. Unfortunately, the study of defects, especially the open-volume defects, in ion-implanted III-V semiconductors is rather limited owing to the inherent complexity.

The defects induced by ion implantation are usually located in the sub-surface regions of semiconductors (shallower than 4 μm). These regions are exactly suitable to be investigated by slow positrons. In the last decade lots of studies on vacancy-type defects in ion-implanted semiconductors, especially Si, have been done by using the slow positron technique. This establishes one of standard applications of the slow positron technique.

2.2 Ion implantation

2.2.1 Ion distribution

As each implanted ion enters a target, it goes under a series of collisions with the target atoms until it finally comes to rest at some depth. The collisions can be divided into elastic ones between the ion and the nucleus of the target atom, and inelastic ones between the ion and the electron in the target. Each implanted ion has a random path as it moves through the target, losing energy by nuclear and electronic stopping. Since each implantation dose contains a number of ions ($> 10^{10}$ ions/cm^2), the average behaviour of these ions could be well predicted. Their distribution is approximately a Gaussian profile[21]. Figure 2.1 shows B^+ implantation into Si simulated by TRIM[22], which is a Monte Carlo code using binary collision approximation. The Gaussian distribution of B^+ in Si is clear in Figure 2.1 (a) .The ion concentration, $n(x)$, along the depth, x, is written as

$$n(x) = n_0 exp[\frac{-(x - R_p)^2}{2\sigma_p^2}], \tag{2.1}$$

where R_p is the average depth of all the implanted ions, usually called the projected range, σ_p is the standard deviation of the Gaussian distribution, n_0 is the peak ion concentration, which is located at R_p. n_0 can be easily obtained from the total ion dose, Φ, using the following expression:

$$n_0 = \frac{\Phi}{\sqrt{2\pi}\sigma_p} \cong \frac{0.4\Phi}{\sigma_p}. \tag{2.2}$$

At the edge of the ion beam, the lateral motion of the ions should be considered. The lateral distribution can also be approximated as Gaussian with a standard deviation of $\sigma_\perp$.

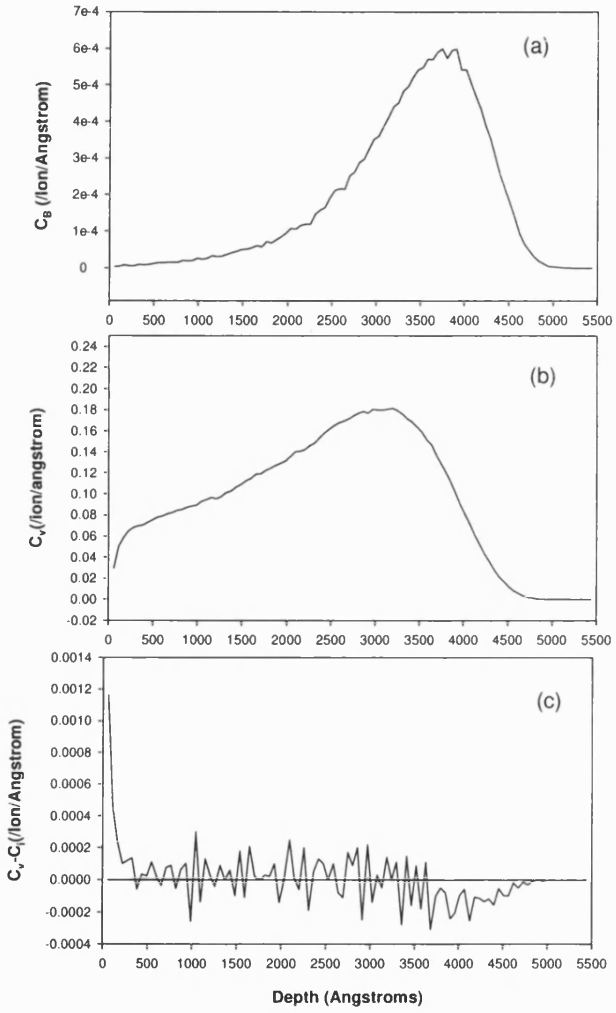

Figure 2.1: (a) Boron, (b) vacancy and (c) net vacancy (the concentration difference between vacancies and interstitials) profiles in 100 keV B^+ implanted silicon obtained from the simulation code TRIM.

2.2.2 Damage

In the elastic collisions the lost energy of the incoming ion is transferred to the target atom, which is recoiled from its lattice site, resulting in irradiation damage. The lost energy in inelastic collisions, however, is dissipated through the electron cloud into thermal vibration of the target. The damage caused by the inelastic collisions is usually negligible unless the implanted ion has a very high energy (the order of magnitude of MeV). The binding energy of a lattice site is only about 10 to 20 eV. Hence, it is easy for the incoming ion with a much higher energy to free an atom from its position and make it travel through the target as a second projectile. Now both the ion and the displaced atom travel and cause further displacements, so the initial energy of the ion is spread over many moving particles. Finally, the energy per particle decreases to be below the binding energy of a lattice site and the cascade stops. The result of one ion has been the displacement of many target atoms. After lots of ions have been implanted, an initially crystalline target will be highly disordered. There are many defects, mainly interstitials and vacancies, in the disordered area. Their distributions can be simulated by TRIM, too. Figure 2-1 shows the simulation result for 100 keV B into silicon. It can be seen that in the near surface region there are more vacancies than interstitials. At the end of the B distribution, however, there exist more interstitials. This separation of vacancies and interstials inherently results from the momentum transfer of implanted ions. Recently, DLTS and SRP measurements on MeV implanted Si have presented experimental evidences for the separation[23, 24]. The main disadvantage of TRIM is that it doesn't consider the annealing of defects. Actually, there exists recombination between vacancies and interstitials during implantation. If the temperature increases, the recombination will become more significant. Another simulation code called molecular dynamics (MD) simulation takes into account the thermalisation of the cascade region during implantation[25]. Because of a short time scale ($\sim 10^{-9}$s), MD is not suitable for studying the long-range diffusion of dopants and defects. However, kinetic Monte Carlo (KMC) can be coupled with MD to simulate it in a much longer time regime[26].

The damage induced by implantation heavily depends on target temperature and implantation dose. The lower the temperature is, or the higher the dose is,

the more damage is because of less recombination and more overlap between the defects. When the disorder reaches a certain level (e.g. 10 % of the lattice sites) in an area, this area will become amorphous. All the damage may be annealed out at some appropriate temperature.

2.2.3 Ion implanter

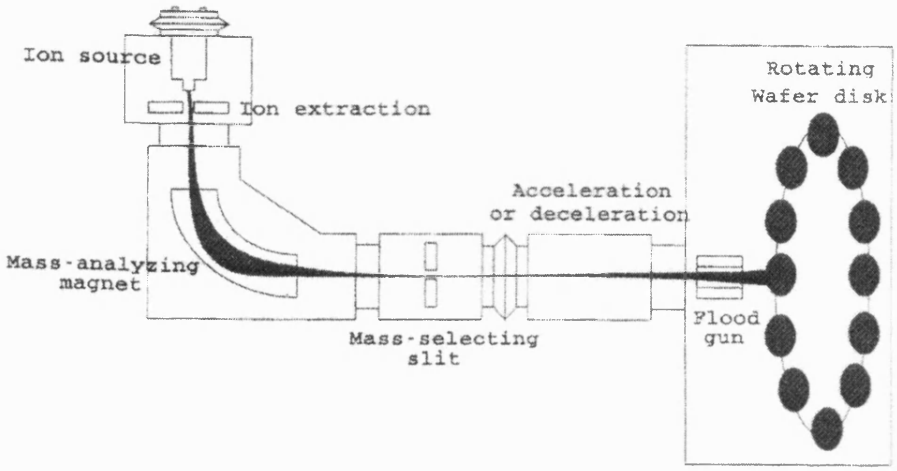

Figure 2.2: Schematic of a typical commercial ion implanter.

An ion implanter is typically composed of ion source, ion extraction, mass-analyzing magnet, mass-selecting slit, acceleration/deceleration, and wafer feeder (as shown in Figure 2.2). The ion source is heated by a filament. The resultant ion plasma contains the desired ion and many other species. An extraction voltage is applied to take the charged ions in the plasma out of the source chamber. Under a vacuum ($< 10^{-6}$ Torr) the magnet field chooses the charged ions with a desired charge to mass ratio. Only the chosen charged ions travel through the mass-selecting slit and then are accelerated or decelerated to required implantation energy.

The specific requirements for an ion implanter are different for different implantation energy ranges. It has become a sever challenge for the implanters to realize ultra-low energy implantation needed in shallow junction formation. A shallower

junction needs lower implantation energy and higher dose. In order to keep a reasonable throughput the beam current should be higher to reach the higher dose without a long time. The maximum beam current, however, decreases as a function of energy, owing to space charge effects or ion repulsive forces induced beam expansion. Effective approaches such as the use of large beam cross-section and short beam line were attempted on the high-current implanter for ultra-low energy implantation. Now the low energy capability for B^+ from 5 keV, 12 mA to 200 eV, 0.4 mA can be available by using several advanced implanters such as VIISion80 Plus, xR80 LEAP, ULE2 and SHC-80[27].

2.3 Open-Volume defects

2.3.1 Vacancies

A vacancy is the simplest open-volume defect in semiconductors. It usually introduces deep levels and can impact the electrical properties of semiconductors. The deep levels of vacancies in Si[28] and GaAs[29, 30, 31, 32, 33, 34] are illustrated in Figure 2.3 and 2.4, respectively. In wide-band-gap GaN, a nitrogen vacancy, V_N, has a shallow donor level about 0.06 eV below the conduction band[35], and a gallium vacancy, V_{Ga} can introduce three levels as a deep triple acceptor[36]. These three levels are marked in Figure 2.5, which shows the formation energy of various defects in GaN (Ga rich) as a function of Fermi level.

The charge state of a vacancy is dependent on the Fermi level. In the damaged area induced by ion implantation the Fermi level is usually pinned near the middle of the bandgap. Therefore, the vacancy is negatively charged in ion implanted silicon, the gallium vacancy is negatively charged in ion implanted GaAs and GaN. These negatively charged vacancies can be easily seen by positron measurements if they exist.

It is well known that the temperature affects the annealing of defects. At higher temperature, the agglomeration of defects can be enhanced together with

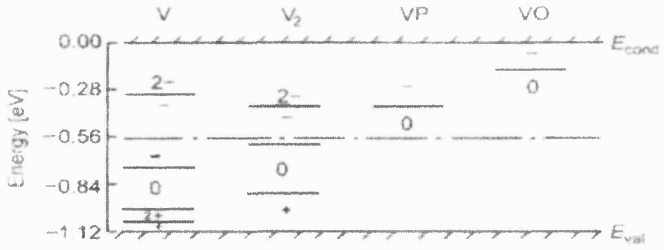

Figure 2.3: Energy-level scheme for various charge states of monovacancy, divacancy, vacancy-phosphorus pair (E center) and vacancy-oxygen pair (A center) in silicon[16].

their recombination owing to the accelerated thermal dynamics. In addition, there is a space separation for vacancies and interstitials in the ion implanted area. Hence, it is very possible that monovacancies agglomerate to divacancies, trivacancies, or even bigger vacancy clusters. It has been proved that divacancy is the dominant vacancy type in ion implanted silicon at room temperature[37, 38]. It means that nearly all the initial monovacancies annihilate by recombination with interstitials or agglomeration to divacancies. Most of the ion implantation is processed at room temperature for silicon in industry. The resultant main open-volume defects are divacancies, which is predominantly neutral in the defective implanted silicon so that it can trap positrons. Up to now extensive work about the open-volume defect (mainly divacancy) distribution and annealing has been done in ion implanted silicon.

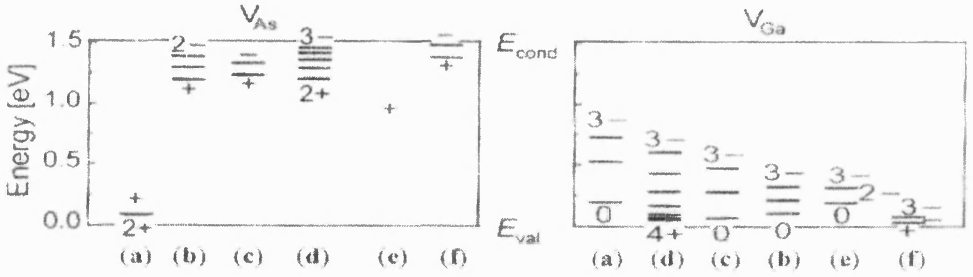

Figure 2.4: Energy-level scheme of arsenic vacancies, gallium vacancies in GaAs according to theoretical calculations of (a) Baraff and Schlter[29],(b) Puska[30], (c) Jansen and Sankey[31], (d) Xu and Lindelt[32], (e) Zhang and Northrup[33] and (f) Seong and Lewis[34].

The Ga vacancy dissolves at 300 K in GaAs. It is believed that the open-volume defects seen by positron measurements in ion implanted GaAs at temperatures higher than 300 K are defect complexes which include Ga vacancies. In electron irradiated GaN there are no Ga vacancies probed[35]. It is suggested that there is a strong combination between the negatively charged Ga vacancy and the positively charged Ga interstial. Another possible explanation is that the Ga vacancies have high formation barriers in damaged area because of the pinned Fermi level near the mid-band-gap (Figure 2.5). However, it is not clear whether there are no Ga vacancies in ion implanted GaN, as in electron irradiated GaN, although experiments have demonstrated the recombination rate is much higher in GaN than in other semiconductors during ion implantation[20].

Positively charged vacancies can be produced and survive the annealing during ion implantation. Owing to the repulsive Coulomb potential between these vacancies and positrons, it is difficult to measure them with positron techniques. Therefore, their behaviours remain elusive unless other measurement techniques are used.

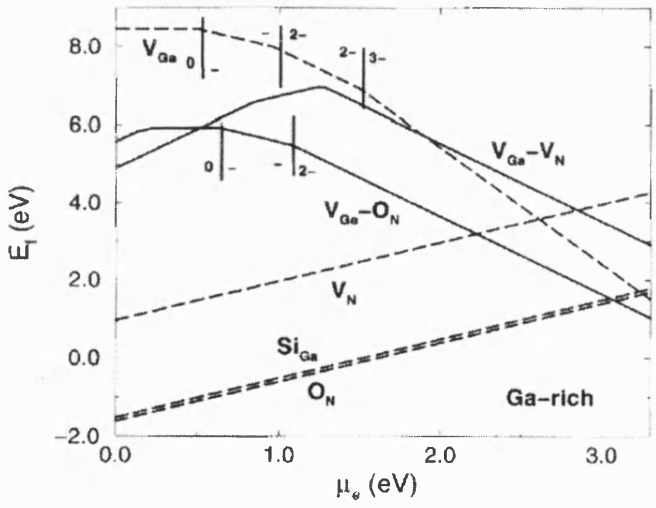

Figure 2.5: Formation energies (E_f) of various defects versus Fermi level (μ_e) position in GaN for the Ga-rich case. $\mu_e = 0$ when Fermi Level is at the top of valence band. The ionization levels of gallium vacancies and the complex of gallium vacancy and substitutional oxygen are also marked. The change of slopes means the variation of charge states[36].

2.3.2 Vacancy-Impurity complexes

Vacancies can combine with impurities to form vacancy-impurity complexes in semiconductors. The so-called A center (VO)[28] and E center (V-dopant)[39] have been identified in electron irradiated silicon. Their corresponding level positions are shown in Figure 2.3. In ion implanted silicon vacancies can combine with the residual impurities as well. For instance, it was found boron-divacancy complexes (V_2-B) formed in a 5 MeV self-implanted highly B doped silicon[40]. Vacancies can also combine with the implanted ions in all possibility. Vacancy-hydrogen complexes were clarified by both infrared absorption spectroscopy[41] and positron annihilation spectroscopy[42] in hydrogen implantation to silicon, which is applied to gettering engineering and manufacturing smart-cut wafers. Various vacancy-oxygen complexes (V_xO_y) were found in oxygen implanted silicon[43]. Vacancy-fluorine complexes were identified in the comparisons among B, BF_2 and F implanted silicon[44]. By analyzing the ratio of 511 keV photo peak of nitrogen-implanted silicon to a control silicon sample, the existence of vacancy-nitrogen complexes was proved[45], which is crucial to the explanation of nitrogen diffusion in silicon. It is well known that SIMOX (Separation by IMplantation of OXygen), an advanced silicon on insulator (SOI) structure, is realized by oxygen implantation. Implantation of BF_2 is an important technique for manufacturing shallow p-n junctions. Nitrogen implantation is of particular importance in mixed signal CMOS and system on a chip technology owing to its ability to retarding gate oxide growth and hence varying the gate oxide thickness across a wafer. In order to take full advantage of these implantation techniques, understanding the reaction between defects and impurities is mandatory. Therefore, the study of vacancy-impurity complexes is desirable.

Ga and As vacancies were found in electron irradiated GaAs. Their annealing all occurs at 300 K[46]. There are no reports on positron measurements of As vacancies in ion-implanted GaAs. The Fermi level is difficult to approach the conduction band in the ion-implanted layer even if GaAs is initially n type. Hence, As vacancies are predominantly positively charged so that they can't be measured by positron techniques. The measured open-volume defects in ion-implanted GaAs were believed to be Ga vacancy related complexes, denoted by $V_{Ga}X$[47].

2.3.3 Voids

As said previously, vacancies can agglomerate into clusters. A large vacancy cluster is called a void (they are equivalent in this thesis). Under such circumstances as high doses or high dose rates during implantation, vacancy clusters have been found in silicon. For example, the dominant defects in the as-implanted wafer were believed to be vacancy clusters with a positron lifetime of 500 ps when high dose ($\geq 10^{18}$ cm^{-2}) oxygen was implanted to form SIMOX[48]. In the annealing after implantation voids may form owing to the thermally enhanced agglomeration. The formation of stable voids at the depth shallower than half projected range in 850 °C annealed self-implanted silicon (245 keV, 8×10^{14} - 6×10^{16} cm^{-2}, 100 °C) has been observed recently[49]. Fujinami's work demonstrated that the clustering of divacancies appeared in the temperature range from 200 to 300 °C[50]. It was also found in the completely amorphised silicon by self-implantation a large number of voids formed and grew in the annealing of 600 to 700 °C[51]. In addition, large vacancy clusters V_x ($x \geq 10$) were observed at the vicinity of the peak of the hydrogen implantation profile (60 keV, 10^{16} cm^{-2}) in the range from 400 to 700 °C[52].

Although the work on ion-implanted GaAs is not as extensive as that on silicon, similar vacancy agglomeration has been observed too. By measuring oxygen implanted (80, 200 keV, 10^{13} - 10^{15}) GaAs with Doppler Broadening spectroscopy a near surface defective layer was found, whose S parameter went up more obviously for higher doses and was higher compared with monovacancies. It was concluded the defects here were vacancy clusters[52]. The vacancy clusters were also found in Se implanted GaAs after an additional annealing at 800 °C[53].

Voids are technologically important especially in the application of ion implantation to getter the metal impurities in silicon because they are effective nuclei for the impurity agglomeration[54]. Moreover they are also used to suppress the transition enhanced diffusion of B at the end of the range of B implantation by the pre-implantation of other ions such Si[55], Unfortunately, the applications of void related defect engineering in compound semiconductors are scarce. Hence, continuous study on voids is desirable in the sense of both enhancing the present application and exploring new defect engineering.

2.4 Summary

Ion implantation is one of the most important processes in semiconductor industry. It is also expected the ion implantation can play an important role in the device manufacture of new semiconductors such as GaN. Damage is inevitable in ion implantation. The resultant defects have great effect on devices so that the understanding of their behaviours is crucial. Open-volume defects such as vacancies, vacancy-impurity complexes and voids are the common defects located in the sub-surface regions in ion-implanted semiconductors. The slow positron technique can be readily employed to study these defects.

Chapter 3

Optimization of Doppler-Broadening Measurement Parameters for Silicon

3.1 Introduction

Slow positron beam techniques have been well established to study various defects, especially the open-volume defects, in all kinds of materials such as semiconductors, metals, alloys, and amorphous materials[56]. One can efficiently profile the distribution of defects in the near surface region by varying the incident energy of mono-energetic positrons. Although several observation methods are available for slow positron beam, Doppler Broadening is the most used one in many laboratories all over the world. This is due to its comparatively easy explanation of experimental data, fewer limits on instruments and shorter run time[4].

It is conventional to use a shape parameter (S) and/or a wing parameter (W) to characterize the shape of Doppler broadened 511 keV peak in order to obtain

the information of the defects in materials. S is the ratio of the central area (C) to the total area (T) under the peak and W is the ratio of the wing area (A) to T. The values of S and W are determined by the momenta of the electrons, which annihilate with positrons. If a thermalized positron annihilates with a valence electron, the Doppler broadening is small owing to the low momentum associated with it. This contributes to the increase of S. In contrast, the Doppler broadening is big under the circumstance of annihilation with a core electron, which usually has a higher momentum. The more positrons annihilate with core electrons, the bigger the value of W is. In open-volume defects, positrons mainly annihilate with valence electrons. Therefore, comparing to the perfect crystal, there will be a higher value of S or lower value of W in the crystal where open-volume defects exist. Practically, S and W make no sense unless they are compared with those of a perfect crystal. In order to characterize the defects in materials more directly, S/S_b or W/W_b is widely used, where the subscript b means that all thermalised positron annihilate in the bulk (perfect crystal). It is well known that the characteristic values of various defects are usually expressed in such a way as S_d/S_b and W_d/W_b, where the subscript d means that all the thermalised positrons annihilate in defects. It is an effective way to identify the type of the defect with S_d/S_b (W_d/W_b). In addition, S_d/S_b (W_d/W_b) is often used in the fitting programs such as VEPFIT to fit the experimental data and calculate the defect concentration[57].

S_d/S_b (W_d/W_b) depends upon (a) the region of interest (ROI) which determines the boundary of the areas C and A, (b) the energy resolution of the annihilation gamma photon detector, (c) the type and crystalline orientation of the material being studied[58, 59]. Of these only ROI is usually adjustable experimentally. Therefore, how to choose ROI is important, which should aim to optimize the characterization of defects, when S/S_b (W/W_b) is used. At the present time the ROI is conventionally chosen to make S_b equal to ~ 0.5 or W_b equal to ~ 0.25. This convention originated in the early research on metals over twenty years ago. It is acceptable as far as the introduction of analysis error is concerned. However, no one is very sure about whether such a choice is optimum, especially given the types of materials studied have been extended.

Studying ion-implanted silicon is one of the standard applications of slow

positron beam. It is useful to determine the optimum ROI that should be employed in the work on silicon. In this chapter the relation between the optimum ROI and crystalline orientation and energy resolution has been obtained by theoretical simulation. An experiment on boron implanted <100> silicon is performed to test the simulation.

3.2 Simulation

3.2.1 Procedure

Recently Hakala *et al* have calculated the momentum distribution of electron-positron pairs annihilating at all kinds of vacancy clusters (V, V_2, V_3, V_4 and V_5) and the bulk in silicon for the first time[10]. Their work proved to be reliable and useful in guiding the experiments[58, 59, 60, 61]. The simulation here started with Hakala *et al*'s theoretical Doppler broadened spectra. Because divacancy (V_2) is the most common vacancy-type defects in ion-implanted Si, only V_2 was taken into account at the present time. Then the theoretical Doppler broadened spectra of both V_2 and bulk in three different orientations were convoluted with Gaussian functions of FWHM(full width at half maximum) corresponding to experimental energy resolutions(1 to 2 keV). Figure 3.1 shows the convoluted Doppler broadened spectra of bulk and V_2 in <111> silicon with an energy resolution of 1.2 keV. The difference between them is also plotted. The abscissa is the energy shift from 511 keV. It is clear that the central area of the spectrum of V_2 is larger than that of the bulk. It agrees with the fact that thermalised positrons annihilate with more low momentum electrons in V_2 than in the bulk. Subsequently, for S parameter, a variety of regions between - 3.9203 keV and 3.9203 keV were tried by reducing them from both sides with a step of 0.0933 keV. For W parameter, the regions between the intersection point, where the spectrum difference between divacancy and bulk is zero, and the end point, where the spectra decrease to zero, were tried like that for S (the results would be multiplied by 2 to obtain the whole wing area A). S_d (W_d), S_b (W_b), S_d/S_b (W_d/W_b) and figure of merit (see below) were calculated for every ROI.

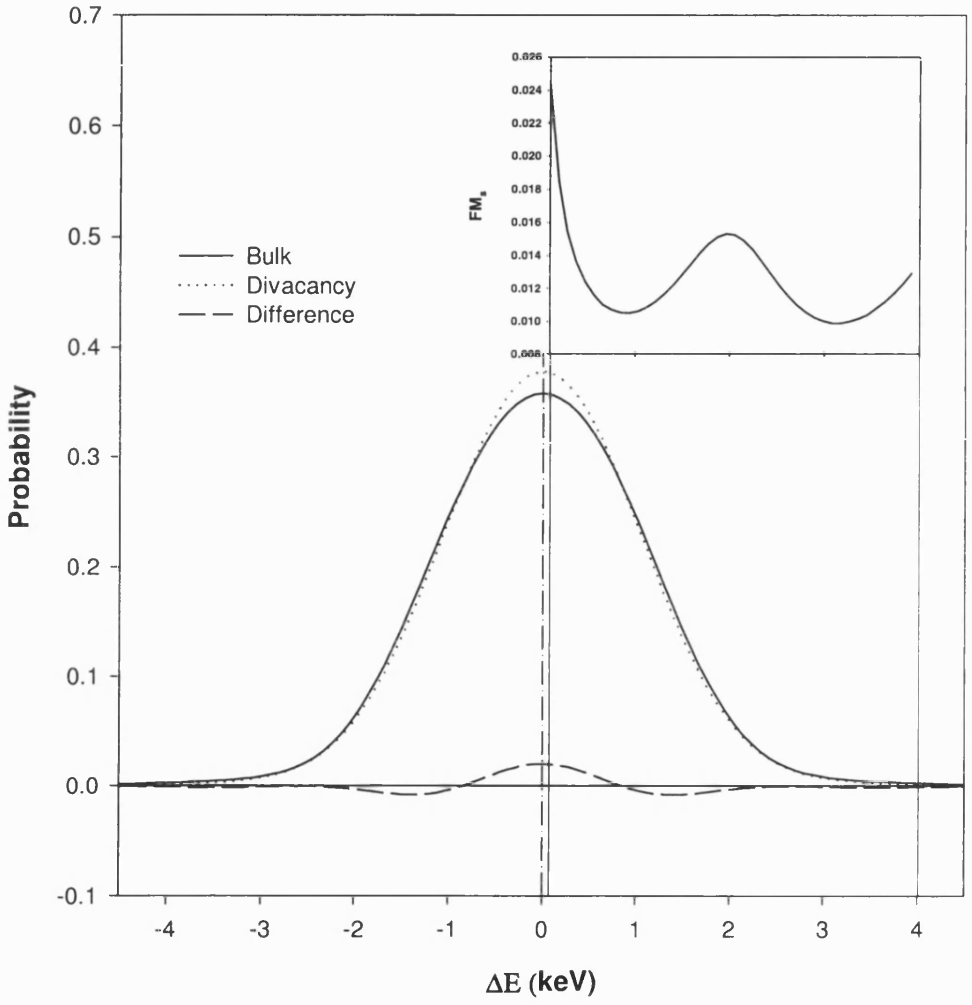

Figure 3.1: Convoluted Doppler-broadened spectra for bulk <111> Si and for a divacancy in <111> Si with a detector energy resolution of 1.2 keV and the difference between the two spectra. Abscissa: energy shift from 511 keV. Inset: FM_S vs. half-width of ROI for energy resolution of 1.2 keV (same energy shift values as main axis).

3.2.2 Figure of merit

In order to evaluate how good the selected ROI, a figure of merit was incorporated in the analysis. If

$$r = \frac{S_d}{S_b}, \tag{3.1}$$

the expression, $\Delta r/(r-1)$, where Δr is the standard deviation of r, can signify the uncertainty and sensitivity of the measurement to defects. Here $\Delta r/(r-1)$ is named figure of merit (FM_s). The smaller the FM_s, the better compromise between uncertainty and sensitivity. The optimum ROI should be able to minimize FM_s. Allowing for

$$\Delta r = \sqrt{(\frac{\partial r}{\partial S_d}\Delta S_d)^2 + (\frac{\partial r}{\partial S_b}\Delta S_b)^2}\ , \tag{3.2}$$

one can obtain an expression as follows by making substitutions of $\frac{\partial r}{\partial S_d}$ and $\frac{\partial r}{\partial S_b}$:

$$\frac{\Delta r}{r} = \sqrt{(\frac{\Delta S_d}{S_d})^2 + (\frac{\Delta S_b}{S_b})^2}\ . \tag{3.3}$$

From the definition of S, given $T = A + C$, similar to the calculation of $\frac{\Delta r}{r}$,

$$\frac{\Delta S_d}{S_d} = \sqrt{\frac{T_d - C_d}{T_d C_d}} \tag{3.4}$$

and

$$\frac{\Delta S_b}{S_b} = \sqrt{\frac{T_b - C_b}{T_b C_b}} \tag{3.5}$$

can be derived. In the derivation S is deemed as a function of C and A. It is also assumed that ΔC and ΔA are $\sqrt{C}$ and $\sqrt{A}$, respectively. Substituting equation

(3.4) and (3.5) into equation (3.3), then combining the result with equation (3.1), FM_s can be written as:

$$FM_s = \frac{S_d}{S_d - S_b}\sqrt{\frac{T_d - C_d}{T_d C_d} + \frac{T_b - C_b}{T_b C_b}} \,. \tag{3.6}$$

Analogical to FM_s, FM_w (the figure of merit for W_d/W_b) reads:

$$FM_w = \frac{W_d}{W_d - W_b}\sqrt{\frac{T_d - A_d}{T_d A_d} + \frac{T_b - A_b}{T_b A_b}} \,. \tag{3.7}$$

The variables on the right of the equation (3.6) and (3.7) above can be obtained easily once the limits of ROI are determined. Therefore, FM_s and FM_w can be computed and compared when various ROI selections are made. In the present simulation, T_d and T_b were set as 10^7.

The inset of Figure 3.1 shows the relation between FM_s and the ROI in <111> silicon with energy resolution of 1.2 keV. The abscissa is the right limit of ROI for S. It can be seen that the smallest FM_s appears where ROI is very wide. The corresponding S_d/S_b is 1.004, which is too near 1 to demonstrate the sensitivity of a measurement to defects. Hence, the second minimum FM_s was chosen, which is slightly larger than the smallest one but the sensitivity is much better, to determine the optimum ROI. In all the simulation the similar treatment was applied if there are two minimum figures of merit.

3.3 Experimental procedure

540-micrometer-thick <100> orientated single crystal silicon was used. It was implanted with 1.5 MeV B^+ to a dose of 10^{15} cm^{-2}. From a preliminary experiment it was known that there was a saturated peak in the plot of S versus incident positron energy in this sample. The saturated peak appeared at 14 keV of incident positrons. Owing to the high implantation energy, the S parameter

could not reach the bulk value (i.e. not all the thermalised positrons annihilated in the defect-free bulk) even though the positron energy was 30 keV. However, when the positron beam entered the sample from backside (opposite to the boron implantation surface) with energy of 24 keV, all the thermalised positrons would stop where there were no defects. In order to minimize the statistic errors, $\sim 10^8$ counts were collected in each incident positron energy by a high purity germanium detector with the energy resolution of 1.44 keV. The distribution of the total counts in 511keV photons peak was analyzed in the computer program Genie 2000.

3.4 Results and discussion

Figure 3.2 shows the optimum ROI as a function of detector energy resolution. The effect of crystalline orientation is also demonstrated. In Figure 3.2 (a) the left-hand ordinate is the right limit of the optimum ROI for S (its left limit is symmetric with respect to the centroid of the Doppler broadened peak). The left-hand ordinate is the left limit of the right part of the optimum ROI for W in Figure 3.2 (b). Given the counts around the end of the peak are very small, the limit close to the end of the peak can make little difference when the ROI for W is considered. Therefore, the treatment of the limits of the optimum ROI for W, i.e., only the one near the centroid is considered, is reasonable in Figure 3.2 (b). S_b or W_b associated with every optimum ROI is also illustrated as the right-hand ordinate in Figure 3.2. The solid lines are the results of second-order regression.

It can be easily seen that both the right limit of the optimum ROI for S and the left limit of the right part of the optimum ROI for W go up with the increase of energy resolution. It means the optimum ROI for S increases and that for W decreases when the energy resolution increases. This is because higher (worse) energy resolution results in stronger smearing of the Doppler broadened spectrum. In the meantime, we can readily find that there is an anisotropy between different crystalline orientations, i.e., the optimum ROI is not the same for each orientation although the energy resolution is the same. It has been proved by theoretical and experimental work that the anisotropy really exits in the Doppler broadened

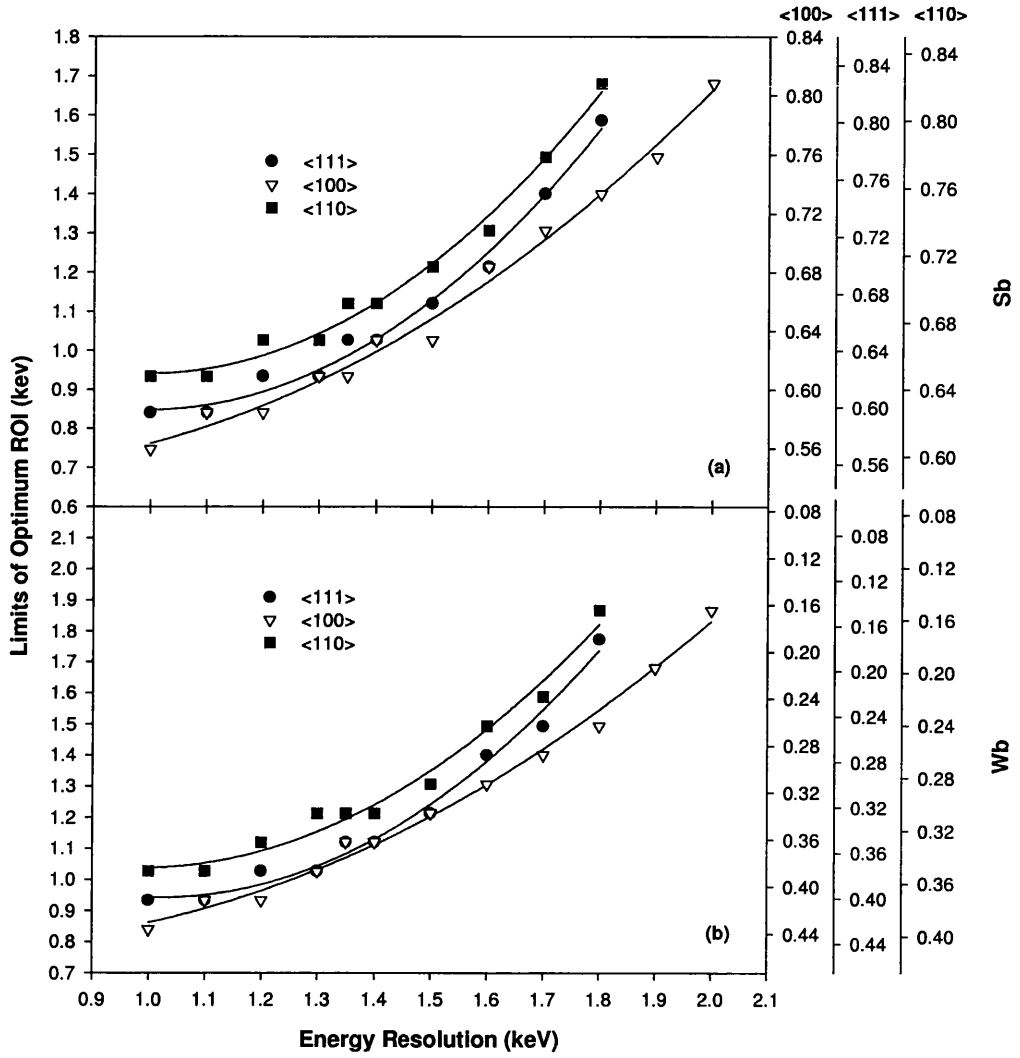

Figure 3.2: .Optimum ROI for (a) S and (b) W versus detector energy resolution in Si with different crystalline orientations. Left-hand ordinate: (a) half-width of the optimum ROI for S, (b) inner limit of the optimum ROI for W. Right-hand ordinate: S_b or W_b for every optimum ROI. Solid lines: second-order regression fits.

spectra of silicon bulk and negligible anisotropy in the spectra of divacancy[59, 10, 60]. Therefore the differences between different orientations should be attributed to the bulk's anisotropy. The different scales of S_b for different orientations can also demonstrate this point, i.e., for the same ROI S_b will change if the orientation is different. In the region of energy resolution between 1.2 and 1.6 keV, into which the experimental energy resolution usually falls, the differences of ROI between <111> and <100> are rather small. Therefore, it is suitable to adopt the same ROI for <111> and <100>. When the orientation is changed to <110>, however, it is necessary to adjust the ROI to make an optimum measurement. It is concluded that the ROI must be chosen in terms of both the energy resolution and the orientation.

It is noteworthy that in the usual experimental energy resolution region (1.2 - 1.6 keV) S_b and W_b linked to the optimum ROI are not 0.5 and 0.25, respectively. S_b is exclusively larger than 0.6 except that S_b of <100> orientation at 1.2 keV resolution is slightly smaller. Meanwhile, W_b is larger than 0.25 except that for <110> orientation the conventional 0.25 is still suitable around 1.6 keV resolution. The present simulation suggests that empirical values of S_b and W_b which are used to determine the ROI should be revised in order to optimize the characterization of the defects in silicon

Figure 3.3 shows the relation between S_{2v}/S_b or W_{2v}/W_b and the energy resolution under different orientations when the optimum ROIs are chosen. Here S_{2v} (W_{2v}) denotes S_d (W_d) of divacancy. The solid lines are still the results of second-order regression for the data dots. From Figure 3.3 (a) we can see S_{2v}/S_b decreases with the increase of energy resolution. The closer to 1 S_{2v}/S_b is, the worse the sensitivity of the measurement is. It can be derived that if the optimum FM_s is insisted, the sensitivity will decrease with the increase of resolution. It should be noted that there is no data for resolution greater than 1.8 keV under <111> and <110> orientations. The reason is that only one minimum FM_s (FM_w) in all the tried ROIs, whose corresponding S_{2v}/S_b(W_{2v}/W_b) is too close to 1. Accordingly, we suggest that under the above circumstances the ROIs are chosen to be the same to those for 1.8 keV. As seen in Figure 3.3 (b), the change of W_{2v}/W_b with the increase of resolution is different from that of S_{2v}/S_b . On one hand, the change is not as significant as that of S_{2v}/S_b .

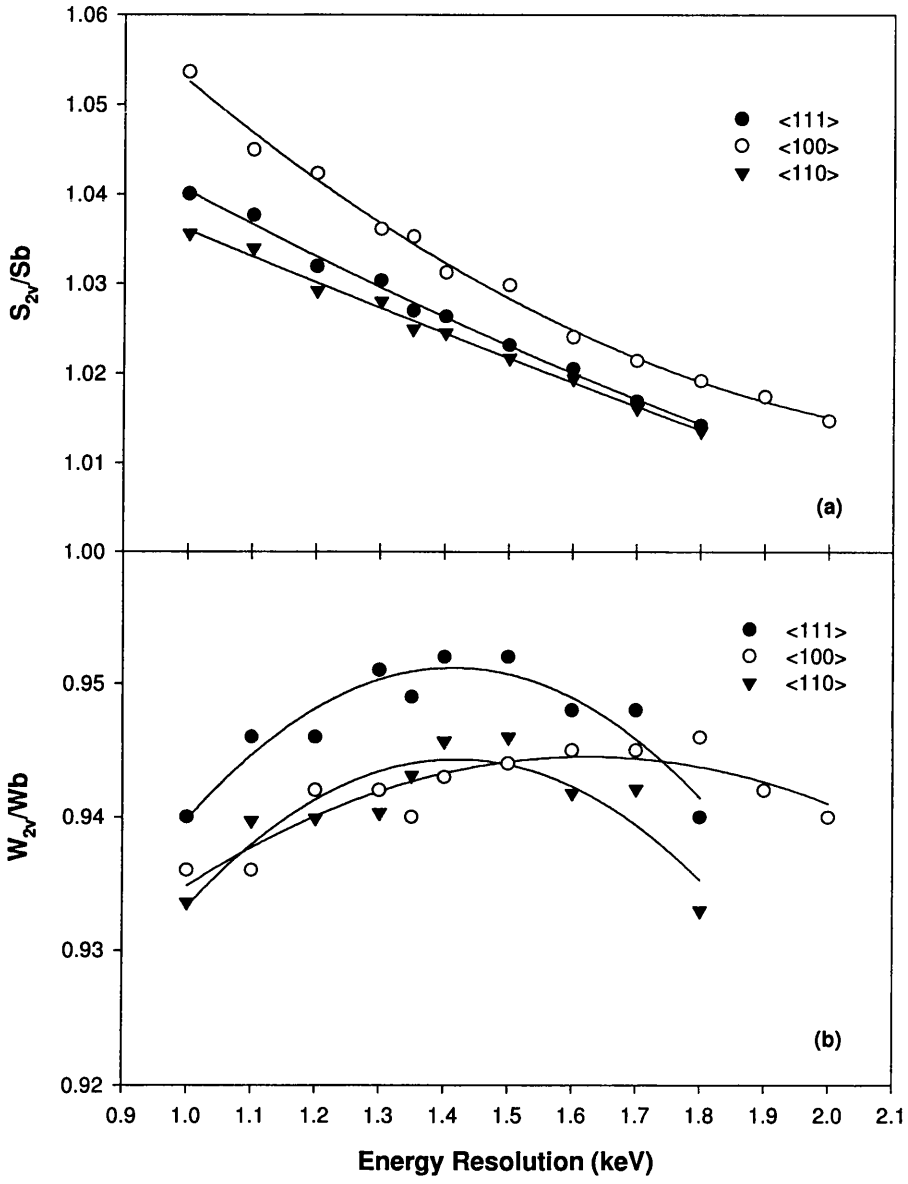

Figure 3.3: (a) S_{2v}/S_b and (b) W_{2v}/W_b vs. detector energy resolution in Si with different crystalline orientations when the optimum ROIs are chosen. Solid lines: second-order regression fits.

On the other hand, its trend is firstly up and then down. The latter implies that the characteristic normalized wing parameter may be the same for different resolutions if the optimum ROIs are always chosen.

Now we are moving on to experimentally test the results of our theoretical simulation. Much work has suggested that divacancy is the dominant open-volume defects in ion-implanted silicon at room temperature[37, 62, 38]. Recently Gebauer *et al* have also concluded that divacancy is the dominant open-volume defect in boron implanted silicon with the dose up to 10^{15} cm^{-2} after room temperature annealing[63]. Thus, it is reasonable to consider that the Doppler broadened spectrum obtained at 14 keV of incident positron energy in boron implanted silicon is for the positron annihilation in divacancies. In addition, it is natural to regard the spectrum attained at 24 keV of incident positron energy as the bulk's spectrum. The 511 keV photon peaks of divacancy and bulk are analyzed like the simulation.

Figure 3.4 shows the FM_s (FM_w) as a function of S_b (W_b) in boron implanted <100> orientated silicon with our experimental energy resolution of about 1.44 keV. The corresponding S_{2v}/S_b (W_{2v}/W_b) is also plotted against S_b (W_b) as the right ordinate. Figure 3.4 (a) indicates that the FM_s decreases firstly and then increases, However, S_{2v}/S_b always decreases, with the increase of S_b. it is clear that the minimum FM_s, 3.13×10^{-3}, appears at S_b of 0.64. S_{2v}/S_b associated with such a minimum FM_s is 1.032. It can be seen that S_b is about 0.64 in Figure 3.2 (a) and S_{2v}/S_b is about 1.031 in Figure 3.3 (a) when optimum ROI is selected at the energy resolution of 1.44 keV. The results are in agreement with the simulation well.

Figure 3.4 (b) shows the FM_w and W_{2v}/W_b change with W_b in in the same boron implanted sample. It is indicated that the minimum FM_w, 2.81×10^{-3}, appears when W_b is ~ 0.34. The corresponding W_{2v}/W_b is 0.935. In simulation, they are 0.35 (Figure 3.2 (b)) and 0.944 (Figure 3.3 (b)), respectively, when the resolution energy is 1.44 keV. Allowing for the effect of background in the experiment, one should expect a slightly larger W_b when the optimum ROI is chosen. The experimental results, however, is smaller than that of theoretical simulation. Hence, the agreement between experiments and simulation in wing

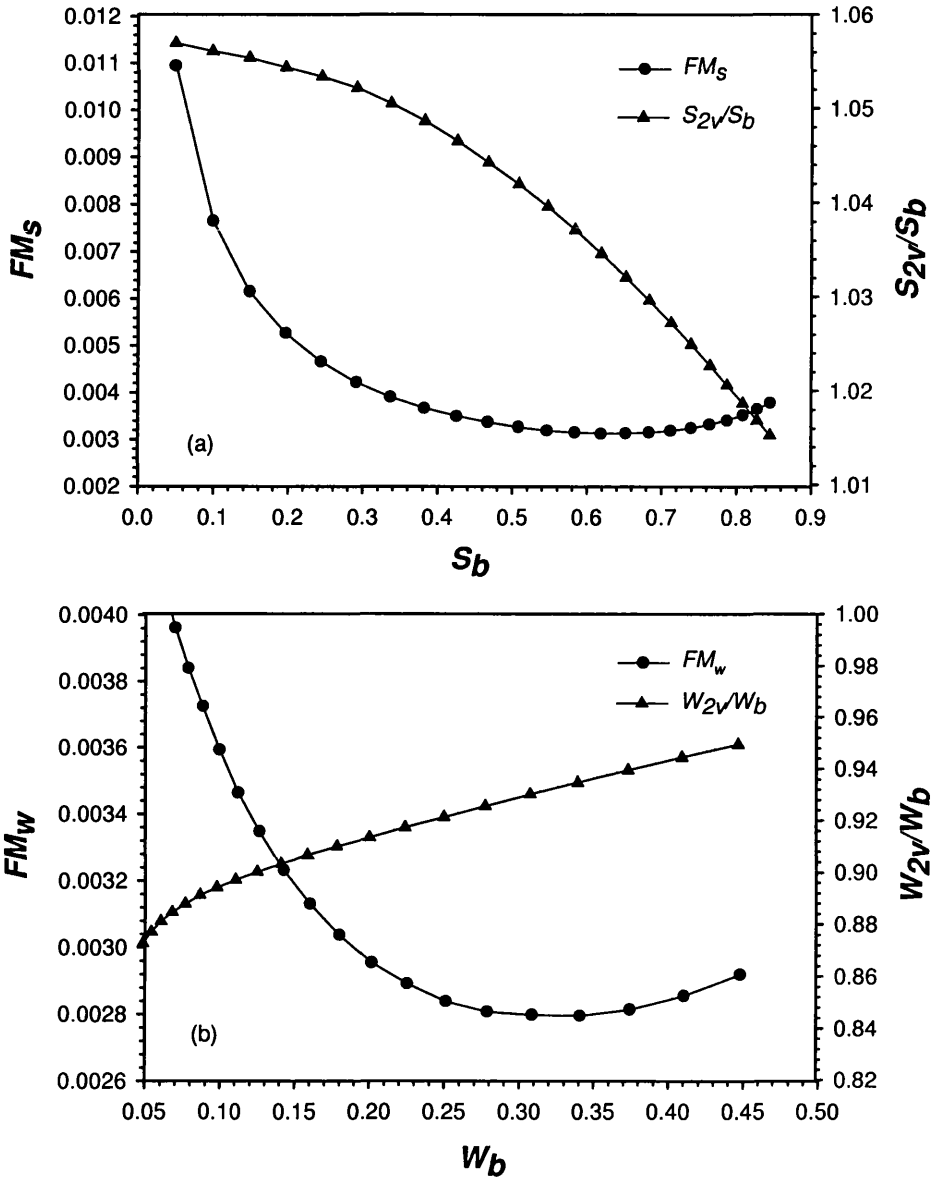

Figure 3.4: Experimentally-determined (a) FM_s vs. S_b and (b) FM_w vs. W_b for 1.5 MeV, 10^{15} cm^{-2} B$^+$-implanted <100> Si with an detector energy resolution of 1.44 keV. Right-hand ordinate: (a) S_{2v}/S_b and (b) W_{2v}/W_b.

parameter is not as good as that in shape parameter. Obviously, it should be pointed that both experiments and simulation demonstrate that the empirical W_b of 0.25 is not optimum to determine ROI. In terms of the more complexity in the wing parameter, generally speaking, the agreement between simulation and experiments is fairly satisfactory.

The effect of the background on S is negligible in practice[4]. If an accurate subtraction of the background is performed when W is used in experiments, the results from our simulation can be used to guide the experimental work correctly.

Finally, the figures of merits are compared when the optimum ROIs and conventional ones (resulting from making S_b 0.5 and W_b 0.25) are used. It is found that in the typical experimental energy resolution region (1.2 $\sim$ 1.6 keV) the promotion is usually smaller than 10%. For instance, it can be calculated in Figure 3.4 that FM_s and FM_w are decreased by 5% and 2%, respectively. Apparently, the improvements of FM_s and FM_w are not significant. However, it is suggested to use the best because there is no any especial cost. One of the reasons to turn to the optimum ROIs is the requirement of distinguishing some very small difference of defect concentration precisely. A proposal of diagnostic measurement of ion implantation dose with a positron beam has been made[64]. We will try to use the optimum ROIs to monitor the ion implantation doses within a change of 10% or even smaller, where the variation of defect concentration is rather small.

3.5 Conclusion

The choice of ROI in studying defects (divacancies) of silicon is simulated utilizing the theoretical Doppler broadened spectra. The experiment on boron implanted <100> silicon proves that the results from simulation are reliable and can be used to guide the experimental work. The optimum ROIs should be chosen for each system studied according to the crystalline orientation and detector energy resolution. The conventional choice of ROI, which results from the criterion of $S_b \sim 0.5$ or $W_b \sim 0.25$, is not the optimum one in work on vacancy-type

defects in silicon using the typical detector energy resolution. It is necessary to transfer to the optimum ROIs, especially in some measurement that requires higher sensitivity and smaller errors.

Chapter 4

Oxygen-Related Vacancy-Type Defects in Ion-Implanted Silicon

4.1 Introduction

Ion implantation has been one of the most important tools in Czochralski (Cz)-Si-based microelectronic industry. An inevitable outcome of ion implantation is the damage - mainly vacancy(V)- and interstitial(I)-type defects - induced by the incident energetic ions. It is well known that oxygen is one of the most important impurities in Cz Si, whose concentration is usually around 10^{18} cm^{-3}. Oxygen is also often used as the implanted ion to produce Si-on-insulator devices, which are very suitable for radiation-hardness, low-power and low-voltage application [65, 66]. Previous studies have demonstrated that oxygen readily reacts with Vs to form complexes in ion-implanted Si. These complexes can be effectively investigated by positron annihilation spectroscopy (PAS), which is a useful technique to detect V-type defects [4]. Fujinami [50] used PAS to study O-related defects in Si implanted with 180 keV O to a dose of 2×10^{15} cm^{-2} by annealing it from 300 to 800 °C. He found that O-V complexes evolved to multioxygen-multivacancy complexes and then to oxygen clusters finally around the ion-projected range (R_p). In addition, he showed that O-related multivacancy-based defects were also formed in the proximity of the surface, but their behaviour was not as com-

pletely described as those near R_p. In high-energy ion implantation this V-excess region exists at depths further away from the surface, and is therefore relatively unaffected by the surface or by the interstitials from the the end of range (EOR). Hence, following high-energy ion implantation, O-related V-type defects in this shallow region can be studied more clearly.

In the present work 0.5 MeV O-implanted Cz Si has been studied. 1 MeV Si-implanted Cz Si is also investigated in order to find the dependence of O-related V-type defects on oxygen concentration and distribution. It is found that V-dominated defects V_mO_n $(m > n)$ form in the shallow region and O-dominated defects V_xO_y $(x < y)$ form near R_p in both Si- and O-implanted Cz Si. The formation and evolution of these O-related V-type defects as a function of temperature are discussed in this chapter.

4.2 Experimental procedure

P doped, 2 - 4 Ωcm $< 100 >$ Cz Si samples implanted with 0.5 MeV O to a dose of 5 $\times 10^{15}$ cm^{-2} and with 1 MeV Si to a dose of 10^{16} cm^{-2} were used. The implantation was performed at room temperature with a tilt of 7°. The samples were then annealed at different temperatures with electron beam bombardment in vacuum. The annealing time was about 10 seconds at every temperature.

Beam-based PAS was employed to measure all the as-implanted and annealed samples at room temperature.The variable measured by PAS is the Doppler-broadened line-shape parameter S [4]. The value of S is larger when positrons annihilate at vacancies than in defect-free Si. However, when vacancies are decorated by oxygen, the value of S can be reduced to below that measured in defect-free Si [67]. The program called VEPFIT [57] was used to analyze the measured S versus incident positron energy E. In this work VEPFIT adopted a layer structure fitting mode in which there was a general S parameter for each layer in a sample. The general S was the average of the measured S values who were associated with a specific layer. A good and reasonable fit of the experimental data gave the boundaries and general S for each layer.

Another program, FAST (Fractions in Annihilation STates) was also used in this work. FAST employs a technique also used by van Veen *et al* [57] in which three annihilation gamma spectra (i.e., the 511 keV photopeaks measured by a Ge detector), associated with positron annihilation at the Si/SiO_2 surface, in divacancies (V_2) and in the Si bulk, are combined in appropriate proportions to fit the measured spectra from the samples. The proportion of each spectrum used for the fit then gives directly the fractions of positrons annihilated at the surface, in V_2-type defects, or in bulk Si. The standard spectrum for the surface was obtained by calibrating the spectrum from the annihilation of 2 keV implanted positrons in a virgin silicon sample with natural oxide on the surface (the effect of epithermal positrons is negligible). The other two were recorded by implanting 30 keV positrons into the virgin sample and 14 keV positrons into a silicon sample implanted with 1.5 MeV B to a dose of 10^{15} cm^{-2}, for which there was saturation trapping of positrons in V_2 defects [68], respectively.

4.3 Results and discussion

The positron measurements for Si- and O-implanted Cz Si samples are shown in Figures 4.1 and 4.2, respectively. The S parameters presented here have been normalized with respect to that for the bulk (defect-free layer) of these samples for which the S is thus 1. It can be seen that in the as-implanted samples the values of S are exclusively larger than 1 except for those near the surface (low E), which are lowered by the presence of oxide at the surface. This means that there are V-type defects in the as-implanted samples, and that their distribution extends to depths such that the values of S at $E = 30$ keV (corresponding to a mean probed depth $\overline{z} \sim 4$ μm, according to the expression $\overline{z}(\text{nm}) = 17E(\text{keV})^{1.6}$) are still larger than 1. Such a deep distribution of defects is a natural result of high-energy ion implantation, and has been observed in previous work [50, 69, 70].

Figures 4.3 and 4.4 show the fitted S values characteristic of each layer in Si- and O-implanted samples, respectively. The distributions of ions in the as-implanted samples predicted by the simulation code TRIM [22] are also included. In both as-implanted samples the S values for the defective layers are ~ 1.041,

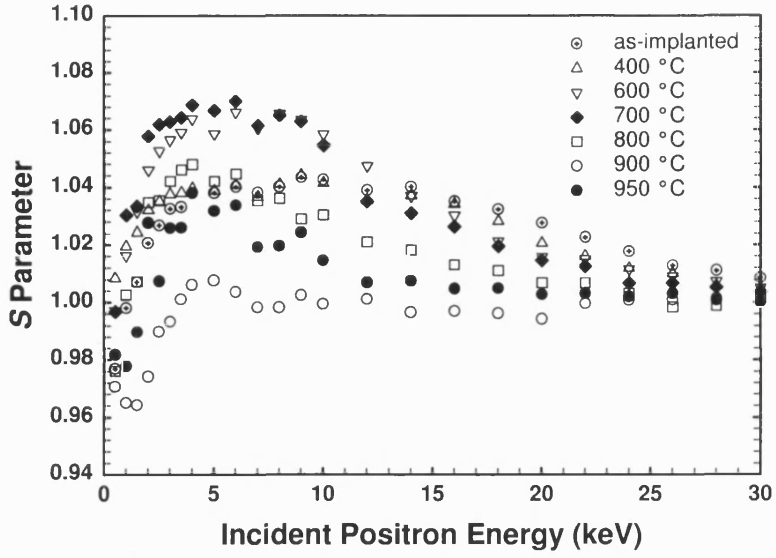

Figure 4.1: S parameter versus incident positron energy measured in Si-implanted Cz Si (1 MeV, 10^{16} cm^{-2}) after implantation and annealing at different temperatures.

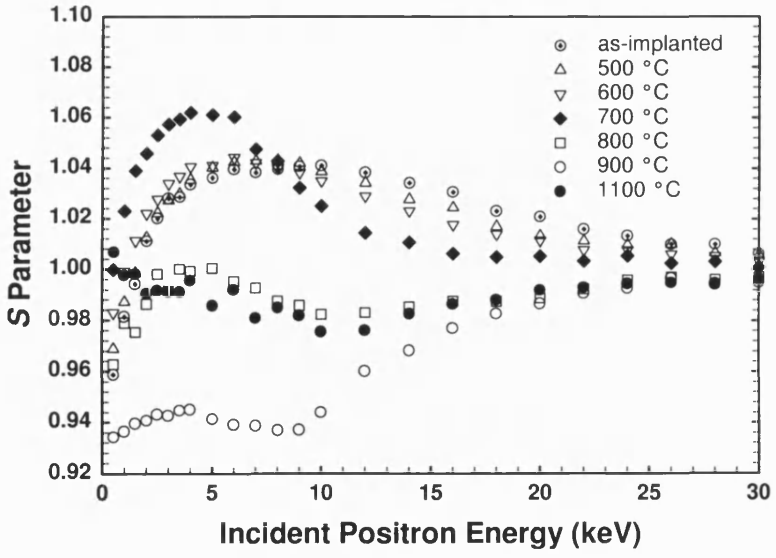

Figure 4.2: S parameter versus incident positron energy measured in O-implanted Cz Si (0.5 MeV, 5×10^{15} cm^{-2}) after implantation and annealing at different temperatures.

characteristic of V_2 with our slow positron beam [68]. Therefore, it is considered that V_2 are the dominant V-type defects in O and Si as-implanted samples, and that the saturation of positron trapping in V_2 is reached owing to the high implantation doses.

In the Si-implanted sample $S(E)$ (Figure 4.1) does not change until the temperature reaches 400 °C. The first change is seen only in the region beyond R_p (1300 nm). It is well known that in Cz Si V_2 are annealed out at $\sim$ 250 °C to form V_2O. At $\sim$ 400 °C these form V_3O or V_2O_2, which at 440 °C form V_3O_2, and which finally at 475 °C change to more advanced complexes [71]. It is believed that in our Si-implanted sample V_2 mainly evolve to V_3O in the region $< \sim$ 1600 nm at 400 °C. The positron lifetime in V_3O (325 ps) is close to that in V_2 (320 ps) [71], and it is supposed that their corresponding characteristic S values may also be very similar. Therefore, the S curve is not changed by this evolution in the region $< \sim$ 1600 nm. It is clear in the raw data of Figure 4.1 that S decreases in the tail of the S curve at 400 °C, and this is confirmed in Figure 4.3, which shows that the value of S drops to unity between 1600 and 2000 nm. It is known that the region beyond R_p is I-rich. The annealing of vacancies depends strongly on the injection of interstitials from EOR [72]. Therefor we propose that, between 1600 and 2000 nm, I-V_2 combination, rather than the evolution of V_2 into V_3O, is dominant at 400 °C. The consequent disappearance of vacancies results in the decrease in S.

The situation is different in the O-implanted sample; the much higher oxygen concentration (predicted by TRIM to reach around $2 \times 10^{20} cm^{-3}$ - Figure 4.4) means that beyond R_p evolution of V_2 to more complex defects outweighs the recombination with interstitials. Oxygen is ready to react with vacancies to form O-V complexes, to which more vacancies or oxygen tend to adhere. It is seen in Figs. 2 and 4 that I-V_2 recombination is not dominant in the region beyond 1250 nm until the temperature reaches 500 °C, which is consistent with Fujinami's work [50]. At shallower depths V_2 can evolve to complexes more advanced than V_3O_2 (Figure 4.4), apparently with a characteristic S slightly larger than that for V_2. After annealing at 600 °C, the tail of S curve (Figure 4.2) continues to decrease, and the boundary between the bulk and the defective layer shrinks to just over 1000 nm (Figure 4.4). However, the value of S for the defective layer

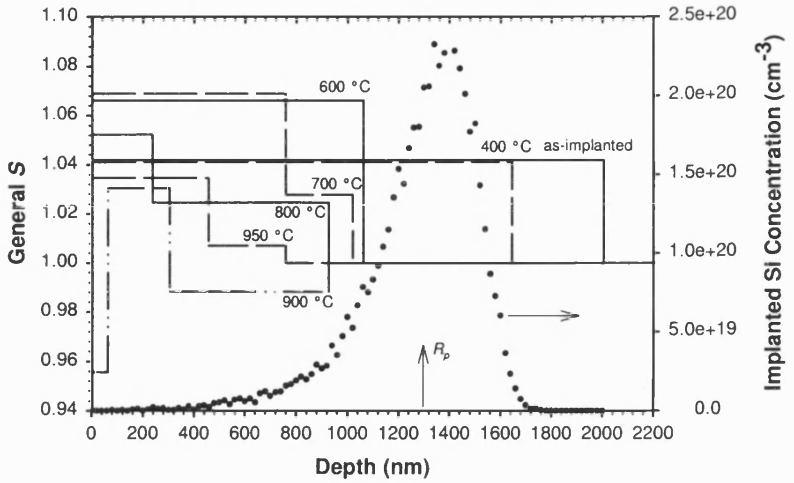

Figure 4.3: The change of general S with depth in Si-implanted Cz Si (1 MeV, 10^{16} cm^{-2}) for the as-implanted sample and after annealing to different temperatures, obtained from the fitting program VEPFIT. The implanted Si ion distribution, as calculated by the code TRIM, is also shown.

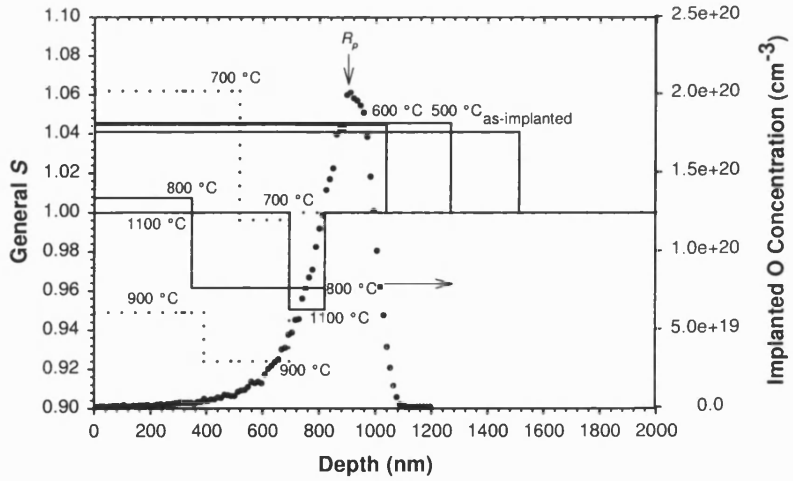

Figure 4.4: The change of general S with depth in O-implanted Cz Si (0.5 MeV, 5×10^{15} cm^{-2}) for the as-implanted sample and after annealing to different temperatures, obtained from the fitting program VEPFIT. The implanted O ion distribution, as calculated by the code TRIM, is also shown.

remains nearly the same as that at 500 °C, suggesting that V_2 evolve to similar advanced O-V complexes at 600 °C as at 500 °C.

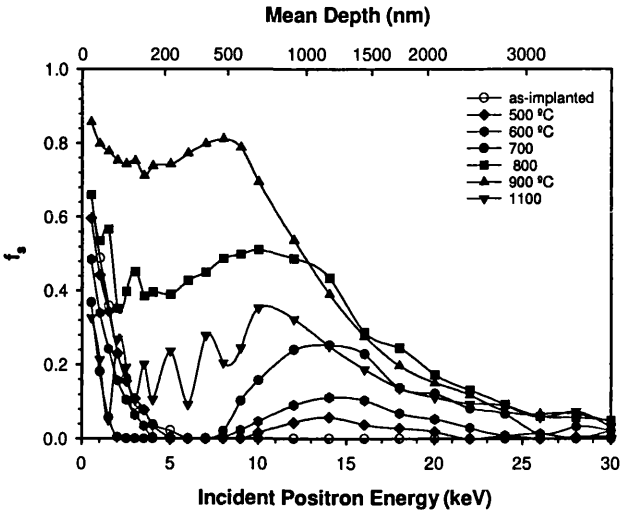

Figure 4.5: The fraction of positrons annihilated in the surface-like state for O-implanted Cz Si (0.5 MeV, 5×10^{15} cm^{-2}) obtained from the program FAST. The solid lines are used to guide the eye.

The insights into the formation of V_xO_y ($x < y$) in the O-implanted sample can be gained from the results of FAST fitting (Figure 4.5). Here the fraction of positrons f_s annihilated in a surface-like state is plotted against incident positron energy. Although the V-type defects are not V_2 exclusively, as assumed by FAST, the trend of the change of f_s is reliable. It is interesting that for annealing temperatures between 500 and 700 °C f_s are not zero at $E \sim 14$ keV (mean probed depth ~ 1000 nm). This does not indicate annihilation at the real surface; rather, that there are surface-like sites at depth ~ 1000 nm ($\sim R_p$), where the oxygen concentration is so large that oxygen atoms react with V_2 to form O-dominated clusters which are more advanced than the O-V complexes produced in the shallower region. These defects behave as positron traps in a way similar to the O-related surface state. However, the effect on S of this cluster formation is too small to be seen in the VEPFIT results (Figure 4.4) for the O-implanted sample annealed at 500 and 600 °C.

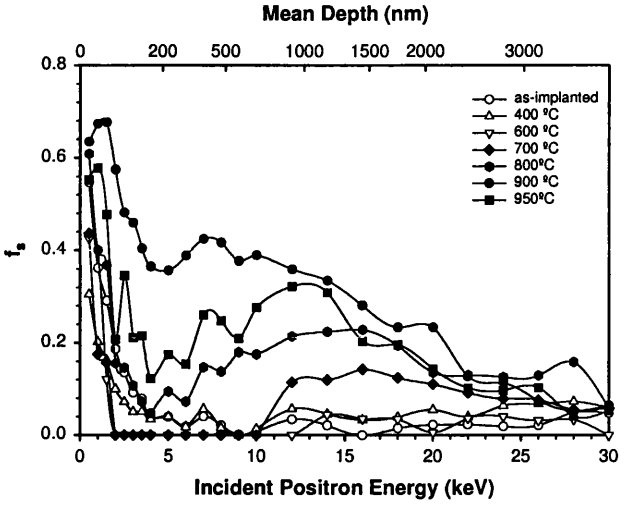

Figure 4.6: The fraction of positrons annihilated in the surface-like state for Si-implanted Cz Si (1 MeV, 10^{16} cm^{-2}) obtained from the program FAST. The solid lines are used to guide the eye.

When the Si-implanted sample is annealed to 800 °C, the defective layer continues to shrink (Figure 4.3). With the increase of temperature, besides the diffusion of interstitials from EOR, the diffusion of implanted Si ions, most of which are located around R_p, also happens [73]. Both of them can make the value of S decrease to be about 1 via the annihilation of vacancies. Therefore, it is seen that the boundary of defective layer decreases to $\sim$ 900 nm at 800 °C. In addition, the value of S in the shallow region is observed to increase significantly at 600 and 700 °C (Figures 4.1 and 4.3). This implies that V_2 evolve to advanced V-O complexes and finally agglomerate to form V_mO_n $(m > n)$, escaping the recombination with interstitials from R_p. It is also shown that the value of S in the region between 750 and 950 nm is much smaller than that in the shallower region at 700 °C (Figure 4.3). Figure 4.6 shows f_s for the Si-implanted sample. It is seen that a broad peak appears at high incident positron energies at 700 °C. As in O-implanted sample, it is believed that V_xO_y are formed between 750 and 950 nm. In this region V_mO_n are produced which then react with silicon diffusing from the R_p region to be transferred to V_xO_y. Apparently, not all V_mO_n are changed here so that the value of S is not decreased to be smaller than 1. Despite the

similarity between the reactions in the shallow region at 600 °C and 700 °C, the reaction near R_p is dominated by V-I recombination, which accounts for the absence of f_s signature at high energies in Figure 4.6 for temperatures below 600 °C. At 800 °C the second defective layer (Figure 4.3) becomes shallower and wider and its S continues to decrease. This implies that silicon ions can travel further toward the surface to transfer a part of V_mO_n to V_xO_y. This agrees with the increase in f_s in the shallower region (Figure 4.6). It can be observed that V_mO_n formed in the first $\sim$ 250 nm may also be affected by the silicon ions diffusing from the R_p region at 800 °C (Figure 4.3). The point is that the arriving silicon ions are limited so that few V_xO_y are produced.

At 700 °C in the shallow region in O-implanted Si V_2 evolve to advanced V-O complexes and agglomerate to form V_mO_n, resulting in a significant increase in S (Figures 4.2 and 4.4). It is interesting that the biggest values of S for V_mO_n appear at 700 °C for both Si- and O-implanted samples, signifying that V_mO_n are formed most effectively at 700 °C, while the maximum S for the latter is smaller because of the much higher oxygen concentration (Figures 4.3 and 4.4). This also proves that these vacancy-type defects are oxygen related in the shallow region. In addition, a higher oxygen concentration appears to results in the formation of more advanced V_mO_n, which has higher activation energy. Therefore, the temperature is higher for the commencement of V_mO_n formation in the O-implanted sample (700 °C) than in the Si-implanted sample (600 °C).

It is evident that f_s measured around 14 keV increases significantly at 700 °C in the O-implanted sample in Figure 4.5; here the two defective layers model works well. This implies that the formation of V_xO_y at 700 °C is more efficient than at 500 and 600 °C, so that the reduction in S is large enough to be seen by VEPFIT. At 700 °C a change similar to that in the shallow region occurs near R_p, except that many more oxygen atoms are involved. Hence V_xO_y are formed, rather than V_mO_n, reducing the value of S to below 1 (Figure 4.4). The boundary between the V_xO_y and the bulk is determined from VEPFIT to be at 700 nm, which is shallower than that at 800 °C (820 nm). This result may be not reliable because the S for the V_xO_y layer is very close to 1.

The value of S for the V_xO_y layer decreases to be far below 1 when the

O-implanted sample is annealed at 800 °C (Figure 4.4). Moreover, this layer extends towards the surface. These observations are consistent with the significant increase of f_s measured around 10 keV (Figure 4.5). At 800 °C the concentration of oxygen in the region between 350 and 820 nm increases owing to the diffusion of oxygen from the region around R_p[74]. This gives rise to an increase in the y:x in V_xO_y, resulting in a value of S much smaller than 1. The change of the boundary between defective and defect-free layer from 500 to 800 °C also benefits from the diffusion of interstitials from EOR, similar to the situation at 500 °C.

After annealing at 800 °C, the value of S in the first 340 nm decreases in O-implanted Si compared with 700 °C, which is the same as that in Si-implanted silicon. It is proposed that the ratio of oxygen to vacancy in the O-V defects increases, as near R_p, as a result of the diffusion of oxygen from around R_p. The increase in this ratio is also made apparent by the increase in f_s at E below 8 keV from zero to $\sim$ 0.4(Figure 4.5). The effective positron diffusion length in the first 340 nm is $\sim$ 56 nm, and the fraction of positrons implanted at 8 keV which diffuse back to the real surface is expected to be negligibly small. Hence, the above-mentioned increase in f_s must be linked to the effect of oxygen in the defects.

In addition, it should be noted that the decrease in S is more significant in the O-implanted sample than in the Si-implanted sample, due to the different formation mechanism of O-related V-type defects at 800 °C. In the Si-implanted sample interstitials reduce the number of vacancies in these defects, but the consequent decrease in S is tempered by the parallel decrease in the specific trapping rate associated with the defects. In the O-implanted sample the number of oxygen atoms in the defects is increased without significantly decreasing the specific trapping rate and, because positrons see more oxygen atoms, a substantial decrease in S is observed. This also explains the large increase in f_s in the shallow region at 800 °C in O-implanted Si (Figures 4.5 and 4.6).

When the O-implanted sample is annealed at 900 °C the values of S in both defective layers are reduced to well below 1 (Figures 4.2 and 4.4). It is believed that the profile of oxygen becomes less sharp because of the diffusion of implanted oxygen. The oxygen concentration in the near surface region ($<$ 390

nm) is increased enough to produce V_xO_y. However, the oxygen concentration between $\sim$ 390 and 700 nm is bigger after all because of the proximity of R_p, this introduces a larger y:x ratio in the resultant defects, and hence smaller S than at $<$ 390 nm (Figure 4.4). The formation of V_xO_y in the entire first 700 nm increases f_s measured at $<$ 9 keV significantly (Figure 4.5).

The boundary between the defective and defect-free layers is closer to the surface than at 800 °C (Figure 4.4). This is due to the recombination between vacancies and interstitials from the EOR. It is supposed that more interstitials can be injected and they can travel a longer distance at 900 °C.

It is shown that the layer between $\sim$ 300 and $\sim$ 900 nm is also characterized by an S smaller than 1 when the Si-implanted Si is annealed at 900 °C (Figure 4.3). It is believed that interstitials, whose concentration is increased significantly by the diffusion of implanted Si, can transfer V_mO_n, which are formed at $\sim$ 700 °C, to V_xO_y in this layer at 900 °C. A smaller decrease is seen in S for the layer between $\sim$ 60 and 300 nm, to a value still larger than 1, because a smaller number of interstitials diffuse to this shallower region. The significant effect of oxygen in the defects on positron annihilation is illustrated by the great increase in f_s in the shallow region between 800 and 900 °C (Figure 4.6). It can be also seen in Figure 4.3 that the value of S for the first $\sim$ 60 nm is much smaller than 1; it is likely that defects in this layer are associated with oxygen from the surface.

After annealing at 950 °C, S for the regions shallower than $\sim$ 900 nm exclusively increase in Si-implanted sample (Figure 4.3), implying that the all the O-related V-type defects begin to dissociate at this temperature. The first defective layer, whose width is smaller than $\sim$ 30 nm, is not shown in Figure 4.3. Oxygen atoms released following dissociation do not trap positrons effectively. Vacancies from the dissociation recombine with interstitials, whose concentration is mainly determined by the redistribution of implanted Si ions. Most of vacancies in the first 450 nm can escape the recombination with interstitials because of the low concentration of the latter, and hence S increases in this region. However, between 450 and 750 nm a fraction of the vacancies from the dissociation recombine with interstitials, and so a somewhat smaller increase in S is observed. In Figure 4.5 it is clear that the values of f_s at 12 and 14 keV at 950 °C are very close to those at

900 °C. Given the Makhov distribution of positrons and the much smaller f_s in the shallow region compared with those at 900 °C. It is believed that the values of f_s measured around 12 and 14 keV are actually larger than those measured at 900 °C. The region associated with these larger f_s is estimated to be around 900 nm. It is considered that oxygen clusters are formed in this region because high-concentration interstitials annihilate nearly all the vacancies so that the released oxygen atoms can migrate easily to agglomerate. However, the region is so narrow that it can't be demonstrated by VEPFIT.

It is presumed that V_xO_y also begin to dissociate at 950 °C in the O-implanted sample. Figure 4.4 shows that only one defective layer, with an S smaller than 1, exists between $\sim$ 700 and 800 nm after annealing at 1100 °C. This layer is beyond the two defective layers at 900 °C; this suggests that most of V_xO_y in the first $\sim$ 700 nm have dissociated. The residual defects are responsible for the non-zero values of f_s measured at from $\sim$ 4 to 8 keV (Figure 4.5). It is well known that oxygen precipitates grow effectively at a high temperature like 1050 °C [75], and we suppose that some defects in the region between $\sim$ 700 and 800 nm, probably surviving vacancies, can facilitate the nucleation of oxygen precipitates at 1100 °C. The precipitates give rise to an S smaller than 1 (Figure 4.4) and the high f_s measured at 10 keV (Figure 4.5). It is evident that oxygen precipitates do not appear beyond $\sim$ 800 nm although there is high oxygen concentration around R_p, because of the shortage of nuclei (the vacancy concentration is too low close to EOR). During the formation of oxygen precipitates interstitals may be emitted because of the relaxation of stress [76]. The vacancies resulting from the dissociation of V_xO_y in the first 700 nm can annihilate with the interstitials from both oxygen precipitates and the EOR or just diffuse out at 1100 °C. However, the oxygen concentration is not enough to make precipitates grow effectively in the first 700 nm, as happened in the region closer to R_p, and hence the value of S becomes nearly 1.

4.4 Conclusion

High-energy O- and Si-implanted Cz silicon samples have been studied by PAS. The evolution of V_2 to V-O complexes is out competed by V-I recombination at 400 and 500 °C in the Si- and O-implanted samples; the higher oxygen concentration makes the latter temperature higher. The defective region shrinks as the annealing temperature increases as interstitials are injected from the EOR. V_mO_n ($m > n$) are formed in the shallow region most effectively at 700 °C for both Si and O implantation. V_xO_y ($x < y$) are produced near R_p by the annealing. At 800 °C implanted Si ions diffuse and reduces m, and implanted O ions diffuse and increases n in V_mO_n. All O-related V-type defects appear to begin to dissociate at 950 °C, with the probable formation of oxygen clusters. At 1100 °C oxygen precipitates appear to form just before R_p in O-implanted silicon.

Chapter 5

Effect of Vacancies on the Behaviour of Fluorine in Silicon

5.1 Introduction

An incomplete picture of the basic behaviour of F in Si blocks the realization of its full potential in microelectronic technology, although it has been incorporated in Si in several device processes [77, 78, 79]. The incorporation of F is usually realized by ion implantation. The threshold dose of F to amorphize Si is $10^{15} cm^{-2}$. F is mobile only above 550 °C in both crystalline and amorphized Si. A strong surface-oriented diffusion has been observed in the former and, in the latter, F additionally accumulates at the amorphous-crystalline interface and in the extended interstitial(I)-type defects beyond the amorphous layer [80, 81]. By implanting high-dose BF_2 to obtain a region of high-density interstitials at the end-of-range (EOR) of implantation, Park *et al.* [82] proposed an interstitialcy mechanism of F diffusion with an activation energy (E_m) of 0.16 eV; this small E_m implies transient diffusion of simple I-F complexes. However, to date no unambiguous evidence has been gathered to demonstrate the effect on F diffusion of the other kind of damage induced by implantation, the vacancy (V). Szeles *et al.* [83] studied this using positron annihilation spectroscopy (PAS) [2]. However, no convincing model was presented because the low densities of F in their samples

gave no measurable PAS signature.

5.2 Experimental procedure

Implantation of F at high energy (0.5 MeV) and dose ($5 \times 10^{15} cm^{-2}$) produced a large number of vacancies in a wide region below the surface, separated from the I-rich region at EOR [84, 85], so that the effect of implantation-induced defects on F could be studied. Implantation of < 100 > Czochralski (Cz) Si (P doped, 2 - 4 Ωcm) was carried out at a tilt of 7°at room temperature at the University of Surrey Ion Beam Centre. The implanted samples were heated in vacuum by electron beam bombardment at 400 and 700 °C, being below and above the previously suggested critical temperature for F diffusion, for times ranging from 30 s to 125 h. Beam-based PAS and secondary ion mass spectroscopy (SIMS) were used to measure the as-implanted and heated samples. The as-implanted sample and that heated at 700 °C for 125 h were examined by cross-section transmission electron microscopy (XTEM). XTEM showed that the as-implanted sample remained crystalline although the dose was higher than the threshold value previously reported; this is due to the high implantation energy used here.

5.3 Results and discussion

Figure 5.1 shows the PAS results for the as-implanted sample and those annealed at (a) 400 °C for up to 67 h and (b) 700 °C for up to 125 h. The trapping of positrons at V-type defects leads to a higher Doppler-broadened line-shape parameter S defined as the central fraction of the annihilation line, compared with that for the defect-free lattice sites. The S values presented here have been normalized with respect to that for a bulk virgin Si sample for which S is thus 1. The mean depth sampled by implanted positrons is determined by their incident energy E (keV), and is $\sim 17E^{1.6}$ (nm). Figure 5.2 shows the F profiles in the as-implanted and annealed samples measured by SIMS. The implantation range (R_p) of 0.5 MeV F is $\sim$ 0.9 μm. By fitting the PAS data

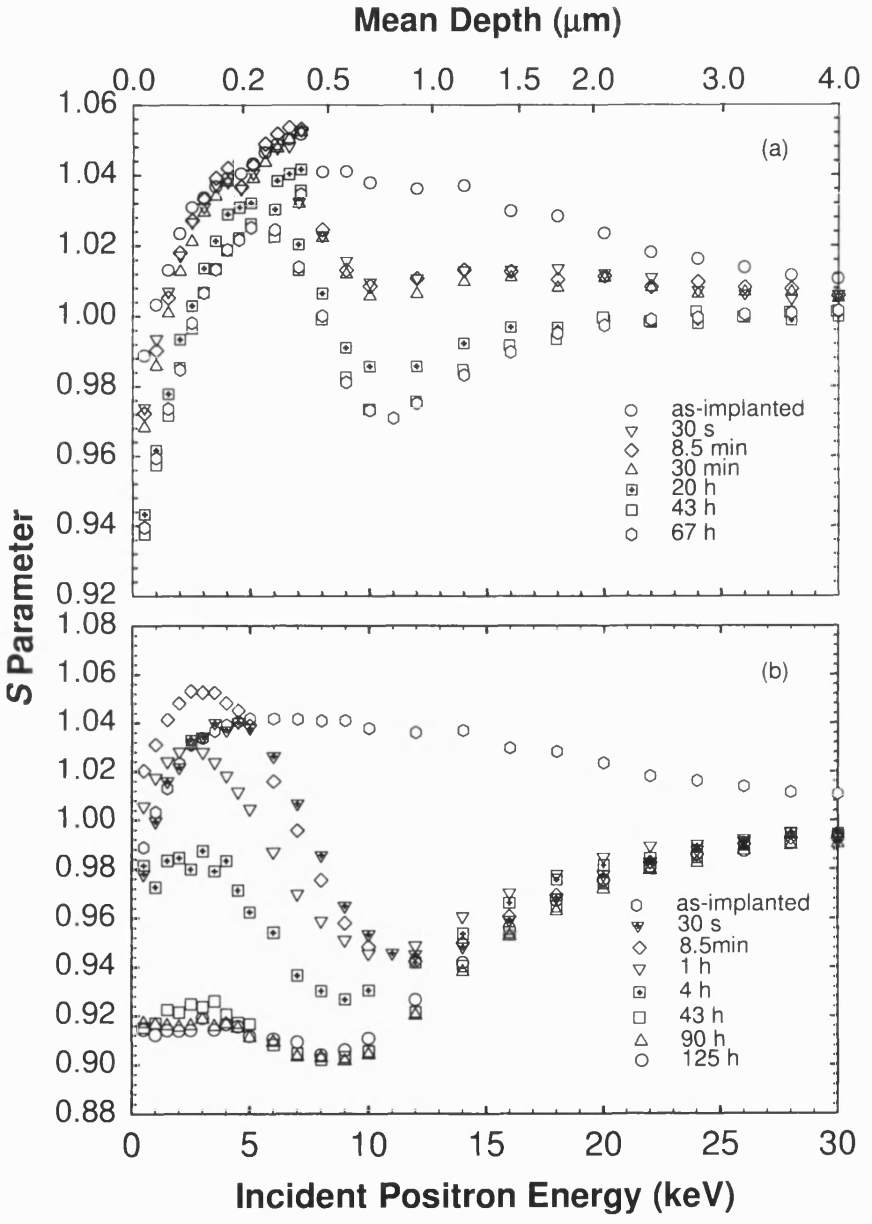

Figure 5.1: PAS results for the samples annealed at (a) 400 °C for up to 67 h and (b) 700 °C for up to 125 h.

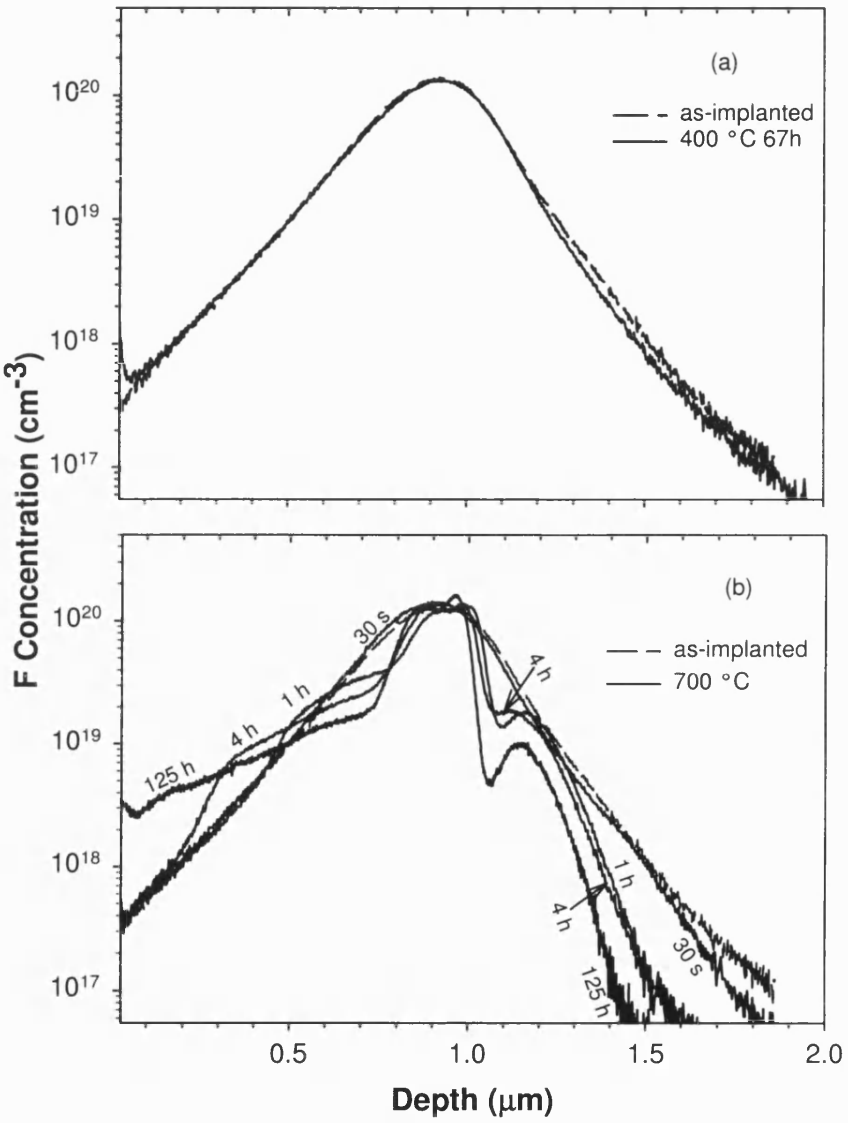

Figure 5.2: F profiles measured by SIMS in the as-implanted sample and those annealed at (a) 400 and (b) 700 °C.

using VEPFIT [57] we find that the vacancy distribution ends at around 2.3 μm; such an abnormally deep distribution of vacancies has been observed previously [69]. It is believed that F atoms react with interstitials effectively during ion implantation; this allows the survival of most of the vacancies, which can then migrate over long distances.

The peak value of S in the as-implanted sample is 1.042, characteristic of the divacancy (V_2) with our PAS setup [68]. It is reproducibly found that a dip appears around 11 keV (Figure 5.1) in the S curve for the as-implanted sample, which corresponds to the region close to R_p . This dip becomes obvious when compared with O implantation with the same implantation energy and dose, illustrated in Figure 5.3. Allowing for the similarity of mass of O and F, nearly the same defects should be introduced by implantation. However, the signal around 11 keV is quite different. It is well known that F and O reduce S when they are associated with vacancies because of the large momenta of their outermost-shell electrons [86, 67, 50]. Clearly, the effect of F on vacancy in as-implanted Si is more significant than that of O so that its signal is observable even with a single detector (the impurities associated with vacancies are usually only observed by a two-detector coincidence setup of PAS[87]). The argument that the dip is real and introduced by F is also supported by the gamma ray energy spectrum. Figure 5.4 shows the spectra divided by that for pure Si for several kinds of ion implantation into Si. The sensitivity to the presence of F, associated with positron annihilation with its high-momentum outermost-shell electrons, is evidenced by the unique bump at the high-momentum side (high channel number side) compared with other ion implantations including O. Therefore, we conclude that F has already decorated some vacancies around R_p because of the high F concentration there.

Figure 5.5 shows the changes in general S obtained by fitting the data of Figure 5.1 (a) in regions I (0 - 0.5 μm), II (0.5 - 1.1 μm) and III (1.1 - 1.8 μm) with time at 400 °C until equilibrium is reached after 43 h. It is interesting that there are still vacancies in the region beyond R_p although there is shrinkage from 2.3 to 1.8 μm during heating. SIMS shows that the F concentration is much less than $10^{18} cm^{-3}$ beyond 1.8 μm in the as-implanted sample (Figure 5.2 (a)). This low concentration facilitates V-I recombination (I being mainly in the form of

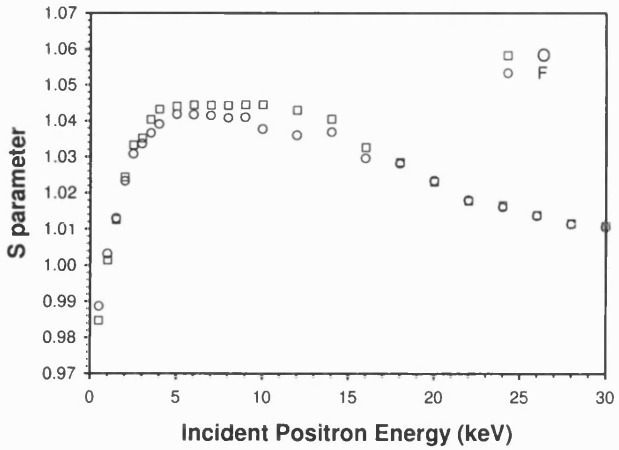

Figure 5.3: Positron measurements on F and O as-implanted Cz Si. For each ion the implantation dose and energy are 5×10^{15} cm^{-2} and 0.5 MeV, respectively. The dip around 11 keV is clear in F implantation when compared with O implantation.

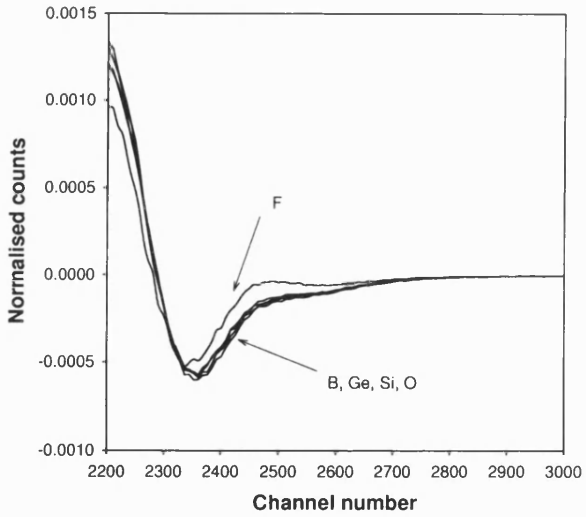

Figure 5.4: The gamma ray energy spectra, normalized to that for pure Si, of positron annihilation in Si implanted with different kinds of ions. The spectrum of F is measured at 11 keV positron energy in the as-implanted Si described in the text. Others are taken where the saturation of positron trapping takes place in high-dose implanted Si, and are indistinguishable from that for undecorated divacancy defects.

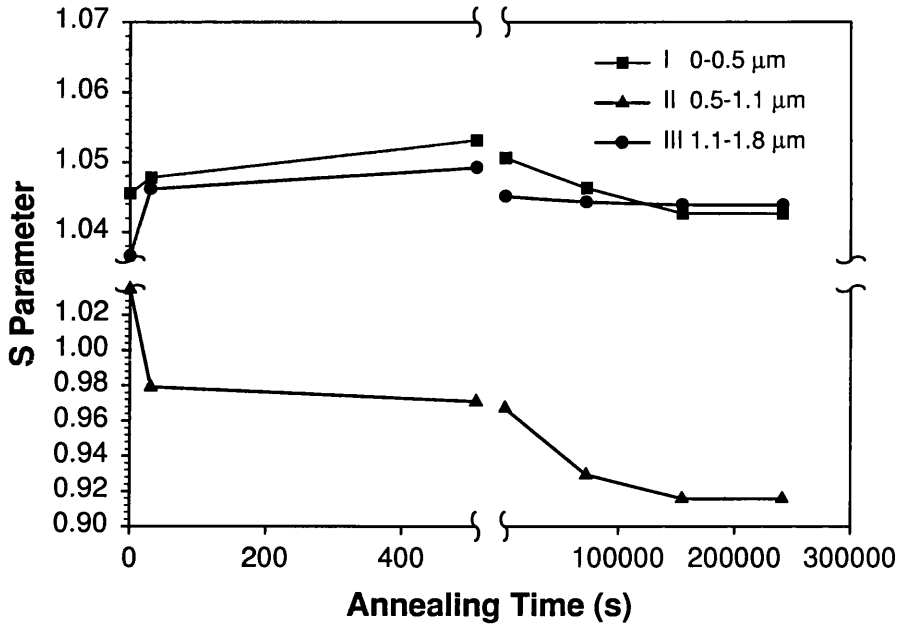

Figure 5.5: The change of general S values obtained from VEPFIT in different regions during annealing at 400 °C. The error bars are smaller than the symbols. The solid lines are used to guide the eye.

I-F complexes) rather than the formation of V-F complexes.

The formation of V-F complexes in region II is evidenced by the clear decrease of S (Figure 5.5). In contrast, the S values in region I and III increase to be between 1.046 and 1.057, characteristic of trivacancy (V_3) and quadrivacancy (V_4), respectively, in the first 8.5 minutes. The dominance of vacancy agglomeration up to the size of V_4 is a consequence of the lower F concentration in these two regions (Figure 5.2 (a)). After 8.5 minutes the S values in regions I and III begin to decrease. It is known that defect agglomeration usually proceeds via Ostwald ripening [88], in which dissociated components from small defects move to big ones to make them bigger. We believe that some of the dissociated vacancies can be lost to the surface from region I and to the bulk from region III. The effect of the loss of vacancies outweighs that of the increase of defect size, and so S decreases in these two regions after 8.5 minutes. Because of the high implantation energy, the vacancy distribution can be regarded as uniform in the V-rich region [89], and a V_2 concentration of $\sim 8.5 \times 10^{18} cm^{-3}$ in the region ≤ 1.1 μm can be estimated with VEPFIT from PAS in the as-implanted sample. It is clear that the

F concentration is higher than the vacancy concentration in region II. We believe that F-dominated V-F complexes are produced so that the S value becomes smaller than 1 after a long annealing time. In region I, however, V-dominated V-F complexes are formed. Hence, the S value in this region is always larger than 1. Region III is I-rich because it is well beyond R_p; it is supposed that some isolated F is left after the formation of I-F complexes in this region in the as-implanted sample; and that this initiates the formation of V-dominated V-F complexes, out-competing the V-I reaction (I being mainly in I-F complexes) at 400 °C. S is thus still larger than 1 even after a long annealing time. The existence of V-F complexes in region III, again, implies that F can prevent V-I recombination by forming complexes.

Figure 5.2 (a) shows that after 67 h annealing at 400 °C the F concentration below $\sim$ 1.1 μm is appreciably unchanged, consistent with the earlier observations that implanted F does not diffuse below 550 °C. This apparently contradicts the PAS results described above, i.e., that F migrates to form V-F complexes. E_m values of 0.6 - 1.6 eV for interstitial F[90], and 1.3 eV for V_2[91] mean that they both can diffuse at 400 °C. However, they trap each other to form V-F complexes once they meet. In region II, for example, the F concentration is $\sim 10^{20} cm^{-3}$ and the mean distance between F and V_2 is estimated as 2.4 nm. It is considered that F travels less than this distance to react with V_2. This is a quick stage, illustrated by the significant decrease in S after the first 30 s annealing at 400 °C (Figs. 1 (a) and 3). After that the agglomeration of V-F complexes takes place slowly via Ostwald ripening, and S changes very slowly with time in region II. The distance travelled by the simple V-F complex lies between 2 and 5 nm. The best depth resolution of modern SIMS is $\sim$ 3 nm (more generally 10 nm)[92], and so it is not able in this case to demonstrate F migration at 400 °C. Assuming a random walk mechanism we estimate that E_m for simple V-F complexes is 2.12 $\pm$ 0.08 eV with the expression $N = \nu t \exp(-E_m/kT)$, where N is the jump number given by $(R/d)^2$ (R is the diffusion distance and d is 0.23 nm, the nearest neighbor distance in Si), ν is the Debye frequency ($\sim 10^{13}$ Hz) and t is the migration time (43 h). It is clear that F diffuses in the V-rich region in the form of simple V-F complexes, i.e., via a vacancy mechanism, although the higher E_m of these V-F complexes makes F less mobile than in the interstitial state.

It is seen in Figure 5.2 (a) that the F concentration beyond $\sim$ 1.1 μm decreases somewhat after 67 h annealing at 400 °C. In region III simple I-F complexes, which are formed either in the as-implanted sample or during the Ostwald ripening of I-type defects, diffuse into the bulk to cause the F concentration to decrease.

The PAS results for annealing at 700 °C for up to 125 h are shown in Figure 5.1 (b). After 30 s it is found from VEPFIT that the V-type defects disappear in the region beyond $\sim$ 1 μm. This is a more significant shrinkage than at 400 °C, suggesting that V-I recombination is significantly enhanced at 700 °C even though a comparatively high F concentration exists.

After 30 s annealing a large decrease of S appears at about 11 keV. VEPFIT shows that the general S in the region from 0.5 to 1 μm becomes smaller than its equilibrium value in this region after annealing at 400 °C. This implies significant formation of advanced F-dominated V-F complexes in this region. F can travel farther at 700 °C than at 400 °C, and the change of F profile is clearly seen by SIMS. In the region shallower than 0.5 μm, however, S increases and, as in the initial stage of annealing at 400 °C, V_2 agglomerate up to the size of V_4.

After 8.5 minutes annealing at 700 °C, the shallow region is shown by VEPFIT to contract to $\sim$ 0.4 μm and its S increases to between 1.057 and 1.068, characteristic of V_4 and V_5, respectively, suggesting that the defects up to the size of V_5 are formed. With time the agglomerates grow and the vacancy density decreases in an Ostwald ripening process. S in the shallow region decreases although there is no change in F concentration after 1 h annealing. The S value for the shallow region would not become smaller than 1 if only vacancies were lost. F migrating from around R_p introduces a further decrease in S. Therefore, the widening of the region with a low S is observed, which is illustrated by the motion of the dip of S curve from the original $\sim$ 11 to $\sim$ 8 keV after 43 h annealing (Figure 5.1 (b)). It is seen in Figure 5.1 (b) that after 90 h there is no more change in the S curve and F ceases to migrate (otherwise, S would continue to decrease to be at least the value seen at $E \sim 7$ keV). The Ostwald ripening of agglomerates in the shallow region is also thought to be completed at 90 h. The flat part of S curve after 90 h corresponds to the first $\sim$ 0.4 μm in the sample. This is consistent

with the rather uniform distribution of vacancies in the shallow region and the small F concentration gradient there after a long annealing time (Figure 5.2 (b)).

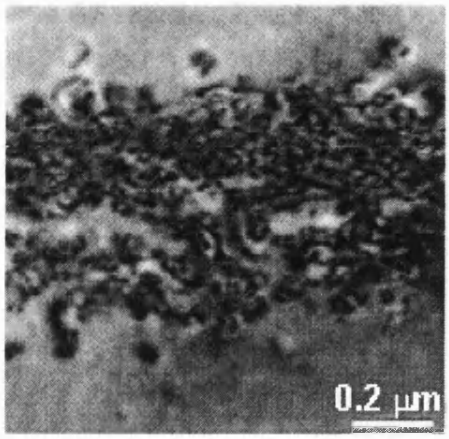

Figure 5.6: XTEM image of the annealed F-implanted Si (700 °C, 125 h). The upper limit of F precipitates is at 0.75 μm depth.The top-band precipitates develop from V-type defects. The bottom-band precipitates develop from I-type defects.

Figure 5.6 shows the XTEM image of the sample annealed at 700 °C for 125 h. It is clear that there are two bands of F precipitates formed in this sample whose locations are consistent with those of two main SIMS F peaks shown in Figure 5.2 (b). F precipitates can be developed from both V- and I-type defects. V-F complexes formed around R_p (0.75 - 1 μm) can act as the nuclei of F precipitates. The other F peak, in the I-rich region from 1 - 1.3 μm, appears after only 1 h annealing. Extended I-type defects such as {311} are generated at EOR at 700 °C[93], and these serve as the nuclei of F precipitates. Between the two bands of F precipitates the numbers of V and I are closely matched, so that during annealing mutual annihilation leaves very few V- or I-type defects to act as the nuclei of F precipitates.

The F concentration beyond $\sim$ 1 μm decreases with time during annealing at 700 °C(Figure 5.2 (b)). {311} defect formation is also a process of Ostwald ripening, in which dissociated simple I-F complexes diffuse quickly into the bulk. The extended I-type defects act as nuclei for F precipitates. Fast-diffusing I-F complexes can also be released during the formation of F precipitates to relax the stress, analogous to the formation of O precipitates [76].

Compared with the decrease of F concentration in the area where F precipitates are developed from I-type defects, the increase of F concentration around 0.95 μm after 125 h annealing (Figure 5.2 (b)) indicates the V-type defects attract F atoms much more effectively than I-type defects as nuclei of F precipitates. Vacancies can reduce the stress induced by the formation of F precipitates so that it is easier for them to grow from V-type defects. This also explains why, in addition to the initially higher F concentration, there is a much higher density of F precipitates in the band between 0.75 and 1 μm (Fig. 5-6).

Although vacancies can help relax stress during F precipitation, interstitials may still be emitted in this process. It is found in Figure 5.2 (b) that there is a loss of F (e.g., $\sim$ 20% after 4 h) in the V-rich region before 90 h at 700 °C. The increase of F concentration in the formation area of F precipitates cannot account for all the loss. We consider that a part of the lost F diffuses out of the surface in the form of simple I-F complexes, in which interstitials are emitted from F precipitates developed from V-type defects. Owing to the transient diffusion of simple I-F complexes, no change of F concentration is induced in the near-surface region.

The story of F diffusion in the V-rich region at 700 °C is clearly different from that described above. It is seen in Figure 5.2 (b) that, in addition to migrating to F precipitates at $\sim$ 0.95 μm, F diffuses from the high-concentration region near R_p towards the surface, consistent with the change of S shown in Figure 5.1 (b). As at 400 °C we obtain that E_m of F in the V-rich region is 2.19 eV assuming F at 0.9 μm takes 90 h to reach the surface; this falls into the range obtained before, leading to the conclusion that F also diffuses via a vacancy mechanism here.

The absence of defects seen by XTEM at < 0.75 μm means that the defects inducing the low S values in this region are V-F clusters whose sizes are below the threshold of XTEM visibility.

5.4 Conclusion

F retards V-I recombination in Si. F diffuses in the V-rich region via a vacancy mechanism. The loss of F in the I-rich region and a part of that in the V-rich region can be explained by the transient diffusion of simple I-F complexes. After a long annealing time at 700 °C F precipitates are developed from both V- and I-type defects. It is hoped that the basic insights gained here will contribute materially to the development of useful F-related structures.

Chapter 6

Characterization of the *nc*-Si/SiO_2 Interface region during the Agglomeration of *nc*-Si

6.1 Introduction

The study of nanocrystalline Si (*nc*-Si) is an active field of research because of applications in advanced electronic and optoelectronic devices. Several methods have been used to fabricate *nc*-Si, including embedding *nc*-Si in a SiO_2 matrix by ion implantation or by chemical vapor deposition, which is promising owing to its compatibility with present ultra-large scale integration (ULSI) technology. Visible luminescence from this system was first observed by Shimizu-Iwayama *et al*[94], and the recent achievement of optical gain in both waveguide and transmission configurations implied the possibility of the fabrication of Si lasers [95]. While it is generally accepted that the band gap of Si widens as a result of quantum confinement, which causes the blueshift of photoluminescence (PL) for Si crystallite size below 5 nm[96], it is also believed that the interface between *nc*-Si and SiO_2 plays a role in the radiative emission of *nc*-Si, especially when its size

is smaller than 3 nm[97]. Therefore, it is desirable to pay close attention to the interfaces associated with *nc*-Si.

Positron annihilation spectroscopy (PAS) with a slow positron beam has demonstrated its power in the investigation of the interface between SiO_2 and Si substrates[98, 3]. It is known that positrons can be easily trapped at open-volume defects as a result of the missing positive-ion cores at these defects. This trapping usually gives rise to a narrowing in the annihilation gamma energy spectrum, which is characterized by a higher S parameter compared with that for positron annihilation in defect-free sites. Here S is defined as the central fraction of the annihilation spectrum[4]. However, S is also sensitive to the impurities such as hydrogen[99, 100], oxygen[67, 50], fluorine[86, 101] and nitrogen[3]; when they decorate the open-volume defects in semiconductors, smaller S values may be observed instead. In this work PAS and PL are employed to study the interface between *nc*-Si and SiO_2. Changes of the interface region during the agglomeration of *nc*-Si in SiO_2 in different atmospheres are elucidated.

6.2 Experimental procedure

500 nm thick SiO_2 thermally grown in dry oxygen on a $\langle 100 \rangle$ Czochralski (CZ) Si substrate (p-type, $10\,\Omega \cdot$ cm) was implanted to a dose of $1.6 \times 10^{17} cm^{-2}$ with 150 keV Si^+. The implantation energy and dose were intentionally selected to produce a similar Si^+ distribution to that in [95]. The sample was then annealed at 1100 °C for 1 hour in nitrogen to produce *nc*-Si dispersed in SiO_2. The nanocrystals are $\sim$ 3 nm in diameter on average with a concentration of $2 \times 10^{19} cm^{-3}$ in a region centered at a depth of $\sim$ 200 nm from SiO_2 surface[95]. The PL spectrum of the as-formed nanocrystals has a peak at 800 nm, as in [95], demonstrating the similarity of the present nanocrystals to those in [95]. Further annealing of this sample was carried out between 400 and 900 °C for 30 minutes in nitrogen, oxygen and vacuum. In the former two a furnace with flowing gas was used. In the latter electron bombardment was employed at a pressure of $\sim 5 \times 10^{-6}$ Torr. PAS and PL were used to measure these annealed samples. Our PAS is based on a slow positron beam, whose maximum energy is 30 keV[102], corresponding

to a mean depth of 4 μm. PL measurements were made at room temperature using a photomultiplier detector; excitation was via the 514 nm line of an argon laser at a power $\sim$ 100 mW and a beam diameter $\sim$ 0.5 mm. The luminescence was measured with a Spex spectrometer with a slit width of 600 μm in the range 580 - 910 nm. Experimental conditions such as laser power and orientation with respect to the laser beam and spectrometer were kept constant as far as possible. A correction was necessary to account for the wavelength dependent response of the system. This was done by measuring spectra of a constant power tungsten lamp and comparing the measured spectra with its calculated spectra[103]. The apparent temperature of the tungsten lamp was measured using a pyrometer with a red filter.

6.3 Experimental results

6.3.1 Annealing in nitrogen

Figure 6.1 shows the change of the PL spectra from these nanocrystals after annealing at 700 and 900 °C in nitrogen, respectively. The PL spectrum of the sample after 400 °C annealing is essentially the same as that of as-formed sample, and so is not shown. After 700 °C annealing the position of the PL peak remains the same, but the short wavelength side becomes wider. A small redshift is observed after 900 °C annealing. It is assumed that the luminescence from the as-formed sample derives from both quantum confinement and interface state radiation because the sizes of nanocrystals are not uniform and their average size (3 nm) is on the boundary between the two mechanisms[97].

PAS results for the samples annealed in nitrogen are shown in Figure 6.2 (a). The S curves for the virgin SiO_2/Si and high temperature annealed (1100 °C, N_2) SiO_2/Si are also included for comparison. All the S values presented here have been normalized with respect to that for the defect-free Si bulk. The interface between SiO_2 and Si substrate is indicated by a dip at $\sim$ 7 keV in the S curve for the virgin SiO_2/Si, which corresponds to a mean depth of 386 nm. The dip

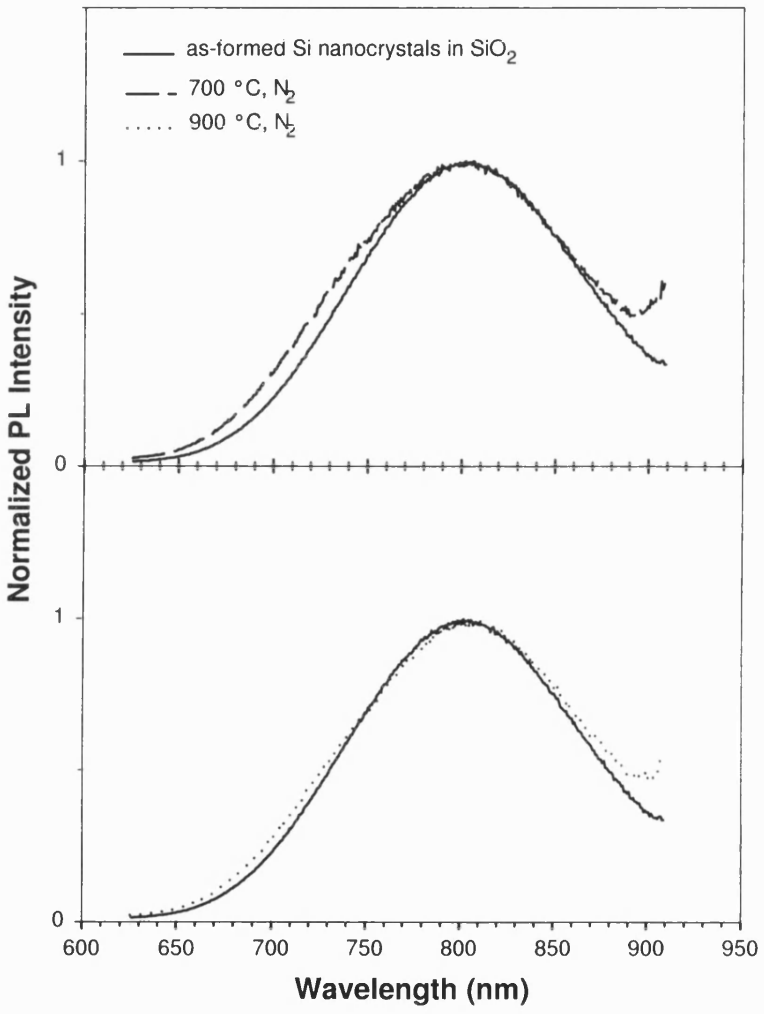

Figure 6.1: PL spectra of the as-formed sample and those annealed at 700 and 900 °C in nitrogen.

can be explained by the residual hydrogen at the interface region[104]. Here the apparent position of the interface is slightly shallower than 500 nm. This is possibly caused by the broad positron profiling shape[98]. It is seen that S values (from now on S values refer to those for the SiO_2 layer if not stated) for the as-formed sample are significantly smaller than those for the annealed virgin sample (1100 °C, N_2). After the sample is annealed at 400 °C, S values decrease, and then remain unchanged after annealing at 550 (not shown) and 700 °C. From 800 °C (not shown) S values begin to recover, becoming even larger than those for the as-formed sample after 900 °C annealing.

6.3.2 Annealing in oxygen

Figure 6.2 (b) shows the PAS results for the samples annealed in oxygen. As in nitrogen S values decrease after 400 °C annealing. With temperature they continue to fall until a minimum is met at 700 °C; then as in nitrogen, S values rise from 800 °C, and after annealing at 900 °C they become nearly the same as those for the as-formed sample.

After annealing in oxygen at 400 °C the PL spectrum shows no change, as in nitrogen. However, the clear PL redshifts for the samples annealed at 700 and 900 °C in oxygen are illustrated in Figure 6.3.

6.3.3 Annealing in vacuum

The PAS results for the samples annealed in vacuum are shown in Figure 6.4. After 400 °C annealing S values do not change in the SiO_2 layer. The S values for the region around SiO_2/substrate (500 nm of mean depth), however, are reduced significantly. When the temperature is increased to 500 °C, these values become slightly smaller than those for the as-formed sample, and the change in S for the SiO_2 layer is still negligible. The data for the annealing at 700 °C is similar to that for the as-formed sample and is not shown. The change in the SiO_2/substrate region during the present annealing is consistent with a model of interface defects

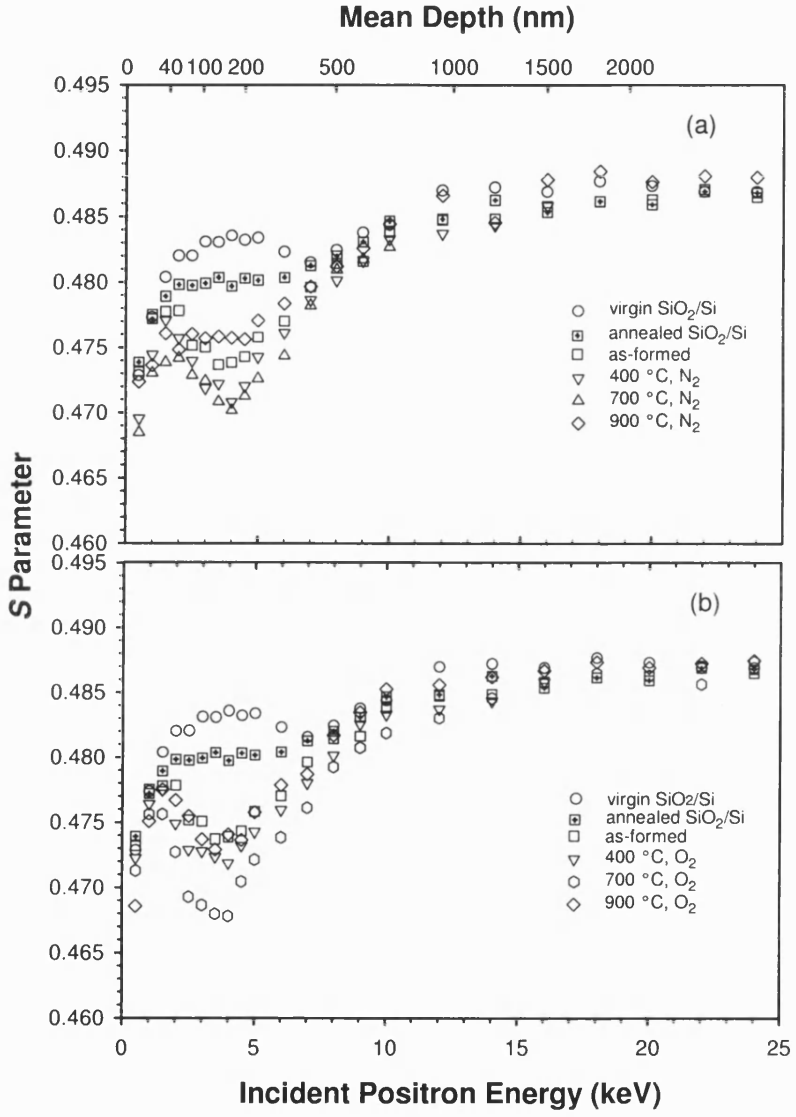

Figure 6.2: PAS results of the as-formed sample and those annealed in (a) nitrogen or (b) oxygen. The virgin and high temperature annealed SiO_2/Si samples are included for comparison.

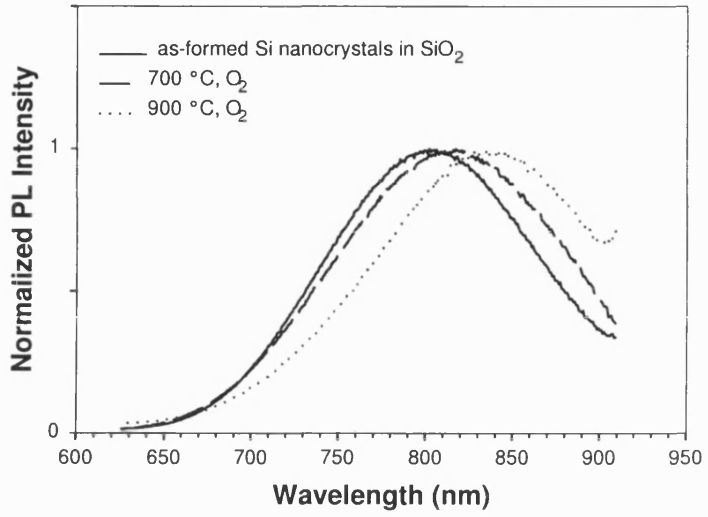

Figure 6.3: PL spectra of the as-formed sample and those annealed at 700 and 900 °C in oxygen.

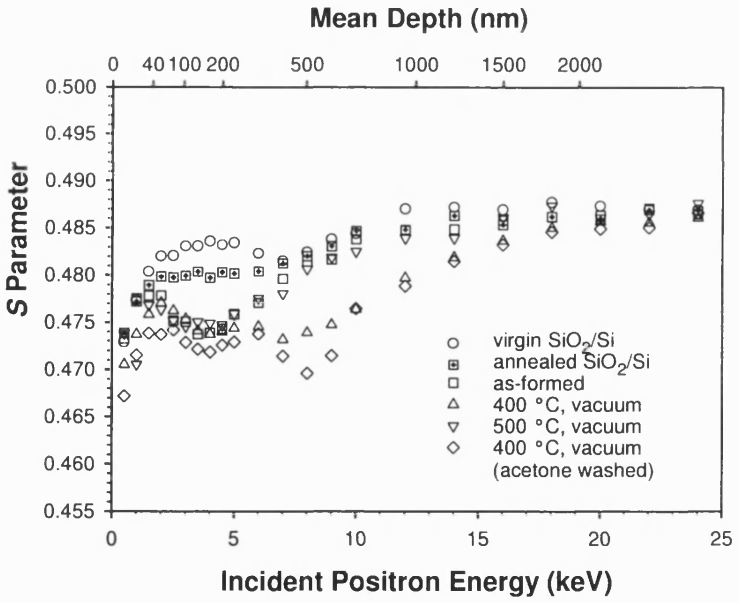

Figure 6.4: PAS results of the as-formed sample and those annealed in vacuum. The virgin and high temperature annealed SiO_2/Si samples are included for comparison.

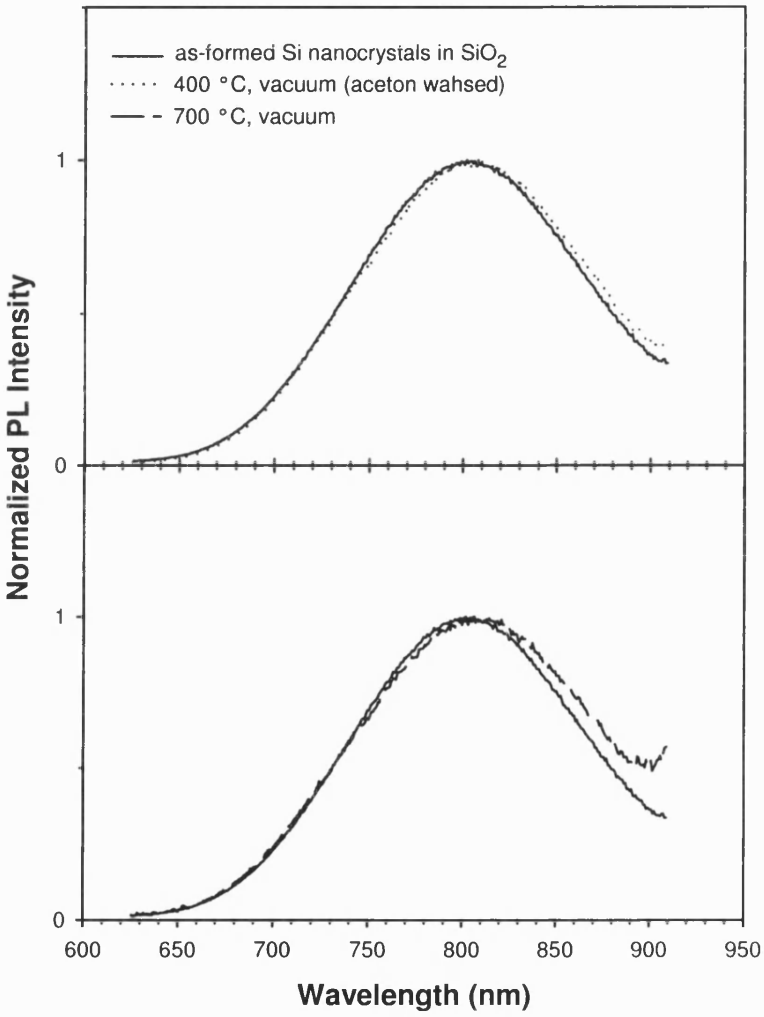

Figure 6.5: PL spectra of the as-formed sample and those annealed at 400 and 700 °C in vacuum. The sample annealed at 400 °C has been washed with acetone shortly before it was placed into vacuum.

(e.g. dangling bonds) passivation by hydrogen[100]. No change in the SiO_2 layer indicates that the hydrogen passivation of the defects at the *nc*-Si/SiO_2 interface is negligible. This implies that hydrogen mainly enters the normal SiO_2 structure during the high temperature formation process of *nc*-Si. In addition, we find that S values for both SiO_2 layer and SiO_2/substrate decrease if the sample is washed with acetone shortly before 400 °C annealing in vacuum.

No change in PL after 400 °C annealing in vacuum is observed. However, the additional acetone washing induces a small redshift of the PL peak, illustrated in Figure 6.5. Also shown is the clear redshift after 700 °C annealing in vacuum.

6.4 Discussion

According to Brauer *et al*'s work[105] it is certain that the annealing in this work does not change the structure of virgin SiO_2. As mentioned before, there is a high concentration of residual hydrogen in the SiO_2/Si interface region although the sample is grown in dry oxygen atmosphere[104]. During post-growth annealing hydrogen diffuses towards the surface of SiO_2 so that it is nearly uniformly distributed in the structure of SiO_2[104]. Because hydrogen introduces low S values in SiO_2[106, 48] we see a clear decrease in S after the virgin SiO_2/Si sample is annealed at 1100 °C in nitrogen (Figures 6.2 and 6.4).

When *nc*-Si is formed in SiO_2 after the same annealing, the S values are further reduced (Figures 6.2 and 6.4). This is not due to the implantation-induced defects, which can be annealed out at 600 °C[107]. Si nanocrystals themselves cannot account for this decrease, either. The diffusion length of positrons in defect-free Si is usually 215 - 250 nm[108], which is significantly larger than the sizes of *nc*-Si in our sample. Moreover, it is known that many interfaces are normally introduced between the SiO_2 matrix and *nc*-Si. The mismatch between them leaves open-volume spaces (voids) in the interface regions. They naturally have a better ability to trap positrons than both the normal SiO_2 structure and Si, inhibiting the quantum confinement of positrons in *nc*-Si no matter how different their positron affinities are[109]. Hence, the probability of positron annihilation

inside *nc*-Si is negligible[110]. Nitrogen also prefers to be trapped in these voids, leading to larger amount of nitrogen incorporated during annealing in nitrogen and, therefore, smaller S values are seen in PAS. The presence of nitrogen in a system of Si clusters embedded in SiO_2 has been identified by X-ray photoelectron spectroscopy (XPS)[111]. We should be also aware of the implantation-induced volume compaction in the structure of SiO_2. This leads to the suppression of the formation of positronium, also contributing to the decrease of S[107].

After 400 °C annealing in nitrogen, the trapping of nitrogen in the interface regions is saturated. This explains why S values decrease and then hardly change until 700 °C(Figure 6.2 (a)). As in nitrogen, 400 °C annealing in oxygen introduces oxygen into the voids around *nc*-Si. This causes the decrease of S (Figure 6.2 (b)), which continues until 700 °C. In contrast, 400 °C annealing in vacuum doesn't introduce any impurities. It appears that the defects at the *nc*-Si/SiO_2 interface have already been completely passivated by nitrogen from the atmosphere or/and oxygen from the implantation-induced oxygen interstitials during the formation of *nc*-Si. It is supposed that the voids around *nc*-Si don't trap hydrogen because of its small atom size and high mobility. They provide excellent diffusion channels for hydrogen instead. Therefore, hydrogen in the normal SiO_2 structure is not trapped in the *nc*-Si/SiO_2 interface regions during 400 °C annealing in vacuum. It diffuses to the SiO_2/substrate interface and is trapped by the interface defects there. The change of hydrogen concentration in the SiO_2 layer is small so that S values remain nearly the same as the as-formed sample (Figure 6.4). The concentration of hydrogen in the SiO_2/substrate interface, however, is considerably increased because its width (1 - 2 nm)[99] is much smaller than the thickness of the SiO_2 layer (500 nm). This explains the decrease of S around 7 keV (Figure 6.4). Nitrogen and oxygen suppress the diffusion of hydrogen in the SiO_2 layer probably by blocking its diffusion channels. This leads to the absence of the decrease of S around 7 keV after annealing in nitrogen or oxygen (Figure 6.2).

After washing the sample with acetone, the residual acetone may dissociate into H, O-H and C=O during the annealing at 400 °C in vacuum. It is supposed that H diffuse to the SiO_2/substrate interface, inducing a further decrease in S around 8 keV (Figure 6.4). O-H and C=O could enter the structure of SiO_2 or

the voids around *nc*-Si, giving rise to the decrease in S for the SiO_2 layer.

It is reasonable to assume that the trapping of oxygen in the voids increases with temperature. After the annealing at 700 °C in oxygen the PL peak is broadened (Figure 6.3). This indicates an inhomogeneous oxidation of *nc*-Si[112]. Oxidation means that additional oxygen is incorporated in addition to that in the voids. Hence, both the larger amount of oxygen in the voids and oxidation contribute to the decrease of S after 700 °C annealing (Figure 6.2 (b).

The average size of *nc*-Si actually increases after the annealing at 700 °C in oxygen because the PL peak is redshifted (Figure 6.3). The agglomeration of nanocrystals and the volume increase induced by the oxidation of nanocrystals both make smaller interface regions, and thus smaller void volume. This weakens the trapping of oxygen. However, its effect on the positron measurement is not enough to counter the above two factors.

Agglomeration during the annealing at 700 °C in nitrogen is negligible because there is negligible shift of the PL peak (Figure 6.1). The widening of the short wavelength side of the PL peak, however, indicates more small nanocrystals are produced. The average distance between nanocrystals in the as-formed sample is estimated to be $\sim$ 0.68 nm. Assuming an activation energy of 1.9 eV and a pre-exponential factor of 1.29×10^{19} cm^2/s for the diffusion of Si in SiO_2 in nitrogen atmosphere[113], we find that a Si atom only travels $\sim$ 0.18 nm at 700 °C in 30 minutes. It is supposed that via the Ostwald ripening mechanism[88] Si atoms dissociated from small nanocrystals do not move far enough to reach larger ones after 700 °C annealing in nitrogen. This causes a decrease in the size of small nanocrystals without any growth of the neighboring ones. Apparently, the increase of the void volume induced by this process is not significant enough to enhance the trapping of nitrogen and thus reduce S values. The difference in the agglomeration between nitrogen and oxygen atmosphere implies that the diffusion of Si in SiO_2 is slower in nitrogen atmosphere.

Now we turn to the PL results for the annealing in vacuum. It is interesting that a small redshift of the PL peak appears even at 400 °C after washing with acetone (Figure 6.5), in contrast to the annealing in nitrogen, oxygen and vac-

uum. The unique element introduced by acetone is carbon compared with the others. Hence, we believe that carbon may enhance Si diffusion in SiO_2, resulting the agglomeration of *nc*-Si at low temperature. The redshift of the PL peak after 700 °C annealing in vacuum is clearly larger than in nitrogen (Figures 6.5 and 6.1), again, implying the slow Si diffusion in SiO_2 in nitrogen atmosphere. The underlying mechanism for these different diffusion phenomena needs further study.

Above 700 °C in nitrogen, Si atoms can move farther so that the agglomeration of *nc*-Si takes place. This is evidenced by the small redshift of the PL peak after the annealing at 900 °C in nitrogen (Figure 6.1). As in oxygen, the broadening of the PL peak may be due to a nitridation process of *nc*-Si at high temperature. Both the size increase and nitridation reduce the interface regions and thus the volume of voids. Assuming that the trapping rate of nitrogen in voids is nearly the same as at low temperatures, the resultant decrease in the amount of nitrogen gives rise to the recovery of S. The reduction of positron trapping in the interface regions is compensated by the increase in the intrinsic open-volume of SiO_2 matrix. The latter is characterized by high S values because of the probable formation of positronium[114]. After 900 °C annealing in nitrogen the fraction of positrons annihilated in the SiO_2 matrix becomes high enough to increase measured S values to above those for the as-formed sample (Figure 6.2 (a)).

On annealing at high temperature in oxygen, the enhanced Si diffusion in SiO_2 results in more effective agglomeration of *nc*-Si. This is illustrated by the considerable redshift of PL peak after 900 °C annealing in oxygen (Figure 6.3). The more significant size increase, together with the oxidation process, introduces a larger shrinkage of the interface regions and the volume of associated voids than on annealing in nitrogen. The resultant decrease of positron trapping in the interface regions should have led to a larger recovery of S; however, S values just recover to the level for the as-formed sample after 900 °C annealing in oxygen (Figure 6.2 (b)), clearly lower than those for the sample annealed at the same temperature in nitrogen.

During oxidation the oxidized Si can introduce a volume increase by up to

100 %, which is $\sim$ 4 times larger than that during nitridation. We believe that the volume increase of *nc*-Si (including their oxide shells) during the oxidation at 900 °C is so large that the intrinsic open-volume of SiO_2 matrix shrinks to relax the stress induced by it . This shrinkage suppresses the formation of positronium in spite of the increase of the fraction of positrons annihilated in SiO_2 as happens in the annealing at 900 °C in nitrogen, and, the increase in S is weakened.

6.5 Conclusion

We find that nitrogen and oxygen are trapped in the voids around *nc*-Si at low temperatures. It appears that the defects at the *nc*-Si/SiO_2 interface have already been completely passivated by nitrogen and/or oxygen in the as-formed *nc*-Si sample. High temperature annealing during the formation of *nc*-Si causes hydrogen to enter the SiO_2 structure, which originally exists in the SiO_2/substrate region. It diffuses back to the SiO_2/substrate region in vacuum at 400 °C because no other impurities block its diffusion channels. At temperatures above 700 °C, both nitrogen and oxygen react with *nc*-Si, resulting in a volume increase. This introduces stress in the SiO_2 matrix, which is relaxed by the shrinkage of its intrinsic open volume. Moreover, it is proposed that nitrogen suppresses Si diffusion in SiO_2, so that the agglomeration of *nc*-Si is slower during the annealing in nitrogen than that in oxygen or vacuum.

Chapter 7

Defects in GaN Films

7.1 Introduction

GaN is a very promising semiconductor material for optoelectronic and high-temperature electronic device applications. It is imperative that the nature of defects in GaN and related materials, and the mechanisms for their formation and evolution, should be understood clearly so that the full potential of GaN and its alloys can be completely realised in device structures[115, 116, 117].

Positron annihilation spectroscopy (PAS) with a slow positron beam is an efficient tool for the investigation of open-volume defects such as vacancies in semiconductors[4]. The implanted monoenergetic positrons can readily become trapped at open-volume defects as a result of the missing positive ion core at these defects. The trapping gives rise to a narrowing of the momentum distribution of the positron-electron pair and thus also in the annihilation gamma energy spectrum. The latter is characterised by a higher S parameter (or lower W parameter) compared with the positron annihilation in defect-free lattice sites[4]. Here S (W) is defined as the ratio of the central (wing) area to the total area under the spectrum. The most probable point defects in GaN are believed to be N vacancies (V_N) in p-type GaN and Ga vacancies (V_{Ga}) in n-type GaN[118]. Whereas positively charged V_N do not readily trap positrons, V_{Ga} can be observed

by PAS because they are usually negatively charged[119, 120, 121].

Open-volume defects are deep positron traps. However, shallow positron traps, such as negative ions and dislocations, also exist in semiconductors[122, 71]. Previous slow positron studies of GaN films demonstrated that the effect of shallow traps could be clearly seen up to 500 K[119]. In this letter we investigate the defect structure of GaN films grown by metal organic chemical vapour deposition (MOCVD) by studying the annealing behaviour from 150 to 900 °C.

7.2 Experimental procedure

The GaN samples were grown on (0001) oriented sapphire by MOCVD at the University of Bath. The growth pressure was 200 mbar. Trimethyl gallium (TMG) and NH_3 were employed as precursors and H_2 as gas carrier. A $\sim$ 20 nm thick nucleation layer was initially deposited on the substrate at low temperature. 400 nm undoped GaN was then grown, followed by 2 μm Si-doped n-type GaN at high temperature. The carrier density and Hall mobility of the as-grown sample were 2.2×10^{17} cm^{-3} and 390 $cm^2V^{-1}s^{-1}$, respectively. The samples were annealed for 2 minutes at temperatures in the range from 150 to 900 °C with an electron beam heater in a vacuum of $\sim 5 \times 10^{-6}$ Pa. Slow positron measurements were carried out at room temperature for the as-grown sample and after every annealing step. In addition, a 3 μm thick lightly Mg-doped high-resistivity GaN film grown by MOCVD on a sapphire substrate was measured as a comparison.

Single-detector Doppler-broadening spectroscopy was performed using a magnetic-transport positron beam system[102].

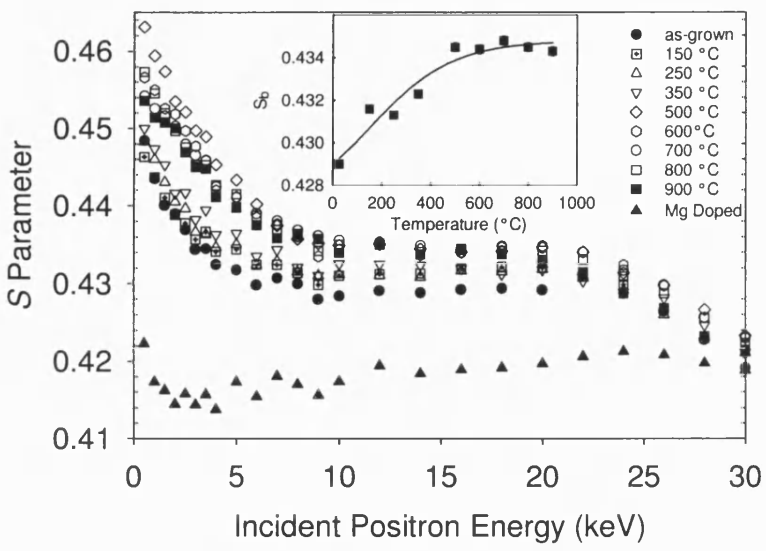

Figure 7.1: S parameter vs. incident positron energy for as-grown and annealed samples. A lightly Mg-doped sample is used as a comparison. The change of S_b with annealing temperature is shown in the inset, where the solid line is a sigmoidal fit.

7.3 Results and discussion

Figure 7.1 shows the results of the slow positron measurements. The incident positron energy E (keV) corresponds to a mean probed depth of $\sim 6.7E^{1.6}$ nm. The measured S can be expressed as a combination of different characteristic S values at different positron annihilation sites. If we use S_s, S_b, S_i and S_{sub} to denote S for positrons annihilated at the surface, in bulk GaN, in the interface region between GaN and sapphire and in the sapphire substrate, respectively, then the measured S is:

$$S = f_s S_s + f_b S_b + f_i S_i + f_{sub} S_{sub} \tag{7.1}$$

where f_s, f_b, f_i and f_{sub} are the corresponding fractions of implanted positrons annihilated at the different sites at each E, respectively. At the lowest incident positron energy, 0.5 keV, it is assumed that essentially all the positrons are annihilated at surface, and we therefore take the measured S at 0.5 keV as S_s in

this study. When E is increased to a value in the range from $\sim$ 10 to $\sim$ 18 keV, almost all the positrons are annihilated in bulk GaN. By implanting positrons from the sapphire side S_{sub} is obtained. S_i cannot be obtained directly from the measurements. It is found that a good fit to the data cannot be achieved by the code VEPFIT[57] without incorporating a very low S ($\sim$ 0.330) in the first $\sim$ 300 nm region above the sapphire.

It has been demonstrated that the defects seen by positrons in GaN are V_{Ga}[119, 120, 121]. There are fewer V_{Ga} in Mg-doped GaN than in n-type GaN[120, 121]. The existence of V_{Ga} can be confirmed if the measured S values are larger than those of Mg-doped GaN, which is the case here (Figure 7.1).

It is interesting to note that S increases slightly as E increases from 9 to 20 keV for the as-grown sample. The increase is believed to be real because the error bars are smaller than the size of the data points in Figure 7.1. This suggests that the V_{Ga} concentration increases with depth. It should be noted that there are still some V_{Ga} in the lightly Mg-doped sample because the formation energy of V_{Ga}, which is the function of Fermi level, is not high enough to block completely the formation of V_{Ga}[121]. Hence, the increase of V_{Ga} with depth can also be seen in our lightly Mg-doped GaN. In GaN dislocations originate from the faulted regions located within the nucleation layer[123]. The dislocation density is very high within the first $\sim$ 400 nm from the substrate, and with the further growth of GaN it decreases towards the surface[124]. Therefore, the change of V_{Ga} concentration is apparently correlated with that of dislocation density. A scanning capacitance microscopy study has indicated that there are negative charges near the dislocations[125], and these can result from V_{Ga}. In summary, V_{Ga} appear to prefer to reside alongside dislocations.

After annealing S_b increases until it becomes nearly constant at temperatures higher than 500 °C. The inset in Figure 7.1 shows this change, where S_b is taken as the average of the S values measured in the positron energy range from 9 to 20 keV for the as-grown sample and those annealed below 500 °C, and the values on the flat part of the curve for the samples annealed at $\geq$ 500 °C. It is well known that by plotting S versus W one can determine whether or not a defect type remains unchanged under external influence[4]. It is clear from Figure 7.2 that

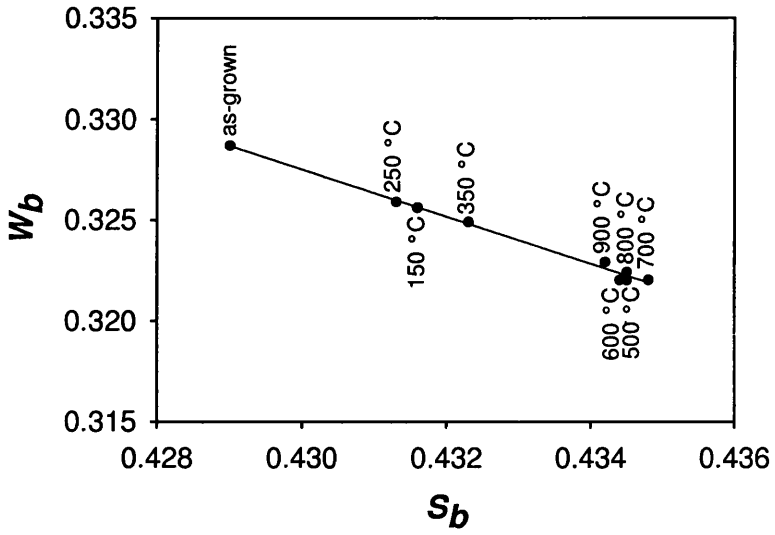

Figure 7.2: W_b vs. S_b for the as-grown sample and annealed GaN from 150 to 900 °C. All the data fall on the same line, suggesting that the defects seen by positrons are V_{Ga} in all the samples

all the data fall on the same line, suggesting that the defects seen by positrons are V_{Ga} in all the annealed samples.

It is tempting to attribute the increase of S_b with annealing temperature to an increase in vacancy concentration. However, because the trapping rate of positrons is proportional to vacancy concentration, the effective positron diffusion length, L_{+eff}, will decrease when the vacancy concentration increases[4]. By using

$$f_s(E) = \int_0^\infty P(z)exp(-z/L_{+eff})dz \tag{7.2}$$

where $P\ (z)$ is the normalized positron implantation profile along the depth, z, at a positron implantation energy E, L_{+eff} can be obtained by measuring f_s. Although the defect distribution is not uniform in the GaN film, as discussed before, the variation with depth of the PAS response is small. This is clear by looking, between $\sim$ 10 and $\sim$ 20 keV, at the small slopes for the as-grown sample and those annealed below 500 °C, and the nearly constant S for those annealed above 500 °C (Figure 7.1). Therefore, it is assumed that such a defect distribution is sufficiently homogeneous over the positron diffusion length in GaN to validate

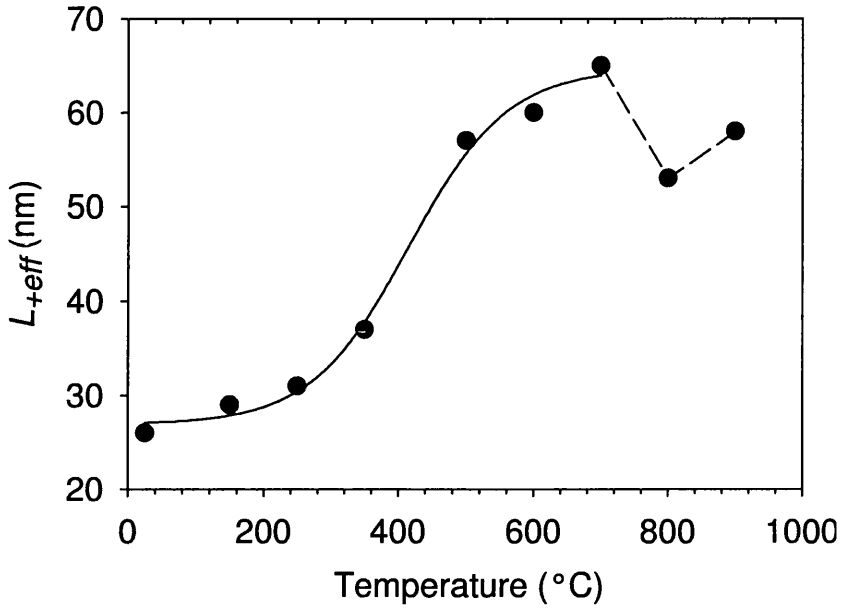

Figure 7.3: The change of effective positron diffusion length in as-grown and annealed GaN. The solid line is a sigmoidal fit. The dashed line is used to guide the eye.

the use of equation (7.2) in our analysis. For each E lower than $\sim$ 10 keV f_s can be calculated using eq. (1) with $f_i = 0$, $f_{sub} = 0$, and the S_b values illustrated in the inset of Figure 7.1 (the real S_b for the regions probed by positrons of energies lower than $\sim$ 10 keV may be slightly, but unimportantly, different). Figure 7.3 shows L_{+eff} from the as-grown and annealed data by fitting f_s versus E with equation (7.2). It is evident that L_{+eff} increases from $\sim$ 30 to $\sim$ 60 nm after the annealing at and above 700 °C. Hence, the increase of S_b cannot be considered to be due to an increase of vacancy concentration.

The present results are therefore interpreted as follows. A fraction of the positrons detrapping from shallow traps can travel further, leading to the increase of L_{+eff}, and others can be trapped by V_{Ga}, leading to the increase of S. Given that shallow positron traps in GaN films have been seen up to 500 K[119], it is naturally believed that they play an important role in the present measurements at 300 K. It has been demonstrated that negative ions trap positrons only efficiently at temperatures below 200 K[126]. Therefore, although Saarinen *et*

al surmised that negative ions acted as shallow traps at temperatures up to 500 K[119], we consider that dislocations are actually the main shallow traps in the present measurements; they have been observed to act as shallow traps in other semiconductor materials[71]. There is expected to be a high density of inherent dislocations in GaN.

As mentioned above, the total dislocation density decreases from the interface to the surface in GaN. In the region near the interface, most of the dislocations are not directed towards the surface along (0001), in contrast to those in the shallower region[127]. The higher density and randomness enable easier dislocation interaction in the deeper region, and thus the annealing of dislocations in the deeper region is efficient, even at temperatures $\leq$ 350 °C, which leads to the obvious increase in S_b (inset, Figure 7.1). However, the increase in L_{+eff}, which characterise the shallower region (E lower than $\sim$ 10 keV), is very small (Figure 7.3), resulting from the insignificant annealing of dislocations in the shallower region. When the temperature is increased to 500 °C, the annealing of dislocations becomes significant even in the shallower region. Therefore, an obvious increase in L_{+eff} is observed (Figure 7.3). Meanwhile, positron trapping in V_{Ga} becomes nearly saturated so that the change in S_b is small (inset, Figure 7.1).

It can been that S_b is approximately constant between 500 and 900 °C (inset, Figure 7.1). This is contrast to the change of L_{+eff} (Figure 7.3). The latter observation indicates that the dislocation density continues decreasing in this temperature range, consistent with XTEM measurements of the annealing of GaN between 600 and 800 °C[128]. After the samples are annealed above 500 °C the associated increase in the number of positrons which can be trapped by V_{Ga} does not increase S_b. This implies that the trapping at V_{Ga} has been saturated.

We also notice that when the sample is annealed at $>$ 700 °C, L_{+eff} decreases (Figure 7.3). It is supposed that there are many V_N produced at the surface at 800 °C because this temperature is very near the dissociation temperature, 850 °C, of GaN in the vacuum[129]. These V_N can make the GaN more n type owing to their donor nature. This results in a band bending near surface, forming a potential that retards positron back-diffusion to the surface and the apparent

decrease in L_{+eff}. Above 800 °C changes are attributed to the dissociation of GaN.

Comparing the S curve of 900 °C to those measured for lower temperatures, the energy denoting the interface between GaN and sapphire drops from 22 to 18 keV (Figure 7.1). Using the code VEPFIT the depth of the interface between GaN and sapphire is found to be at $\sim$ 1800 nm after the annealing at 900 °C. This corresponds to a dissociation rate of $\sim$ 5 nm/s, which is somewhat larger than the value of 1.2 nm/s obtained by extrapolating Grandjean *et al*'s data[130]. This difference is probably due to the fact that in our system, which does not employ a rapid thermal process, efficient dissociation has happened before 900 °C.

Finally, we return to the very low S in the interface region, as derived from the fitting program. Such a low S can be explained by the presence of many oxygen clusters in that region. During the growth of GaN at high temperature oxygen can diffuse from sapphire to the interface region, as has been indicated by SIMS measurements[131]. These oxygen atoms can easily form clusters because there are many defects such as voids that can act as the nucleation centers in the interface region. Oxygen clusters reduce S to a value smaller than that for defect-free semiconductors[50]. Moreover, the present results suggest that these oxygen clusters are stable up to 900 °C because the low S exists in all the samples. It should also be noted that an electrical field probably exists near the interface, which can enhance positron diffusion to oxygen clusters or to sapphire and result in a smaller S.

7.4 Conclusion

The results presented in this letter suggest that V_{Ga} exist alongside dislocations in GaN films and are stable up to 900 °C. Dislocations are believed to behave as shallow positron traps. The decrease of dislocation density increases the positron L_{+eff} and S parameter for annealing at $\leq$ 500 °C. Above 500 °C, the trapping of positrons at V_{Ga} is saturated and S becomes constant, while L_{+eff} continues

to change. The near-surface formation of V_N at high temperature can introduce a potential that retards positron back-diffusion. The dissociation rate of GaN at 900 °C is estimated to be $\sim$ 5 nm/s. In addition, the results are consistent with the presence of oxygen clusters in the $\sim$ 300 nm region near the interface, which are stable up to 900 °C

Chapter 8

Realization of a Compact Positron Beam Spectrometer

8.1 Introduction

The motivation for this work is to harness the potential of Positron Annihilation Spectroscopy (PAS) in a user-friendly instrument for general use in an industrial environment. The desirable features of PAS are its non-destructive nature, its high sensitivity to vacancy-type defects (e.g., to divacancy concentrations in Si as low as $\sim 10^{15}$ cm^{-3}), its depth tuneability - it is especially useful for measurements within 10^1 - 10^3 nm of the surface - and its potential for large-area mapping. It does not require a post-implant annealing step or post-processing preparation prior to measurement, and it does not significantly power-load the substrate.

The physics of the formation and evolution of defect structures in epilayer and implanted semiconductors has been studied in university-based positron laboratory facilities for more than a decade[4]; however, in order to meet the criteria for acceptable use as an instrument of practical use in industry a compact, user-friendly system is required. The past two years has seen the parallel development of such a positron instrument and an extensive program of PAS measurements on implanted and as-grown semiconductor samples performed on a traditional

laboratory-based positron beam system. These measurements were designed both to evaluate the prospects for using the instrument as an ion dosimeter with mapping capability, and to investigate the broader potential exploitation of PAS in near-market research and development laboratories.

The form of beam-based PAS most widely used in the study of the microstructure of implanted semiconductors and thin films measures the Doppler broadening of annihilation radiation, and it is this spectroscopy that we have chosen as the basis for the instrument. It is relatively straightforward and has the potential to produce measurements in the short times demanded by industrial laboratories. Typical research-laboratory-based positron beams designed for Doppler broadening measurements are a few meters in length, allowing effective radiation shielding between radioactive source and gamma detector. The footprint of any instrument based on such a system has to be $\sim$ 1 m^2 or less, and this presents a significant design challenge.

The focus of our diagnostic research has been the application of beam-based PAS to ion-implanted silicon. In the case of as-grown thin films, the effective positron diffusion length is considerably smaller than those of defect-free metals ($\sim$ 100 nm) and semiconductors ($\sim$ 250 nm), so that positrons implanted at low enough energies do not appreciably diffuse from films as thin as 10 nm, and are annihilated within them[132]; the raw PAS data can thus often demonstrate directly a response characteristic of the film. For very thin films, and for those in which there may be significant positron out-diffusion, well-established analysis codes can be applied to fit the raw data and extract information on film response[57].

8.2 Design and construction of the instrument

8.2.1 Performance and design requirements

The primary requirements are that a PAS instrument, which incorporates features of research apparatus developed in the research laboratory in recent years, should be compact, that measurements should be rapid and safe, and that the operator interface be user-friendly.

The footprint of the prototype is ~ 1 m^2, made possible by compact, robust design and the employment of electrostatic beam transport and focusing including a 90° reflector to enable efficient radiation shielding between positron source and gamma detector.

Efficient production, delivery and detection of slow positrons leading to high data collection rates are coupled with a rapid sample changing capability. Safe radioactive source handling is achieved via a rapid positron source installation technique, and the safety aspects of high voltage supply and vacuum system operation are addressed.

Sample loading is via a small airlock system, and wafer transport and positioning, as well as data collection and analysis, is performed by the operator via a PC interface screen.

8.2.2 Construction of the instrument

A schematic diagram of the vacuum chamber is shown in Figure 8.1, and a photograph of the entire system (without lead shielding) in Figure 8.2. The system is evacuated to $\sim 10^{-5}$ Pa by an (oil-free) turbomolecular pump with magnetically-levitated bearings, backed by a dry mechanical pump. The radioactive primary positron source is a ~ 1.2 GBq ^{22}Na sealed capsule, inserted into the system on a meter-long manipulator through a small hole in the lead shielding which is then

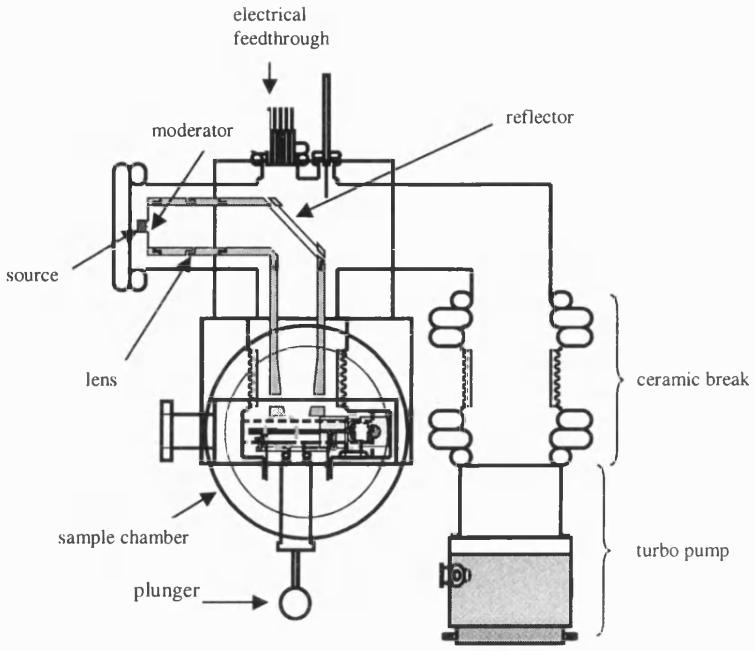

Figure 8.1: Schematic diagram of the spectrometer vacuum system.

plugged. The moderator comprises seven overlaid annealed tungsten meshes, which thermalise the beta positrons and re-emit $\sim 10^{-4}$ of them with eV energies. The open area is less than a few percentage so that the penetration of beta positrons is minimised and background radiation from their annihilation in sight of the detector is minimised. The potentials to the electrostatic lenses, including the 90° reflector, are realized by two 30 kV power supplies. While the positron implantation energy (and hence probed depth) is defined by the potential applied to the entire upper portion of the system, the relative potentials on the lenses are always the same, ensuring approximately constant beam characteristics at all energies between 0.1 and 30 keV. Initial settings of lens potentials were those predicted by ion-transport computer modelling. This method permits the use of standard electrical feedthroughs.

The annihilation gamma photons are detected through a thin window by a high-resolution Ge detector positioned directly beneath the sample. The detector is shielded from the primary source by lead of minimum thickness 0.2 m. Lead shielding of ~ 0.15 m thickness is mounted around the entire system to ensure safe

shielding. The high-voltage part of the system is insulated by vacuum ceramic breaks and by a complete coating of ~15 mm insulating material.

The sample wafer, currently 4-inch-diameter, is loaded via a door-mounted plunger into a letterbox-style airlock system, whose volume has been minimised to reduce the time required for pumpdown. It is taken automatically (under computer control) to any desired position under the positron beam and over the Ge detector by a transport system.

Sample manipulation and data collection is computer-controlled by the operator, with simple on-screen guidance. The positron energy is tuneable in the range 0.1 - 30 keV (mean depth from the surface to $\sim$ 4 μm in Si) and direct reading of relevant parameters (e.g., the lineshape parameter S) is given after data collection and analysis. Pulse height analysis is performed by the EG & G DSPEC2 digital processor to achieve high throughput with acceptable gamma energy resolution.

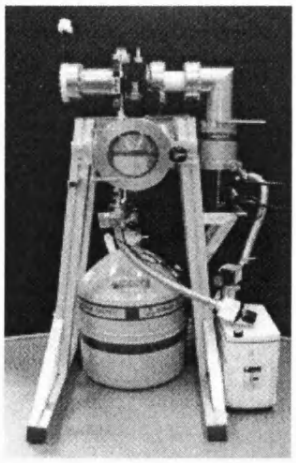

Figure 8.2: The prototype positron instrument without lead shielding.

8.3 Diagnostic measurements

The first measurements to be taken with the new instrument are shown in Figures. 8.3. In Figure 8.3 a Si wafer with a 5-mm-wide strip of silver paint

has been moved in small steps under a 5 keV positron beam and the lineshape parameter S measured. A fit to the resulting data yield a value for beam diameter of 1.8 ± 0.2 mm. The lead has proved to be essentially 100% effective in shielding source from detector. The signal count rate was $\sim 4500\ s^{-1}$ and the time per point $\sim 10^2$ s.

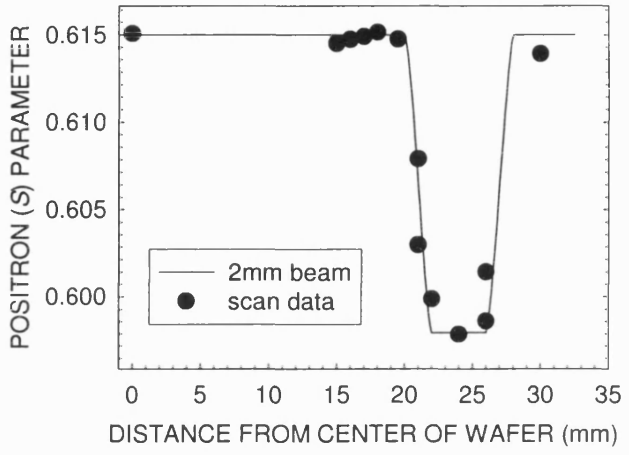

Figure 8.3: Positron response as a Si wafer with a 5 mm wide silver strip is scanned across the beam.

8.4 Further developments

Current work on the system is aimed at improving its performance by decreasing deadtime, developing an efficient positron moderator which is completely opaque to fast (beta) positrons, and improving system stability. Future developments will include increasing the speed of the wafer transport system: introducing a electrical cooling system for the Ge detector: and further automation including interlocks on high voltage and vacuum lines. Scaling of the prototype to handle wafers of any size is possible.

8.5 Applications

8.5.1 Monitoring ion dose and uniformity

The primary motivation for the development of the bench-top tool was the requirement for metrology techniques capable of providing information on the dose and uniformity of ultra-low energy implants. We have previously described the ability of PAS to monitor dose variations as a function of wafer area and depth resulting from sub-keV ion implantation[133]. More recently, we have described the response of PAS to MeV ion implantation[89]. The study analyzed response to ions varying in mass and energy from protons at 450 keV, to Ge^+ at 4 MeV. The results led to the deduction of a relationship between ion dose (normalized using TRIM[22]), (Φ_A), and vacancy-type defect concentration, (C), at 1/2 R_p such that

$$C = 2.79 \times 10^{10} \Phi_A^{0.63} \tag{8.1}$$

for all ions in the energy and dose range used in the study. In addition to being a straightforward and reliable expression for estimating aggregated vacancy-type defect concentrations following MeV implantation, (8.1) implies the ability to determine implanted dose for a wide range of implantation conditions using only the raw PAS data and TRIM output.

In summary, PAS may be used with varying sensitivity to monitor implant dose from 1×10^{10} - 1×10^{16} cm^{-2} and implant energy from sub-keV to MeV. In many cases, the raw PAS data can be used to provide an absolute measure of dose within an accuracy of $< 10\%$.

The ability to probe depth-dependent defect distributions with a focused positron beam of $\sim$ 2 mm diameter also offers the opportunity to measure non-uniformities in the concentration of open-volume defects across a wafer. Such non-uniformities can be caused by many different phenomena, depending on the sample and the process undertaken. Figure 8.4 shows an example of a 4-inch float

zone Si wafer exposed to a nominal dose of 3×10^{15} cm^{-2} of 120 keV O^+ ions. The measurements, which were taken using the new beam at the positron energy of 3 keV, illustrate the potential of a high-intensity mm-resolution scanning instrument.

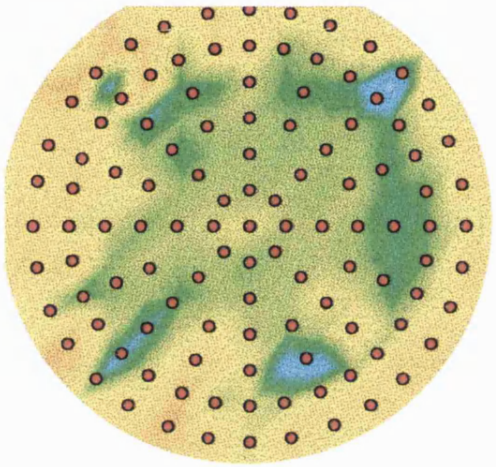

Figure 8.4: Implantation uniformity of a 4-inch float zone Si wafer nominally exposed to a dose of 3×10^{15} cm^{-2} of 120 keV O^+ ions measured by the compact positron beam spectrometer at the positron energy of 3 keV. The mapping positions are indicated by red dots. Different colours indicate different S parameters and thus different implantation parameters.

8.5.2 SIMOX process control

Separation by implantation of oxygen (SIMOX) is a well-established technique for producing silicon-on-insulator (SOI) structures. Ion energies of 100 - 200 keV at doses approaching 1×10^{18} cm^{-2} are typical in the fabrication of conventional SIMOX, however much of the current research is aimed at developing low-dose fabrication processes where the implanted dose is at least one order of magnitude lower, with significant reduction in fabrication time and cost. Spectroscopic ellipsometry (SE) has been used successfully to monitor implanted O dose via the measurement of the thickness of the Si rich, back interface layer of the buried oxide (BOX)[134]. A significant disadvantage to the use of SE is the requirement

for the measured sample to be a fully formed SIMOX wafer having undergone not only oxygen implantation but also a high temperature anneal for several hours.

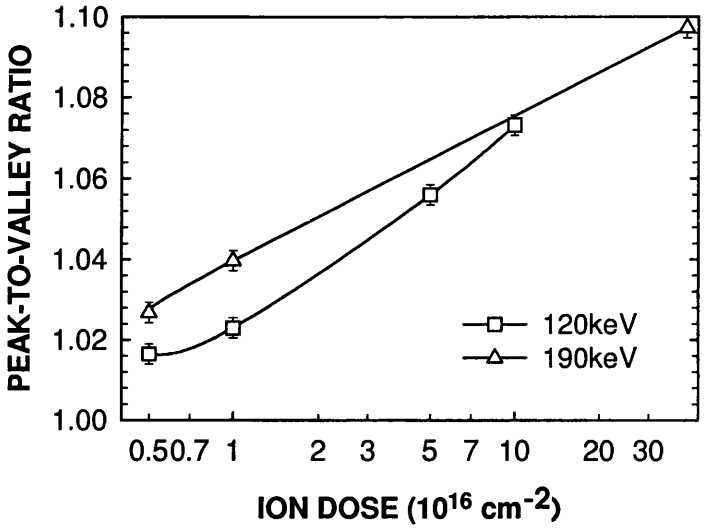

Figure 8.5: PAS peak-to-valley parameter vs ion dose for 120 and 190keV O^+-implanted Si (as-implanted).

PAS is known to be highly sensitive to the structure of silicon following high dose oxygen implantation[5]. The S parameter versus energy curve typically has a peak (corresponding to voids generated near the Si surface) followed by a valley (resulting from positron interaction with defects complexed with the end of range oxygen). For each dose of oxygen at a particular implantation energy, the ratio of the peak to valley S parameter value is unique. Figure 8.5 shows values of peak to valley ratios versus implanted dose for implant energies of 120 and 190 keV. The sensitivity of measurement varies with dose, but significantly, at the lower dose values (i.e. those appropriate to low-dose SIMOX formation) the peak to valley ratio is sensitive to changes in dose of $\sim$ 5%. PAS is therefore an ideal technique for process control of low-dose (and standard-dose) SIMOX formation, with a sensitivity to changes in dose of a few per cent measured on as-implanted wafers as opposed to those which consist of fully formed SOI.

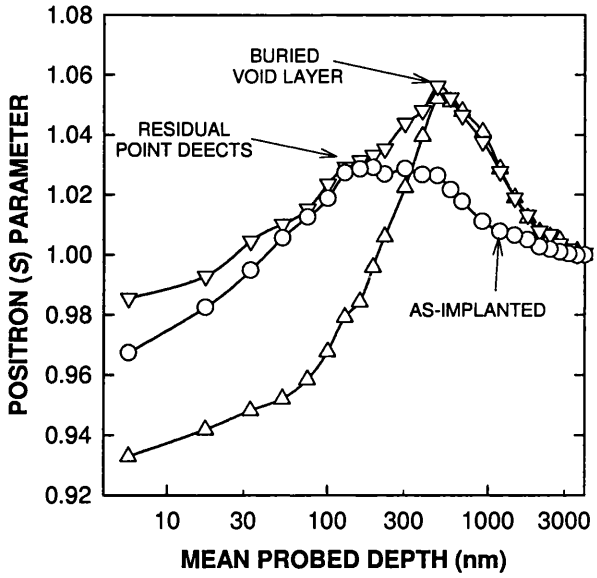

Figure 8.6: Raw PAS data for 100 keV He^+-implanted Si at 5×10^{16} cm^{-2}. The circles represent data for the as-implanted sample. The up-triangles are data taken from the same sample following a thermal annealing step. The down triangles are data taken from a sample with a small difference in processing history.

8.5.3 Monitoring of void formation

It has been known for sometime that nanocavities can be formed by high-fluence implantation of H or He[12]. Post-implantation annealing causes the implanted species to outgas leaving behind microscopic voids. This process has found use as an efficient method for forming gettering centers in Si. The implantation of H in particular is also an important step in the UNIBOND process[135]. PAS is a particularly appropriate technique for monitoring the formation and evolution of vacancy clusters into small nanocavities. Figure 8.6 shows S parameter values versus mean probed depth for He^+-implanted Si (100 keV, 5×10^{16} cm^{-2}), both pre- and post-thermal processing. The circles represent data for the as-implanted sample. Here the S parameter value of only 1.03 indicates the presence of small vacancy-type defects. The up-triangles are data taken from the same sample following a thermal annealing step. The increase of the S parameter to $\sim$ 1.06 indicates the formation of a layer of small voids at a depth of 500 - 600 nm, consistent with the depth of peak disorder. The remaining data (down triangles)

were taken from a sample with a small difference in processing history. The PAS data here indicates the presence of both point defects from the original implant and a layer of voids positioned at the end-of -range.

8.5.4 Response to chemical composition of thin films

As PAS is sensitive to changes in the local electronic environment, there exists in principle a unique S parameter value for each element of the periodic table. PAS can thus provide non-destructive information on the structure and stoichiometry of thin films[136].

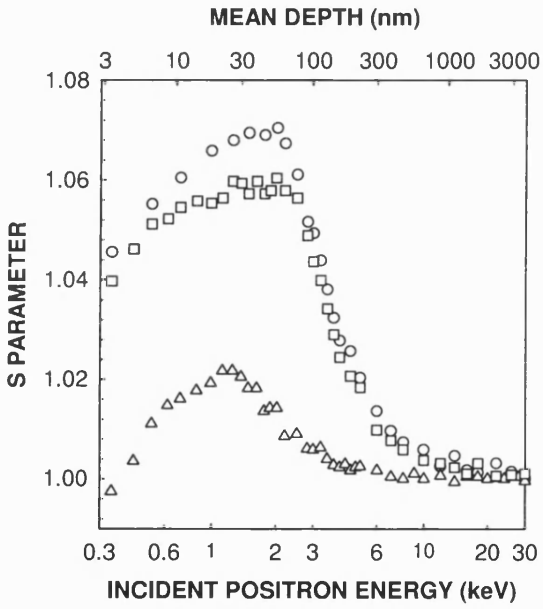

Figure 8.7: S vs incident positron energy for SiN films. Circle: 68% Si, 112nm film. Square: 52% Si, 133nm film. Up-triangle: 37% Si, 51nm film.

Figure 8.7 shows S parameter vs incident positron energy for three PECVD-deposited SiN films deposited with varying Si composition. The films were characterized using Rutherford backscattering to determine the %Si values. The PAS data were taken from 68, 52 and 37 %Si layers. The trend of decreasing S parameter with decreasing Si content is clear and can be easily calibrated. Although this data demonstrates the capability of PAS to monitor chemical composition,

in this particular case ellipsometry is more suitable. However, the use of PAS can be extended to the composition of any films (of depths of several microns) including polymer and metallic layers. Also, when used in conjunction with optical techniques such as ellipsometry, the density of thin films can be determined easily, as shown in reference [136].

8.6 Conclusion

A compact, user-friendly positron beam annihilation spectrometer has been designed and constructed in prototype form. It successfully delivers a mm-diameter positron beam to any set of chosen points on a sample wafer and reads out the results of the measurements. After initial testing the instrument is undergoing development work, principally aimed at decreasing run times. Design features, performance and first results are presented and discussed. Possible applications are described, including ion dosimetry and mapping, SIMOX process control, void monitoring and thin film interrogation.

Appendix A

Characteristic S Values for Vacancies

Using the same simulation as in Chapter 3 we have obtained characteristic S values for V_3 (Fig. A-1), V_4 (Fig. A-2) and V_5 (Fig. A-3) in silicon as a function of S values for Si bulk. Their corresponding values of figure of merit (FM) are also shown. Please note that the energy resolution of gamma photon detector is 1.44 keV.

The simulation programme is in the CD enclosed in this thesis, which is also available from Prof. P. G. Coleman, Department of Physics, University of Bath, Bath, BA2 7AY. One can easily use the value of the energy resolution of his/her gamma photon detector to get the characteristic S values for vacancies (from V to V_5) in Si.

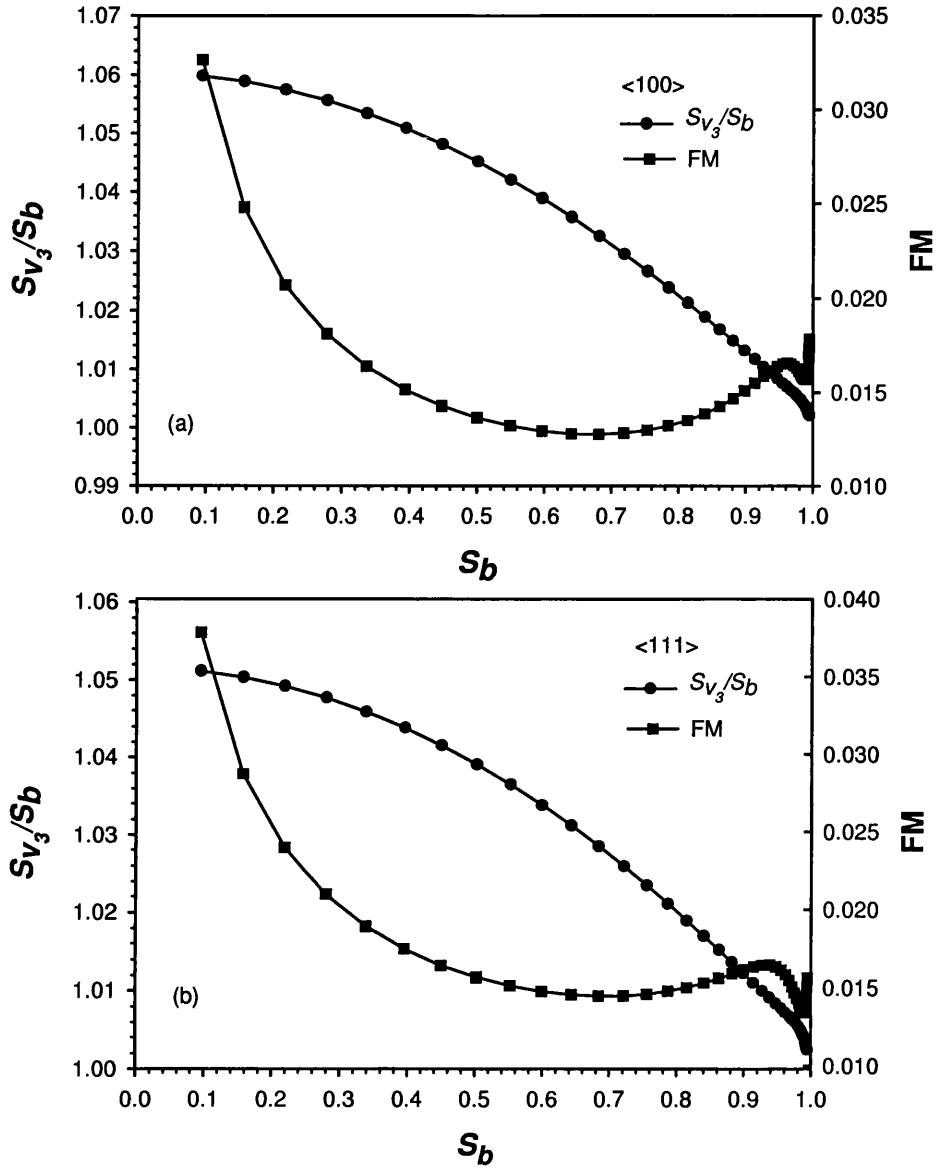

Figure A.1: Characteristic S values for V_3 in Si and their corresponding values of FM as a function of S values for the Si bulk (S_b). The crystalline orientation are (a) $\langle 100 \rangle$ and (b) $\langle 111 \rangle$. The energy resolution of gamma photon detector is 1.44 keV.

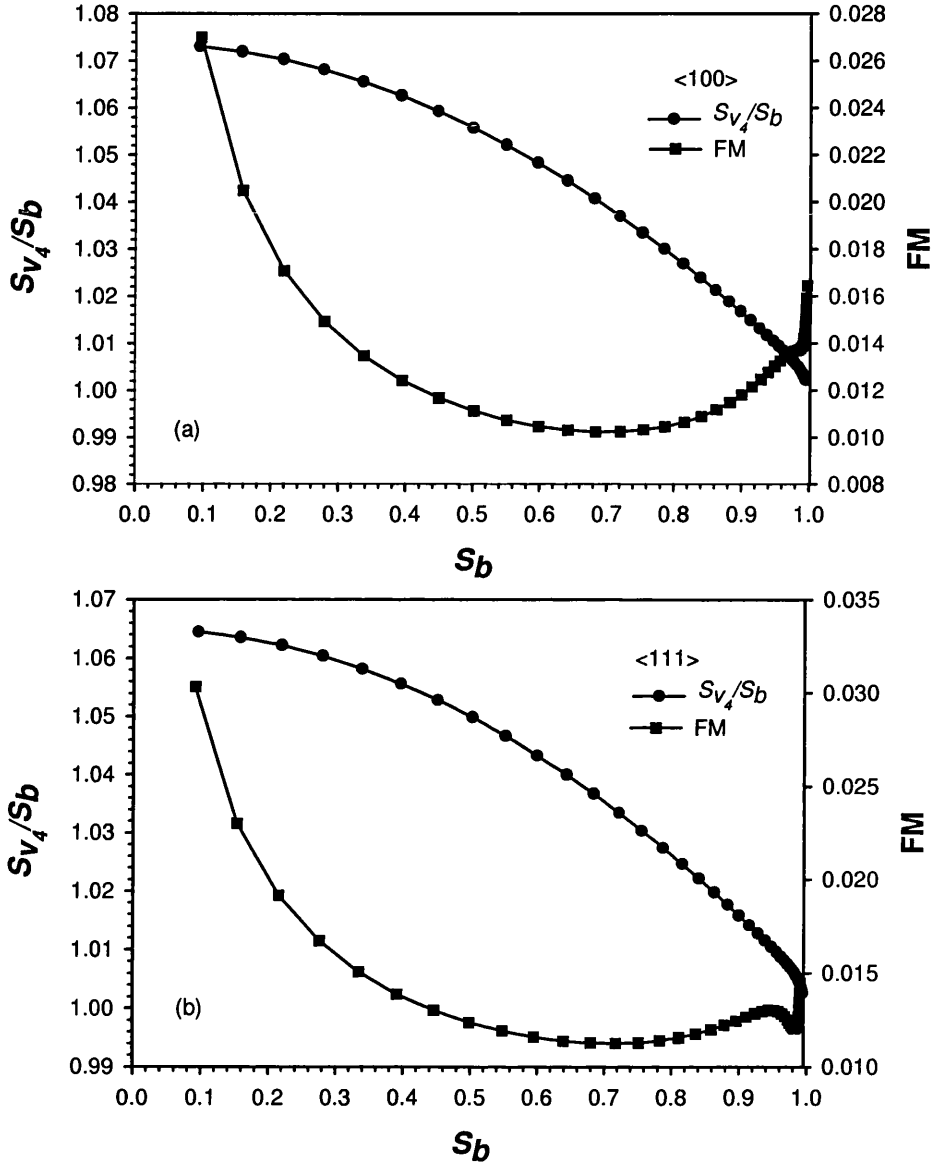

Figure A.2: Characteristic S values for V_4 in Si and their corresponding values of FM as a function of S values for the Si bulk (S_b). The crystalline orientation are (a) $\langle 100 \rangle$ and (b) $\langle 111 \rangle$. The energy resolution of gamma photon detector is 1.44 keV.

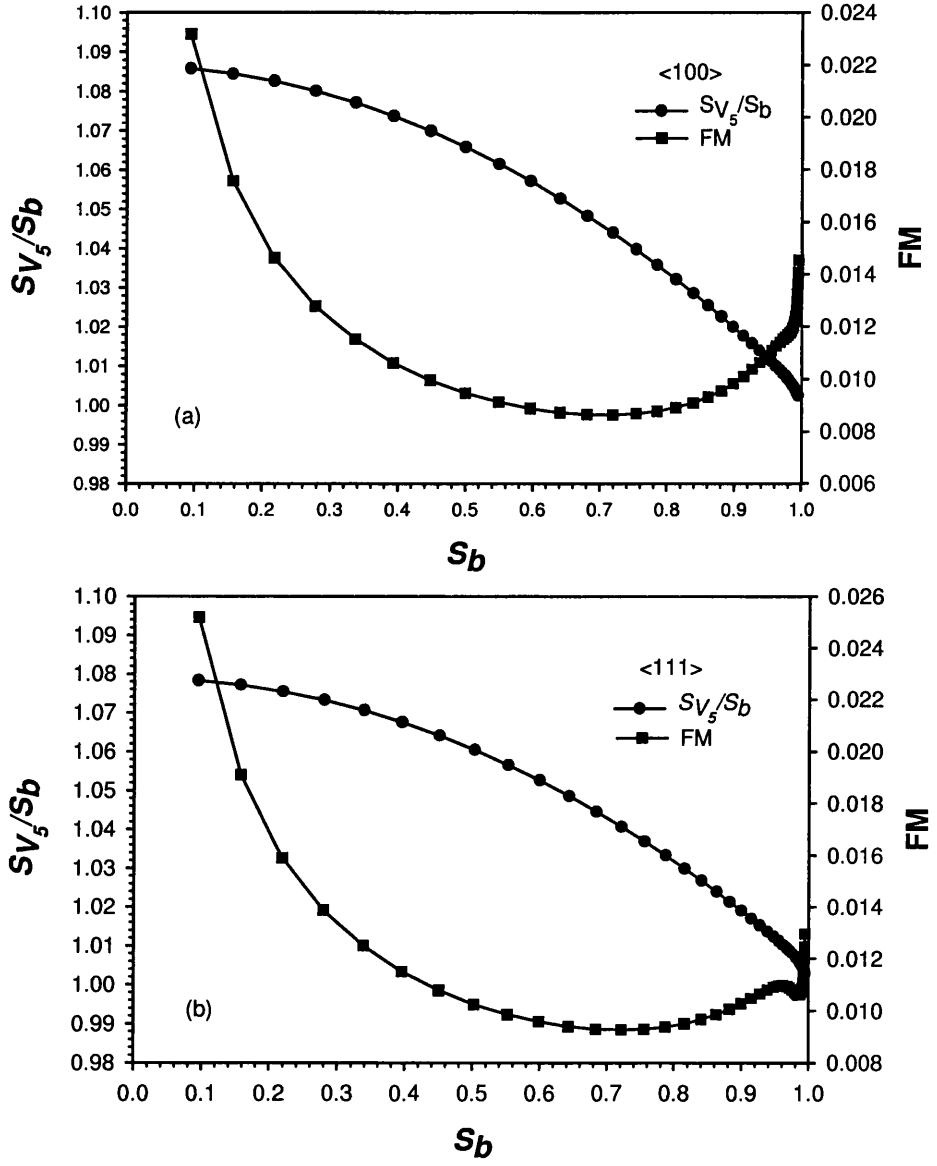

Figure A.3: Characteristic S values for V_5 in Si and their corresponding values of FM as a function of S values for the Si bulk (S_b). The crystalline orientation are (a) $\langle 100 \rangle$ and (b) $\langle 111 \rangle$. The energy resolution of gamma photon detector is 1.44 keV.

References

[1] P. J. Schultz, K. G. Lynn, Rev. Mod. Phys. 60 (1988) 701.

[2] P. G. Coleman (Ed.), Positron Beams, World Scientific, Singapore, 2000.

[3] P. Asoka-Kumar, K. G. Lynn, D. O. Welch, J. Appl. Phys. 76 (1994) 4935.

[4] R. Krause-Rehberg, H. S. Leipner, Positron Annihilation in Semiconductors: Defect Studies, Springer, Berlin, 1999.

[5] A. P. Knights, P. G. Coleman, Defect and Diffusion Forum 183-185 (2000) 41.

[6] M. J. Puska, R. M. Nieminen, Rev. Mod. Phys. 66 (1994) 841.

[7] R. M. Nieminen, J. Oliva, Phys. Rev. B 22 (1980) 2226.

[8] S. Valkealahti, R. M. Nieminen, Appl. Phys. A 35 (1984) 51.

[9] A. Vehanen, K. Saarinen, P. Hautojärvi, H. Huomo, Phys. Rev. B 35 (1987) 4606.

[10] M. Hakala, M. J. Puska, R. M. Nieminen, Phys. Rev. B 57 (1998) 7621.

[11] M. D. Giles, VLSI Technology, McGraw-Hill book company, Singapore, 1988.

[12] E. Chason, S. T. Picraux, J. M. Poate, J. O. Borland, M. I. Current, T. D. de la Rubia, D. J. Eaglesham, O. W. Holland, M. E. Law, C. W. Magee, J. W. Mayer, J. Melngailis, A. F. Tash, J. Appl. Phys. 81 (1997) 6513.

[13] The national technology roadmap for semiconductors, Tech. rep., Semiconductor Industry Association (1997).

[14] P. A. Stolk, H. J. Gossmann, D. J. Eaglesham, J. M. Poate, Nucl. Instr. Methods Phys. Res. B 96 (1995) 187.

[15] D. J. Eaglesham, T. E. Haynes, H. J. Gossmann, D. C. Jacobson, P. A. Stolk, J. M. Poate, Appl. Phys. Lett. 70 (1997) 3281.

[16] M. Griglione, T. Anderson, Y. Haddara, M. Law, K. Jones, Mater. Res. Soc. Proc. 532 (1998) 119.

[17] F. Priolo, G. Mannino, M. Micciche, V. Privitera, E. Napolitani, A. Carnera, Appl. Phys. Lett. 72 (1998) 3011.

[18] V. C. Venezia, D. C. Jacobson, T. E. Haynes, A. Agarwal, H. J. Gossamnn, F. Baumann, Appl. Phys. Lett. 73 (1998) 2980.

[19] R. Krause-Rehberg, F. Böner, F. Redmann, Appl. Phys. Lett. 77 (2000) 3932.

[20] S. O. Kucheyev, J. S. Williams, S. J. Pearton, Mater. Sci. and Engi. R 33 (2001) 51.

[21] S. M. Sze, Semiconductor Devices, Wiley, New York, 1986.

[22] J. F. Ziegler, J. P. Biersack, U. Littmark, The Stopping and Range of Ions in Solids, Pergamon, New York, 1985.

[23] S. Coffa, V. Privitera, F. Priolo, S. Libertino, G. Mannino, J. Appl. Phys. 81 (1997) 1639.

[24] P. Pellegrino, P. Leveque, J. Wong-Leung, C. Jagadish, B. G. Svensson, Appl. Phys. Lett. 78 (2001) 3442.

[25] T. D. de la Rubia, G. H. Gilmer, Phys. Rev. Lett. 74 (1995) 2507.

[26] A. L. Magna, S. Coffa, L. Colombo, Nucl. Instr. Methods Phys. Res. B 148 (1999) 262.

[27] E. C. Jones, E. Ishida, Mater. Sci. and Engi. R 24 (1998) 1.

[28] P. Mascher, S. Dannefaer, D. Kerr, Phys. Rev. B 40 (1989) 11764.

[29] G. A. Baraff, M. Schlüter, Phys. Rev. Lett. 55 (1985) 1327.

[30] M. J. Puska, J. Phys.: Condens. Matter 1 (1989) 7347.

[31] R. W. Jansen, O. F. Sankey, Phys. Rev. B 39 (1989) 3192.

[32] H. Xu, U. Lindefelt, Phys. Rev. B 41 (1990) 5979.

[33] S. B. Zhang, J. E. Northrup, Phys. Rev. Lett. 67 (1991) 2339.

[34] H. Seong, L. Lewis, Phys. Rev. B 52 (1995) 5675.

[35] D. C. Look, Z. Q. Fang, L. Polenta, MRS Internet J. Nitride Semicond. Res. 5S1 (2000) W10.5.

[36] T. Mattila, R. M. Nieminen, Phys. Rev. B 55 (1997) 9571.

[37] H. J. Stein, W. Beezhold, Appl. Phys. Lett. 17 (1970) 442.

[38] J. Keinonen, M. Hautala, E. Rauhala, V. Karttunen, A. Kuronen, J. Räisänen, J. Lahtinen, A. Vehanen, E. Punkka, P. Hautojärvi, Phys. Rev. B 37 (1988) 8269.

[39] P. Mascher, D. Kerr, S. Dannefaer, Phys. Rev. B 35 (1987) 4043.

[40] S. Szpala, P. J. Simpson, J. Appl. Phys. 89 (2001) 5991.

[41] B. Bech, H. G. Grimmeiss, Phys. Rev. B 40 (1989) 12403.

[42] M. Fujinami, R. Suzuki, T. Ohdaira, T. Mikado, Phys. Rev. B 58 (1998) 12559.

[43] A. Uedono, Y. Ujihira, L. Wei, Y. Tabuki, S. Tanigawa, J. Sugiura, M. Ogasawara, M. Tamura, Mater. Res. Soc. Symp. Proc. 262 (1992) 1061.

[44] A. Uedono, H. Itoh, T. Ohshima, R. Suzuki, T. Ohdaira, S. Tanigawa, Y. Aoki, M.Yosaikawa, I. Nashiyamai, T. Mikado, H. Okumura, S. Yoshida, Jpn. J. Appl. Phys. Pt. 1 36 (1997) 6650.

[45] L. S. Adam, M. E. Law, S. Szpala, P. J. Simpson, D. Lawther, O. Dorkumaci, S. Hegde, Appl. Phys. Lett. 79 (2001) 623.

[46] A. Polity, F. Rudolf, C. Nagel, S. Eichler, R. Krause-Rehberg, Phys. Rev. B 55 (1997) 10467.

[47] J. Gebauer, R. Krause-Rehberg, S. Eichler, M. Luysberg, H. Sohn, E. R. Weber, Appl. Phys. Lett. 71 (1997) 638.

[48] A. Uedono, L. Wei, S. Tanigawa, R. Suzuki, H. Ohgaki, T. Mikado, K. Fujino, J. Appl. Phys. 75 (1994) 216.

[49] J. S. Williams, M. J. Conway, B. C. Williams, J. Wong-Leung, Appl. Phys. Lett. 78 (2001) 2867.

[50] M. Fujinami, Phys. Rev. B 53 (1996) 13047.

[51] M. Fujinami, A. Tsuge, K. Tanaka, J. Appl. Phys. 79 (1996) 9017.

[52] S. Eichler, Ph.D. thesis, Martin-Luther-Universität Halle-Wittenberg (1997).

[53] S. Fuji, S. Shikata, L. Wei, S. Tanigawa, J. Appl. Phys. 72 (1992) 1405.

[54] J. Wong-Leung, E. Nygren, J. S. Williams, Appl. Phys. Lett. 67 (1995) 416.

[55] K. K. Larsen, V. Privitera, S. Coffa, F. Priolo, C. Spinella, M. Saggio, S. U. Campisano, Nucl. Instr. Methods Phys. Res. B 112 (1996) 139.

[56] A. van Veen, H. Schut, P. E. Mijinarends, Positron Beams and Their Applications, World Scientific, Singapore, 2000.

[57] A. van Veen, H. Schut, J. de Vries, R. A. Hakvoort, M. R. IJpma, AIP Conf. Proc. 218 (1990) 171.

[58] S. Eichler, R. Krause-Rehberg, Appl. Surf. Sci. 149 (1999) 227.

[59] L. Liszkay, K. Havancsak, Z. Kajcsos, Appl. Surf. Sci. 149 (1999) 181.

[60] S. Dannefaer, W. Puff, D. Kerr, Phys. Rev. B 55 (1997) 2182.

[61] R. S. Brusa, G. P. Karwasz, N. Tiengo, A. Zecca, F. Corni, R. Tonini, G. Ottaviani, Phys. Rev. B 61 (2000) 10154.

[62] H. J. Stein, F. L. Vook, J. A. Borders, Appl. Phys. Lett. 16 (1970) 106.

[63] J. Gebauer, S. Eichler, R. Krause-Rehberg, A. Polity, Appl. Surf. Sci. 116 (1997) 215.

[64] P. G. Coleman, A. P. Knights, R. M. Gwilliam, J. Appl. Phys. 86 (1999) 5988.

[65] C. Claeys, E. Simoen, J. Electrochem. Soc. 141 (1994) 2522.

[66] G. G. Shahidi, et al., IEEE Trans. Electron Devices 41 (1994) 2405.

[67] P. G. Coleman, N. B. Chilton, J. A. Baker, J. Phys.: Condens. Matter 2 (1990) 9355.

[68] X. D. Pi, C. P. Burrows, P. G. Coleman, Appl. Surf. Sci. 194 (2002) 255.

[69] M. Fujinami, N. B. Chilton, J. Appl. Phys. 73 (1993) 3242.

[70] A. Uedono, S. Tanigawa, J. Sugiura, M. Ogasawara, Jpn. J. Appl. Phys. 29 (1990) 1867.

[71] A. Kawasuso, M. Hasegawa, M. Suezawa, S. Yamaguchi, K. Sumino, Appl. Surf. Sci. 85 (1995) 280.

[72] R. kalyanaraman, T. E. Haynes, M. Yoon, B. C. Larson, D. C. Jacobson, H. J. Gossmann, C. S. Rafferty, Nul. Instr. and Meth. in Phys. Res. B 175-177 (2001) 182.

[73] H. Bracht, E. E. Haller, R. Clark-Phelps, Phys. Rev. Lett. 81 (1998) 393.

[74] R. C. Newman, J. Phys.: Condens. Matter. 12 (2000) R335.

[75] D. C. Gupta, R. B. Swarroap, Solid State Technol. 27 (1984) 113.

[76] U. Gösele, D. G. Ast, Energy solar technical information letter, Tech. Rep. DOE/JPL/956046-83/9 (DE40009494), U. S. Department of Energy (1983).

[77] D. F. Downey, C. M. Osburn, S. D. Marcus, Solid State Technol. 40 (1997) 71.

[78] J. D. Williams, P. Ashburn, J. Appl. Phys. 72 (1992) 3169.

[79] T. P. Ma, J. Vac. Sci. Technol. A 10 (1992) 705.

[80] M. Y. Tsai, D. S. Day, B. G. Streetman, P. Williams, J. C. A. Evans, J. Appl. Phys. 50 (1979) 188.

[81] S. P. Jeng, T. P. Ma, R. Canteri, M. Anderle, G. W. Rubloff, Appl. Phys. Lett. 61 (1992) 1310.

[82] Y. J. Park, J. J. Kim, J. Appl. Phys. 85 (1999) 803.

[83] C. Szeles, B. Nielsen, P. Asoka-Kumar, K. G. Lynn, M. Anderle, G. W. Rubloff, J. Appl. Phys. 76 (1994) 3403.

[84] B. Nielson, O. W. Holland, T. C. Leung, K. G. Lynn, J. Appl. Phys. 74 (1993) 1636.

[85] O. W. Holland, L. Xie, B. Nielson, D. S. Zhou, J. Electron. Mater. 25 (1996) 99.

[86] A. Uedono, T. Kitano, K. Hamada, T. Moriya, T. Kawano, S. Tanigawa, R. Suzuki, T. Ohdaira, T. Mikado, Jpn. J. Appl. Phys. Pt. 1 36 (1997) 2571.

[87] P. Asoka-Kumar, M. Alatalo, V. J. Ghosh, A. C. Kruseman, B. Nielsen, K. G. Lynn, Phys. Rev. Lett. 77 (1996) 2097.

[88] W. Ostwald, Z. Phys. Chem. 34 (1900) 495.

[89] P. G. Coleman, C. P. Burrows, A. P. Knights, Appl. Phys. Lett. 80 (2002) 947.

[90] A. Taguchi, Y. Hirayama, Solid State Commun. 116 (2000) 595.

[91] G. D. Watkins, J. W. Corbett, Phys. Rev. A138 (1965) A543.

[92] R. A. Stradling, P. C. Klipstein (Eds.), Growth and Characterisation of Semiconductors, Adam Hilger, Bristol, 1990.

[93] S. Coffa, S. Libertino, C. Spinella, Appl. Phys. Lett. 76 (2000) 321.

[94] T. Shimizu-Iwayama, M. Ohshima, T. Niimi, S. Nakao, K. Saitoh, T. Fujita, N. Itoh, J. phys: Condens. Matter 5 (1993) L375.

[95] L. Pavesi, L. D. Negro, C. Mazzolenl, G. Franzó, F. Priolo, Nature 408 (2000) 440.

[96] J. P. Proot, C. Delerue, G. Allan, Appl. Phys. Lett. 61 (1992) 1948.

[97] M. V. Wolkin, J. Jorne, P. M. Fauchet, G. Allan, C. Delerue, Phys. Rev. Lett. 82 (1999) 197.

[98] B. Nielsen, K. G. Lynn, Y.-C. Chen, D. O. Welch, Appl. Phys. Lett. 51 (1987) 1022.

[99] H. L. Au, P. Asoka-Kumar, B. Nielsen, K. G. Lynn, J. Appl. Phys. 73 (1993) 2972.

[100] R. Khatri, P. Asoka-Kumar, B. Nielsen, L. O. Roelling, K. G. Lynn, Appl. Phys. Lett. 65 (1994) 330.

[101] X. D. Pi, C. P. Burrows, P. G. Coleman, Phys. Rev. Lett. 90 (2003) 155901.

[102] N. B. Chilton, P. G. Coleman, Meas. Sci. Technol. 6 (1995) 53.

[103] J. C. D. Vos, Physica 20 (1954) 690.

[104] A. G. Revesz, J. Electrochem. Soc. 126 (1979) 122.

[105] G. Brauer, G. Boden, Diffusion and Defect Data 53-54 (1987) 173.

[106] M. Fujinami, N. B. Chilton, K. Ishii, Y. Ohki, J. Appl. Phys. 74 (1993) 5406.

[107] A. P. Knights, P. J. Simpson, L. B. Allard, J. L. Brebner, J. Albert, J. Appl. Phys. 79 (1996) 9022.

[108] P. J. Schultz, E. Tandberg, K. G. Lynn, B. Nielsen, T. E. Jackman, M. W. Denhoff, G. C. Aers, Phys. Rev. Lett. 61 (1988) 187.

[109] M. A. van Huis, A. van Veen, H. Schut, C. V. Falub, S. W. H. Eijt, P. E. Mijnarends, J. Kuriplach, Phys. Rev. B 65 (2002) 085416.

[110] G. Ghislotti, B. Nielsen, P. Asoka-Kumar, K. G. Lynn, L. F. D. Mauro, F. Corni, R. Tonini, Appl. Phys. Lett. 70 (1997) 496.

[111] Q. Zhang, S. C. Bayliss, D. A. Hutt, Appl. Phys. Lett. 66 (1995) 1977.

[112] G. Ledoux, O. Guillois, D. Porterat, C. Reynaud, F. Huisken, B. Kohn, V. Paillard, Phys. Rev. B 62 (2000) 15942.

[113] L. A. Nesbit, Appl. Phys. Lett. 46 (1985) 38.

[114] M. Hasegawa, M.Saneyasu, M. Tabata, Z. Tang, Y. Nagai, T. Chiba, Y. Ito, Nucl. Instr. and Meth. in Phys. Res. B 166-167 (2000) 431.

[115] D. C. Look, J. R. Sizelove, Phys. Rev. Lett. 82 (1999) 1237.

[116] S. Nakamura, M. Senoh, S. Nagahama, N. Iwasa, T. Yamada, T. Matsushita, H. Kiyoku, Y. Sugimoto, T. Kozaki, H. Umemoto, M. Sano, K. Chocho, Appl. Phys. Lett. 72 (1998) 211.

[117] J. Neugebauer, C. G. V. de Walle, Appl. Phys. Lett. 69 (1996) 504.

[118] J. Neugebauer, C. G. V. de Walle, Phys. Rev. B 50 (1994) 8067.

[119] K. Saarinen, T. Laine, S. Kuisma, J. Nissilä, P. Hautojärvi, L. Dobrzynski, J. M. Baranowski, K. Pakula, R. Stepniewski, M. Wojdak, A. Wysmolek, T. Suski, M. Leszczynski, I. Grzegory, S. Porowski, Phys. Rev. Lett. 79 (1997) 3030.

[120] K. Saarinen, P. Seppälä, J. Oila, P. Hautojärvi, C. Corbel, O. Briot, R. L. Aulombard, Appl. Phys. Lett. 73 (1998) 3253.

[121] K. Saarinen, J. Nissilä, P. Hautojärvi, J. Likonen, T. Suski, I. Grzegory, B. Lucznik, S. Porowski, Appl. Phys. Lett. 75 (1999) 2441.

[122] K. Saarinen, P. Hautojärvi, A. Vehanen, R. Kause, G. Dlubek, Phys. Rev. B 39 (1989) 5287.

[123] V. Narayanan, K. Lorenz, W. Kim, S. Mahajan, Appl. Phys. Lett. 78 (2001) 1544.

[124] X. H. Wu, P. Fini, S. Keller, E. J. Tarsa, B. Heying, U. K. Mishra, S. P. Denbaars, J. S. Speck, Japan. J. Appl. Phys. 35 (1996) L1648.

[125] P. J. Hansen, Y. E. Strausser, A. N. Erickson, E. J. Tarsa, P. Kozodoy, E. G. Brazel, J. P. Ibbetson, U. K. Mishra, V. Narayanamurti, S. P. Denbaars, J. S. Speck, Appl. Phys. Lett. 72 (1998) 2247.

[126] K. Sarrinen, P. Hautojärvi, C. Corbel, Identification of Defects in Semiconductors, Academic, New York, 1998.

[127] W. Qian, M. Skowronski, M. D. Graef, K. Doverspike, L. B. Rowland, D. K. Gaskill, Appl. Phys. Lett. 66 (1995) 1252.

[128] M. W. Cole, F. Ren, S. J. Pearton, Appl. Phys. Lett. 71 (1997) 3004.

[129] O. Ambacher, M. S. Brandt, R. Dimitrov, T. Metzger, M. Stutzmann, R. A. Fisher, A. Miehr, A. Bergmaier, G. Dollinger, J. Vac. Sci. Technol. B 14 (1996) 3532.

[130] N. Grandjean, J. Massies, F. Semond, S. Y. Karpov, R. A. Talalaev, Appl. Phys. Lett. 74 (1999) 1854.

[131] G. Popovici, W. Kim, A. Botchkarev, H. Tang, J. solomon, H. Morkoc, Appl. Phys. Lett. 71 (1997) 3385.

[132] C. Tucker, F. A. Smith, P. G. Coleman, J. Phys.: Condens. Matter 13 (2001) 1857.

[133] P. G. Coleman, et al., Ion Implantation Technology-2000, IEEE, 2000.

[134] H. Ryssel, L. Frey, J. Gyulai, H. Glawischnig (Eds.), Ion Implantation Technology-2000, IEEE, 2000.

[135] A. J. Aubertonherve, M. Bruel, B. Aspar, C. Maleville, H. Moriceau, IEICE Trans. Electronics E80C (1997) 358.

[136] R. M. Gwilliam, A. P. Knights, E. Wendler, B. J. Sealy, C. P. Burrows, P. G. Coleman, Mat. Sci. Eng. B 80 (2001) 60.